Shock Convergence and Mix Dynamics in Inertial Confinement Fusion

by

James Ryan Rygg

M.S., Electrical Engineering, Stanford University (2001)
B.S., Physics, Stanford University (2000)

Submitted to the Department of Physics
in partial fulfillment of the requirements for the degree of

Doctor of Philosophy
at the
Massachusetts Institute of Technology

July 2006

Signature of Author: .....
Department of Physics
July 14, 2006

Certified by: .....
Richard D. Petrasso
Senior Research Scientist, Plasma Science and Fusion Center
Thesis Supervisor

Certified by: .....
Miklos Porkolab
Professor of Physics
Thesis Reader

Accepted by: .....
Thomas Greytak
Professor of Physics, Associate Department Head for Education

Shock Convergence and Mix Dynamics in Inertial Confinement Fusion

by

James Ryan Rygg

Submitted to the Department of Physics
on July 14, 2006, in partial fulfillment of the requirements for the degree of
Doctor of Philosophy

Abstract

Understanding the phenomena of shock propagation and of turbulent mix induced by Rayleigh-Taylor (RT) instability growth is of critical importance for ignition and high gain in inertial confinement fusion (ICF). Capsule assembly and hot-spot formation require careful timing of multiple shocks to maximize hot-spot heating while minimizing heating of the main fuel. Unmitigated mixing of the main fuel with the hot-spot can quench hot-spot heating, resulting in reduced gain or failed ignition.

Nuclear measurements of direct-drive implosions at the OMEGA laser facility were performed to study shock convergence and mix dynamics in ICF. During these studies, an unexpected scaling of experimental nuclear yields was observed in implosions of capsules filled with different mixtures of D_2 and ^{3}He. A number of possible mechanisms to cause the scaling were considered, but no dominant mechanism has been identified.

Mix dynamics were studied using a novel capsule configuration that only emits D^{3}He protons when the fuel and shell are atomically mixed. Temporal and spectral measurements of protons emitted from such capsules were used to investigate the extent and evolution of mix, and demonstrate that the time necessary for RT instabilities to induce mix results in a delay of the peak D^{3}He reaction rate in these special capsules compared to standard capsules.

The collapse of a converging spherical shock launched by the onset of the laser pulse induces nuclear production several hundred picoseconds before deceleration and stagnation of the imploding shell. The time, duration, nuclear yields, temperature, and target compression of this shock-induced burn were measured and compared to 1-D simulations. The simulations significantly overestimate the yields, time, and compression, even though the shock collapse and resulting nuclear reaction history were experimentally demonstrated to be 1-D in nature. A 1-D model of shock convergence was constructed to gain insight into the discrepancy between experiments and simulations by extending Guderley's converging shock analysis.

It is hoped that the constraints imposed by these nuclear measurements of shock convergence and mix dynamics will enable useful tests to affirm the validity or improve the utility of the analytic and numerical tools used to understand these phenomena.

Thesis Supervisor: Richard D. Petrasso,
Senior Research Scientist,
Plasma Science and Fusion Center, MIT

Acknowledgements

The pursuit of knowledge is most enjoyable and effective as a collaborative pursuit. As such, the work reported herein was enabled and enriched by the contributions and discussions of numerous people.

I would like to express my gratitude to the members of the MIT High-Energy-Density Physics (HEDP) group, who have provided the collaborative environment in which I have thrived. The seemingly boundless enthusiasm of my research advisor, Richard Petrasso, provided continuous (and sometimes exhausting!) inspiration to see this project through, and the profusion of new ideas and insights arising from discussions with him elevated this work to a much higher level than would be possible otherwise. I would like to thank Johan Frenje for the frequent and valuable discussions, and for his patience with my plentiful questions. I benefited greatly from Chikang Li's insightful questions and thorough knowledge of the field. It would please me greatly if, through my interaction with Fredrick Séguin, this work has been imbued with at least some of his legendary diligence and rigor. In addition, I would like to thank Fredrick and Johan for their substantial efforts in the development of essential software for the analysis of data obtained by diagnostics used in this work.

The chance to run experiments on a world-class laser facility is a wonderful opportunity for a student entering the field. These experiments would not have been possible without the expertise of the OMEGA operations crew. Samuel Roberts merits particular appreciation for his instrumental role in the preparation and set-up of the diagnostics used in this work. Special mention should also be made of Jocelyn Schaeffer and Candice Culligan for their help processing the copious amount of CR-39 exposed during the experiments.

Collaboration with numerous scientists at the University of Rochester's Laboratory for Laser Energetics was instrumental for the success of this work. Riccardo Betti, Jacques Delettrez, Vladimir Glebov, Valeri Goncharov, David Meyerhofer, Craig Sangster, Sean Regan, and Christian Stoeckl provided the essential support, ideas, and discussions which have allowed the collaboration with our MIT HEDP group to prosper. Jacques Delettrez deserves special thanks for his help providing the LILAC simulations reported in this thesis.

Finally, I would like to thank the many friends and family members who read over drafts of this thesis in part or in its entirety. I would especially like to thank my parents, George and Nancy, whose unwavering love and support are blessings I too often take for granted.

Table of Contents

List of Figures

List of Tables

1 Introduction

Fusion is as old as the universe. Shortly after the Big Bang, the temperature of the universe fell below the binding energy of deuterium (2.2 MeV), which allowed nuclear fusion to proceed. Primordial nucleosynthesis then converted about 25% of the universe's baryonic mass[1] into stable helium nuclei before the universe expanded and cooled, thus quenching the fusion process. This left, in addition to hydrogen and helium, a small amount of deuterium and helium-3, as well as traces of lithium and beryllium.

An interlude without fusion lasted until the birth of the first stars, a few hundred million years after the Big Bang. Synthesis of elements heavier than beryllium takes place in the nuclear furnace of stellar cores. These heavier elements have been dispersed through the interstellar medium by the explosive deaths of massive stars, and can be observed in second and third generation stars (such as our sun) today.

Although fusion has been occurring in stellar cores for over 13 billion years, only about 1% of baryonic mass has been converted into elements heavier than helium – the composition of the universe is still dominated by the hydrogen and helium left over from the initial nucleosynthesis. In fact, the natural abundance of primordial deuterium, and its potential as an energy source, is the primary motivation driving fusion research today.

1.1 Fusion Energy

The energy released in a nuclear reaction can be evaluated using Einstein's celebrated formula, $E = mc^2$ [1]. Any difference in the masses of the reactants and products will be released (or, if the products are heavier, will need to be absorbed) as energy. The large value of the speed of light c (3×10^8 m/s) indicates that a tremendous amount of energy is available for even a small mass difference.

The number of baryons is conserved in all interactions, so it is customary to examine the mass per nucleon[2] of the elements when considering nuclear reactions. As shown in Figure 1-1, elements with high and low atomic mass numbers (*A*) have excess mass compared to the minimum mass per nucleon at ^{56}Fe. This mass excess is related to the nuclear energy available. Nuclear fission releases this energy by breaking up high *A* elements such as uranium into lower *A* elements, whereas nuclear fusion releases this energy by combining low *A* elements such as hydrogen into higher *A* elements.

[1] Baryonic matter consists of protons and neutrons, and is thought to make up 4% of the mass of the universe. Dark matter (22%) and dark energy (74%) make up the remainder. The nature of dark matter and dark energy is still poorly understood.

[2] Nucleons strictly refer to protons and neutrons, whereas baryons also include certain exotic, short-lived particles.

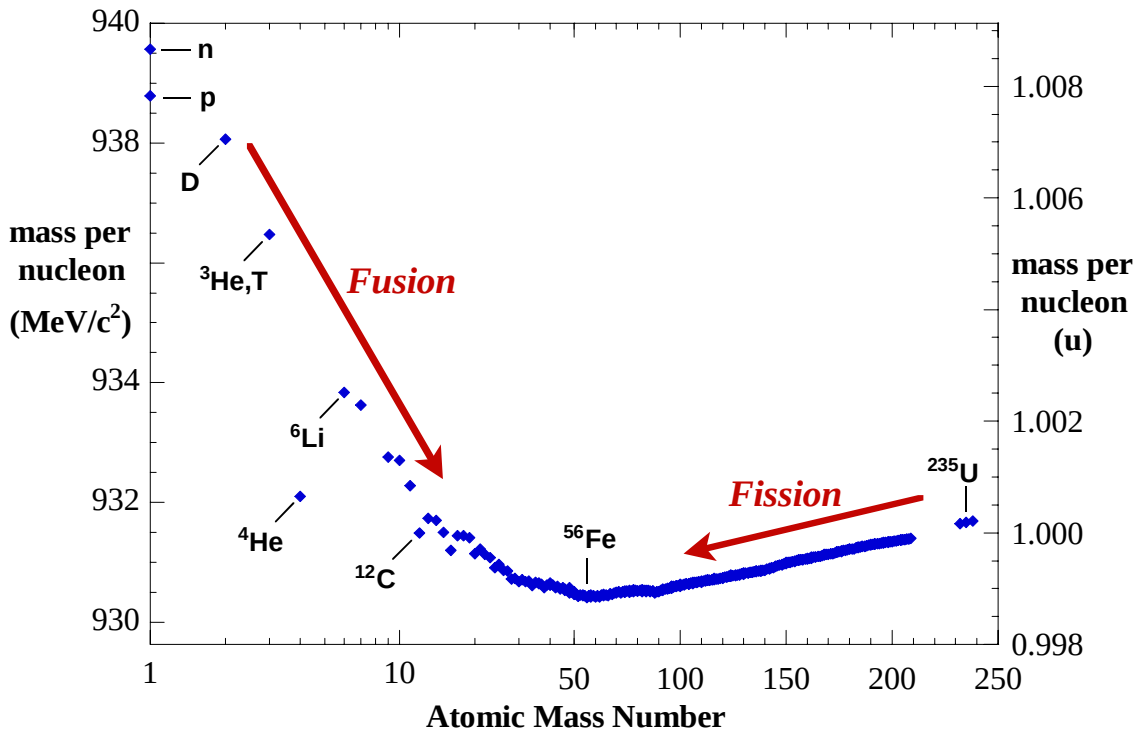

Figure 1-1: Mass per nucleon of the elements vs. atomic mass number (*A*). Note that the scale is logarithmic below *A* = 50 and linear above.

The tremendous amount of energy involved in nuclear reactions is especially remarkable when contrasted to the typical energy released in chemical reactions. For example, two deuterons (D) have 100.6% the mass of one ^{4}He. Conversion of this mass into energy would give 6 MeV per nucleon, or 6×10^8 MJ/kg. The mass difference between reactants and products in the chemical combustion of hydrogen, on the other hand, is about 2 parts in 10^{10}, yielding 3 eV per molecule of H_2, or 142 MJ/kg – more than a million times less. Table 1-1 shows the energy density of representative chemical, fission, and fusion reactions.

Table 1-1: Energy density of representative chemical and nuclear reactions.

Reaction type	Net Reaction	Energy released (eV)	Energy density (MJ/kg)
chemical combustion	$2\ H_2 + O_2 \rightarrow 2\ H_2O$	6	142
"	$CH_4 + 2\ O_2 \rightarrow CO_2 + 2\ H_2O$	9	56
nuclear fission	$^{235}U \rightarrow {}^{141}Ba + {}^{92}Kr + 2\ n$	2×10^8	7×10^7
nuclear fusion	$D + {}^6Li \rightarrow 2\ {}^4He$	2×10^7	3×10^8

The extremely high energy density of nuclear fuels and the natural abundance of deuterium (naturally occurring as 0.015% of hydrogen) combine to make fusion fuels vastly more abundant than any other energy source. Even the most optimistic estimates for fossil fuel resources fall short of available fusion fuel resources by a factor of at least 10 million. For example, using the energy density and natural abundance of deuterium, it can be shown that fusion of the deuterium in 1 gallon of ocean water releases the energy equivalent of burning about 300 gallons of gasoline.

Access to fusion energy could prove essential, as concerns over fuel resource availability, climate change, air quality, and energy security reduce the appeal of fossil fuels, which currently supply 86% of world yearly energy consumption. According to data published by the U.S. Energy Information Administration [2], we will exhaust our proven oil reserves in approximately 30 years, although as yet undiscovered resources are likely to extend this time frame. Of perhaps more concern than the finite reserves of fossil fuels, however, is the adverse effects their continued use will incur on the natural and human environment [3].

Renewables, such as wind or solar power, offer energy without many of the complications of fossil fuels, but their extremely low power density makes it hard to envision that they would contribute more than a small fraction of the total energy demand. Fission offers high power density and low climate impact, but expansion of nuclear power capacity has been inhibited by public concerns over the safety and security of the high level radioactive byproducts. Fusion offers the possibility of high power density, vast fuel resources, no high level radioactive waste, and low climate impact. It is an ideal energy source in all respects but one: the technology has not yet been developed to actually harness usable energy.

To become a viable energy source, fusion must overcome a number of considerable scientific and engineering obstacles. Unlike fission, fusion has no self-sustaining chain reaction, so fusion fuels must be burned at a high temperature[3]. However, the ignition temperature for fusion is drastically higher than for ordinary combustion – 100 million degrees rather than hundreds or thousands of degrees. Confining such an extremely hot fuel long enough for it to fuse has proven to be extremely challenging.

Fusion energy research has focused mainly on magnetic confinement fusion (MCF). At the high temperatures necessary for fusion, the fuel is ionized into the "plasma" state, and composed of electrically-charged electrons and ions. The charged particles that make up the plasma can be strongly confined by magnetic fields. MCF research has been devoted to optimizing confinement geometries and heating methods for fusion plasmas.

Inertial confinement fusion (ICF) is the other confinement method that has received significant attention. The inertia of any assembled mass will limit the speed with which it can expand and cool, and in a sense represents the lower limit of confinement. ICF techniques aim to compress the fuel to such a density that the fuel fuses before it has a chance to expand and cool.

1.2 Historical Notes

In 1920, Aston experimentally determined that the mass of the helium nucleus is less than four times the mass of a hydrogen nucleus using his recently developed mass spectrograph [4]. Shortly thereafter, Eddington used this result along with Einstein's mass-energy equation to propose the conversion of hydrogen to helium as the source of the sun's energy [5]; Eddington offered no suggestion, however, as to what allowed the hydrogen nuclei to overcome the barrier of their electrostatic repulsion in order to fuse into helium.

[3] Popular awareness of fusion research still has a strong memory of "cold fusion", first introduced to the world in a press release by Fleischmann and Pons in March of 1989, claiming the production of excess heat during the electrolysis of heavy water that could only be explained by a nuclear process. A Department of Energy meeting in May 1989 found the reports unconvincing, admitting there were unexplained phenomena, but concluding that the phenomenon would not be useful as an energy source.

The birth of quantum mechanics during the 1920s provided the explanation. Gamow and others formulated the theory of quantum tunneling, originally used to describe the radioactive decay of heavy nuclei. In 1929, Atkinson and Houtermans recognized that the Gamow tunneling mechanism opened the way for hydrogen nuclei to interact in the center of the sun [6], and in 1932, Cockroft and Walton observed the first fusion reactions in the lab [7] by using a type of linear accelerator to accelerate hydrogen atoms at a lithium target. The experimental and theoretical progress in describing fusion during the 1930s led to the publishing of a quantitative fusion theory by Bethe in 1939, which identified the dominant fusion reactions contributing to energy production in stars [8].

Wartime saw a concerted effort to develop the release of nuclear energy, as countries rushed to acquire fission weapons [9]. These efforts culminated in 1945 with the Trinity test and the subsequent bombing of the Japanese cities of Hiroshima and Nagasaki. During the war, many scientists, including Fermi, Teller, and others, speculated about using a fission bomb to ignite deuterium and create “Super” bombs. After the end of the second World War, development of a thermonuclear fusion bomb was accelerated by tensions between the United States and the Soviet Union, and the onset of the Cold War. The United States achieved the first thermonuclear detonation in 1952, followed shortly thereafter by the Soviet Union’s demonstration of a deliverable weapon in 1953.

Efforts to harness the nucleus for energy began while the fission bomb was still under development. Chicago Pile 1, the first self-sustaining nuclear chain reaction, was built in 1942 by a group of scientists led by Fermi. The first electricity from nuclear energy was produced in 1951 at the Experimental Breeder Reactor I in Idaho. Development of nuclear energy for electricity and naval propulsion continued in the 1950s in Russia, England, and the United States. In the United States, nuclear power plant construction surged in the 1960s, before declining in the 1970s, and coming to a standstill for over 25 years; no new reactors were from 1978 to 2004. The trend may be reversing, however, as two new sites were selected in 2005 for the construction of new plants. Outside the United States, there is currently much interest in nuclear energy, with several countries, such as France and Japan, generating over half their electricity through nuclear plants, and many developing countries, such as China and India, demonstrating a keen interest in rapidly expanding their nuclear generating capacity.

Nuclear fission has been accessed as a useful source of energy, but fusion energy has so far only been utilized in thermonuclear weapons. In order for fusion to become a useful energy source, the energy release has to be reduced vastly in scale and controlled. Contriving to do this introduces its own problems, as one tries to balance designs with the largest gain in the smallest system which still works. The parallel pursuit of the two main fusion confinement methods mitigates the risk of pursuing just one, in the event that one method turns out to be untenable.

Magnetic confinement fusion (MCF) research began in the late 1940s and early 1950s, and although experiments have yet to produce net power, significant progress has been made in improving heating and confinement methods over the last 50 years. Construction on the next big magnetic fusion facility, the International Thermonuclear Experimental Reactor (ITER) [10], is scheduled to begin in Cadarache, France next year, and first plasma operation is expected in 2016.

The underpinnings of inertial confinement fusion (ICF) are closely related to thermonuclear weapons development. Thermonuclear weapons are inertially confined, but in order to utilize the

energy released for purposes other than destruction, the energy yield must be scaled down by a factor of a million. It turns out that igniting milligrams of fusion fuel is much harder than the considerable challenge originally posed of igniting kilograms. The most daunting obstacle was that for such micro-explosions, fission bomb detonations can not be used to create the ignition conditions necessary for fusion. A faster and less energetic way was needed.

The discovery of the laser [11][12] was immediately recognized as a potential driver for ICF micro-explosions. At the Lawrence Livermore National Laboratory (LLNL) in 1962, a laser fusion group was formed [13], and laser fusion developed in the 1960s and 1970s along with the improvement of laser technology. Rounds of declassification in 1972 and 1992 opened the door for contributions from a wider scientific community, and numerous facilities around the world are actively investigating different aspects of the physics. Two MJ-class laser facilities are currently under construction: the National Ignition Facility (NIF) [14] in the US and the Laser MegaJoule (LMJ) in France. These facilities will not be used to produce electrical energy, but will enable studies of ignition physics.

Neither magnetic nor inertial confinement fusion has yet achieved net energy gain, but both are making notable progress and currently have major facilities under construction. Depending on the results from experiments run at these sites, a facility to further explore the conversion of fusion energy into electricity would then be built as a final step before the first commercial reactors. The time before which we can expect to produce commercial electricity is the source of much speculation, with estimates spanning the range from 30 years to never. The actual time will depend on sustained funding, improved technology, and a greater understanding of the physical phenomena which most critically affect the behavior and performance of systems confined for the release of fusion energy.

1.3 Thesis Outline

Two physical phenomena which bear critically on the performance of inertial confinement fusion (ICF) systems are the propagation of strong shocks in heated and compressed materials, and the turbulent mixing of materials induced by the saturation of Rayleigh-Taylor (RT) instability growth. This thesis presents the results of new studies of shock convergence and mix dynamics using nuclear measurements of direct-drive implosions at the OMEGA laser facility. It is hoped that the constraints imposed by these nuclear measurements will enable useful tests to affirm the validity or improve the utility of the analytic and numerical tools used to understand these phenomena.

Chapter 1 includes a discussion of fusion energy, its merits as an energy source, and a comparison with other energy sources. Brief historical notes on the discovery and development of fusion energy are also included, as is this thesis outline.

Chapter 2 contains a primer on ICF. It reviews basic fusion concepts, including fusion reactions of interest for fusion energy, the ideal ignition temperature, and different fusion confinement schemes. It also covers important ICF concepts such as confinement time, areal density, energy gain, and fuel compression. It continues with a discussion of a selection of physical phenomena and challenges encountered in ICF, including a brief explanation of the Rayleigh-Taylor instability. It concludes with a description of the OMEGA laser facility, where

all experiments reported herein were performed, and with a description of nuclear diagnostics for ICF, with particular focus on charged-particle diagnostics.

Chapter 3 discusses an unexpected scaling of experimental nuclear yields that was observed during these studies. A number of possible mechanisms to cause the scaling are considered, but no dominant mechanism has been identified.

Chapter 4 describes a novel technique to discern the presence of turbulent mixing between the fuel and shell. The first time dependent experimental measurements using this technique are used to determine the extent and timing of the turbulent mixing process in ICF implosions.

Chapter 5 presents observations of the nuclear production induced by collapse of a strong spherically convergent shock. The first measurements of the time, duration, yield, temperature, and target compression of the-shock induced burn in ICF implosions are compared to results from 1-D simulations. Significant differences between simulations and measurements are shown not to be due to multi-dimensional effects, and highlight the need for improved understanding of shock heating and propagation.

Chapter 6 compares the experimental observations and simulated results of shock induced nuclear burn with a 1-D model of shock convergence which was constructed to gain insight into the discrepancy between experiments and simulations.

Chapter 7 summarizes the results presented in this thesis.

A number of supplementary appendices are included. Appendix A contains a reference table of acronyms and abbreviations, Appendix B summarizes the manner in which means and errors were calculated, and Appendix C tabulates a selection of experimental data.

2 Inertial Confinement Fusion

This chapter contains a primer on inertial confinement fusion (ICF). Section 2.1 introduces basic fusion concepts such as thermal reactivity, ideal ignition temperature, and confinement. Section 2.2 delves deeper into topics specific to ICF, such as areal density and compression, as well as discussing different ICF configurations. An introduction to the physics of ICF implosions on OMEGA is covered in Section 2.3 – of particular importance in this section is a timeline defining key events and phases discussed in subsequent chapters. Section 2.4 examines some of the challenges which must be understood and overcome to enable ICF ignition. Section 2.5 provides details about the OMEGA laser facility, which is the premier operational facility for ICF implosion experiments. Techniques for measuring implosion conditions and a short review of essential diagnostics are contained in Section 2.6.

Interested readers are referred to several sources which cover the fundamentals of ICF more thoroughly than this chapter. A concise introduction can be found in the original paper by Nuckolls *et al* (1972) [15], and an early overview of laser-driven fusion was written by Brueckner and Jorna (1974) [16]. Lindl (1995) published a widely referenced review paper [17], as well as the associated book [18]. Finally, an excellent and much-needed book, *The Physics of Inertial Fusion*, was published in 2004 by Atzeni and Meyer-ter-Vehn [19].

In addition, many books have been published on physics topics of relevance to ICF, including *The Physics of Laser-Plasma Interactions* by W. L. Kruer (1988) [20], *Physics of Shock Waves and High-Temperature Hydrodynamic Phenomena* by Zel'dovich and Raizer (2002) [21], and *High-Energy-Density Physics* by R. P. Drake (2006) [22].

2.1 Basic Fusion Concepts

The first experimental fusion reactions were produced using a simple accelerator to direct an energetic ion beam at a solid target [7], but "beam fusion" is not a feasible method for net energy production, because the accelerated ions are much more likely to lose their energy through electromagnetic (Coulomb) scattering than they are to fuse. This loss mechanism can be overcome by heating the reactants to the temperatures needed for fusion, such that Coulomb scattering merely redistributes energy among the particles rather than acting as a loss mechanism. After a number of collisions, the particles will eventually fuse; this is known as thermonuclear fusion.

At high temperatures (above about 10^{-3} keV [4]), particle collisions are energetic enough to strip atoms of their electrons. The resulting ionized gas is considered to be in a state distinct from solids, liquids, and gases, and is known as a plasma. At the extreme temperatures necessary for fusion (at least several keV), elements with low and intermediate atomic number (Z) will become fully ionized, where all the electrons have been stripped.

Nuclear reactions of interest for fusion energy must be binary, have low Z reactants, conserve proton and neutron numbers between reactants and products, and be exothermic. Reactions must be binary since any reactions requiring more than two reactants depend on extremely unlikely 3-body interactions. Low Z reactants tunnel through the repulsive Coulomb barrier with greater

[4] Temperature in this thesis will be measured in kilo-electron-Volts (keV), where 1 keV = 11,600,000 Kelvin.

ease, and have lower X-ray losses, thereby allowing fusion at significantly lower energies than fusion between high Z reactants. Nuclear reactions that convert protons to neutrons, such as proton-proton fusion (an important process in our sun), are mediated by the Weak force[5], making the process much less likely than those mediated by the Strong force. And, of course, the nuclear reaction must be exothermic in order to extract useful energy from the reaction as it proceeds. Reactions that fit all these constraints are those that involve three specific isotopes of hydrogen and helium – deuterium (^{2}H or D), tritium (^{3}H or T), and helium-3 (^{3}He). Reactions of particular interest among these reactants are listed in Table 2-1.

The likelihood of a fusion reaction to occur is characterized by the cross section (σ), which is a strongly varying function of the relative speed of the potential reactants (v). To get the thermonuclear reaction rate in a plasma, the value of the cross section must be averaged over the relative velocities of the reactants:

$$<\sigma v> = \int_0^\infty f(v)\, \sigma(v)\, v\, dv\,, \tag{2-1}$$

where $f(v)$ is the normalized distribution of relative reactant velocities, which depends on the plasma temperature T_i. Reactants in plasmas are usually assumed to be in thermal equilibrium, and will thus have Maxwellian velocity distributions. The coefficient $<\sigma v>$ is known as the thermal reactivity, and characterizes the thermonuclear reaction rate at temperature T_i.

Thermal reactivities for reactions of interest are shown in Figure 2-1, as functions of T_i. The curves show the results of a parameterization by Bosch and Hale [23]. Mixtures of deuterium (D) and tritium (T) are considered most promising as a first fusion fuel, since the DT fusion reaction has the largest thermal reactivity at low temperatures.

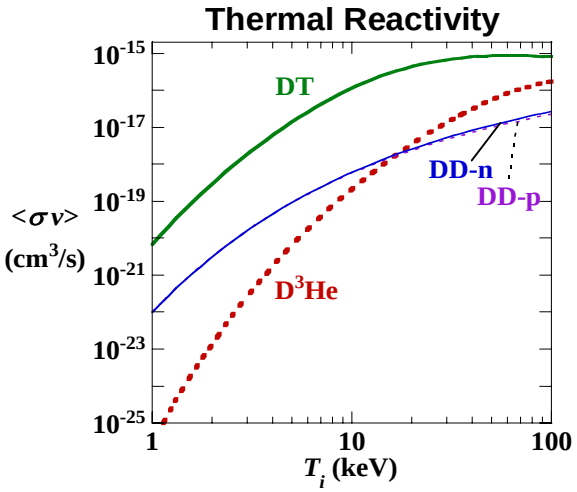

Figure 2-1 Thermal reactivity as a function of ion temperature for fusion reactions of interest.

Table 2-1: Fusion reactions of interest. Q is the energy released in the reaction.

Reaction	Label	Q (MeV)
D + T → ^{4}He + n	DT	17.6
D + ^{3}He → ^{4}He + p	D^{3}He	18.4
D + D → ^{3}He + n	DD-n	3.3
D + D → T + p	DD-p	4.0

[5] The four fundamental forces, and their coupling strength relative to the Strong force, are the Strong force (1), the electromagnetic force (1/137), the Weak force (10^{-6}), and gravity (10^{-38}).

A plasma will ignite if it gets hot enough to produce and absorb fusion energy faster than it loses energy through such processes as radiation, conduction, and diffusion. The fusion power density P_{fus} produced by an equimolar DT plasma is:

$$P_{fus} = \frac{1}{4} n^2 < \sigma v >_{DT} Q_{DT}, \tag{2-2}$$

where n is the total ion number density, and Q_{DT} is the energy released in a DT fusion reaction. The factor of 1/4 accounts for the fact that each reactant number density is half the total ion number density. Only the energy of the alpha particle (^{4}He nucleus), equal to 1/5 of Q_{DT}, is available for self heating, since the majority of uncharged neutrons escape the plasma without energy loss.

One of the cooling mechanisms is x-ray radiation, which in a fully ionized plasma is dominated by the Bremsstrahlung process. The Bremsstrahlung power density, P_{br}, emitted by a plasma with electron temperature T_e ($\approx T_i$) and atomic number Z is[6]:

$$P_{br} = C_{br} Z^3 n^2 T_e^{1/2}, \tag{2-3}$$

where the constant coefficient $C_{br} = 5.35\times10^{-31}$ W cm^3 / keV$^{1/2}$.

The "ideal" ignition temperature is the temperature at which the absorbed fusion power is equal to the radiation losses (ignoring other loss mechanisms). Above this temperature, the plasma will heat itself, since more power will be absorbed than will be lost. Figure 2-2 plots the absorbed fusion power divided by the square of the ion density as a function of plasma temperature for pure D_2 and equimolar DT fuels. The calculation for pure D_2 assumes full burnup of the primary T products, and absorption of the resulting DT-alphas. Also shown is the power lost through Bremsstrahlung radiation, and the ideal ignition temperatures at which $P_{fus} = P_{br}$ (4.3 keV for DT and 27.6 keV for D_2).

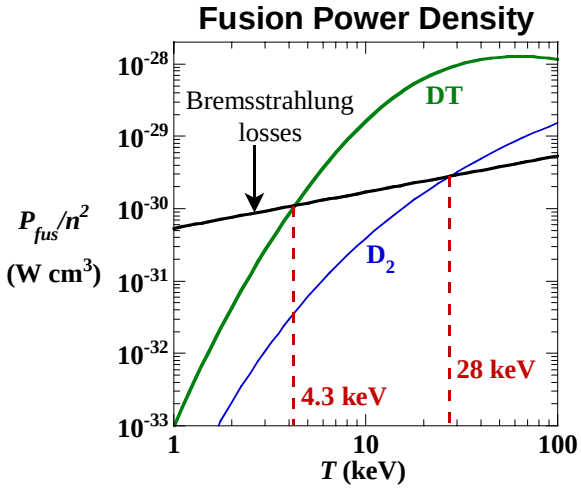

Figure 2-2: Absorbed fusion power density and x-ray Bremsstrahlung losses for DT and D_2 fuel as a function of plasma temperature. The power densities have been normalized by the square of the number density. The ideal ignition temperature (4.3 and 27.6 keV for DT and D_2 fuels) is the temperature above which the absorbed fusion power exceeds the x-ray radiation losses.

[6] For plasmas with multiple ion species, the Z^3 term should be replaced with $<Z^2><Z>$.

Not only must the temperature be high enough to ignite the fuel, but the plasma must also be confined long enough for the fuel to fuse. The characteristic time required for a particle to fuse can be simply related to the ion density and the thermal reactivity:

$$\tau_{fus} = \frac{1}{n < \sigma v >} . \tag{2-4}$$

For an equimolar DT plasma, the product of ion density and confinement time ($n\tau$) must be about 10^{15} s/cm^3 at temperatures near 30 keV in order for a significant fraction of the fuel to fuse. This value is very close to the minimum $n\tau$ necessary for ignition derived by Lawson [24], which involves a more detailed treatment of power absorption and losses. For a DT plasma at 20 keV, the "Lawson criterion" for ignition is $n\tau \geq 2\times10^{14}$ s/cm^3. This value is a bit lower because ignition of the fuel does not guarantee that most of the fuel will fuse. Better confinement is needed to take advantage of the self-heating generated through ignition to fuse a significant fraction of the fuel.

Confining a plasma at temperatures above a hundred million degrees is a challenging task – even advanced materials will melt or vaporize above just a few thousand degrees. Currently, three different methods of plasma confinement have received the most attention. The sun and other stars confine their fusing cores using gravity. Magnetic confinement uses strong magnetic fields to slow the particle and heat diffusion perpendicular to the magnetic field. Inertial confinement makes use of the fact that a heated plasma takes a finite time to disassemble under its own pressure; if compressed and heated sufficiently rapidly, a plasma can thus have time to fuse. Table 2-2 lists the plasma parameters and confinement time for the various fusion confinement methods.

Table 2-2: Plasma parameters for various fusion confinement methods.

Confinement method	Reaction	$n\tau$ (s/cm^3)	τ_{conf} (s)	n (cm^{-3})	T_i (keV)	P (atm)
gravity (sun's core)	p-p	10^{43}	10^{17}	10^{26}	1	10^{10}
magnetic fields	D-T	10^{15}	10	10^{14}	30	10
inertia	D-T	10^{15}	10^{-11}	10^{26}	30	10^{12}

2.2 ICF Concepts

The concept of inertial confinement is that expansion of any heated material under its own pressure takes a finite amount of time due to the impedance of its inertia. This is as minimal a confinement as there is, and in this section simple considerations will be used to examine what conditions are necessary for this confinement to be sufficient for fusion to occur. Further discussion of many topics in this section can be found in the tutorial paper by Rosen [25].

2.2.1 Inertial confinement

The confinement time of an assembled spherical plasma can be simply related to the ratio of the radius R to the speed of sound in the plasma c_s:

$$\tau_{conf} = \frac{R}{4c_s}, \tag{2-5}$$

where the factor of 1/4 reflects the mass-average of the distance of the plasma from its surface. The speed of sound is related to the plasma temperature T, the average ion mass m, and the adiabatic index γ by $c_s^2 = (\gamma+1)T/m$. For inertial confinement, the confinement parameter $n\tau$, described in Section 2.1, is customarily expressed in terms of the areal density ρR of the assembled plasma:

$$n\tau = \frac{\rho}{m}\frac{R}{4c_s} = \frac{1}{4mc_s}\rho R. \tag{2-6}$$

For a spherical DT plasma at 30 keV, the confinement criterion $n\tau \geq 10^{15}$ s/cm^3 becomes $\rho R \geq 2.5$ g/cm^2.

The advantage of expressing the confinement condition in terms of the areal density is that areal density has another important physical interpretation, in which ρR is also used as a shorthand notation for the radial integral of the density:

$$\rho R = \int_0^R \rho(r)dr. \tag{2-7}$$

This expression for ρR is a generalization that holds also for non-uniform densities (as we shall see in the next subsection, uniform density is not necessarily the ideal configuration).

The areal density also has the interpretation of being the amount of material that an energetic particle needs to pass through in order to escape the plasma sphere. This makes the measurement of energetic particles a useful diagnostic probe for this important ICF parameter (see Section 2.6).

2.2.2 Energy yield and gain

To evaluate the energy produced by an inertial plasma assembled to meet the confinement criterion, we first express the fusion energy yield per unit fuel mass released by a fusing equimolar DT plasma:

$$E_{fus} = \frac{Q_{DT}}{2m} f_B, \tag{2-8}$$

where Q_{DT} is the energy released per DT fusion reaction, and f_B is the fraction of the fuel that fuses. To release maximal fusion energy from a given fuel mass, a large fraction of the fuel must fuse, and so fuel depletion cannot be neglected as fusion proceeds. The number density of the reactants in an equimolar DT mixture decreases with time as the fuel fuses according to:

$$\frac{dn}{dt} = -\frac{n^2}{2} < \sigma v >_{DT}, \tag{2-9}$$

where n is the total reactant number density. Assuming the thermal reactivity stays constant, integration of this reaction rate equation will give the remaining density n as a function of the

burn time τ and the initial density n_0. Expressing the fractional burn as $f_B = 1\text{-}n/n_0$, the integration of Equation (2-9) gives:

$$\begin{aligned} f_B &= \frac{n_0 \tau}{n_0 \tau + 2/<\sigma v>_{DT}}, \\ &= \frac{\rho R}{\rho R + 8m c_s /<\sigma v>_{DT}}. \end{aligned} \tag{2-10}$$

For DT plasmas at temperatures near 30 keV, $c_s/<\sigma v>_{DT}$ has a very weak temperature dependence, which leads to a common approximation to Equation (2-10):

$$f_B = \frac{\rho R}{\rho R + 6\, g/cm^2}. \tag{2-11}$$

For ρR = 2.5 g/cm^2, the fractional burn is 30% and the fusion energy yield is $E_{fus} = 10^8$ MJ/kg.

The fusion energy released by an inertial plasma is usually evaluated in terms of the gain G, which compares the fusion energy produced to the energy needed by a "driver" to assemble and heat the plasma to the conditions necessary for fusion. G is defined as:

$$G = \frac{E_{fus}}{E_{dr}}, \tag{2-12}$$

which is the ratio of E_{fus} to the energy delivered by the driver per unit fuel mass, E_{dr}.

Several inefficiencies exist in converting the energy of the assembling driver into the final internal energy of the plasma ball, E_{plas}, just before ignition. The conversion efficiency of energy into the plasma η is defined by: $\eta = E_{plas}/E_{dr}$. The value of η depends on the details of the assembly scheme, and is described elsewhere (for example, Reference [19]); here, 10% will be chosen as a representative value for η.

The simplest configuration in which to evaluate E_{plas} is to assume that the entire fuel is heated to temperature T. This ICF configuration is often referred to as "volume ignition", and is characterized by an isothermal fuel. The internal energy of the plasma can then be simply calculated as its total thermal energy:

$$E_{th} = 3\frac{T}{m}. \tag{2-13}$$

Although the fuel will burn at temperatures of 30 keV and higher, it is only necessary to heat the fuel to some small multiple of the ideal ignition temperature, at which point the plasma will ignite, and self-heating will propel the plasma to higher temperatures. For a DT plasma at 8.6 keV, which is twice the ideal ignition temperature, $E_{th} = 10^6$ MJ/kg.

The gain of an isothermal DT plasma can thus be reduced to:

$$G_{isothermal} = \frac{1}{6}\frac{Q_{DT}}{T}\eta\, f_B\,. \tag{2-14}$$

For an 8.6 keV plasma with $\rho R = 2.5$ g/cm^2, $G_{isothermal} = 10$. This gain is not sufficient to overcome low conversion efficiencies external to the fuel such as the efficiency of converting electrical energy into the energy used by the driver (~10%) and the efficiency of converting the fusion energy yield into electrical energy (~33%). To overcome these low conversion efficiencies, gains of 100 or greater are necessary.

Fortunately, the gain can be greatly enhanced using a fuel configuration which makes further use of the fusion energy produced within the fuel assembly. The key is to heat only a small fraction of the fuel (~1%) to the ignition temperature, and to arrange the rest of the fuel such that the energy released in this "hot-spot" heats the nearby, cold fuel to the ignition temperature. This nearby region fuses and releases more energy, which heats the next region, and thus a fusion burn wave forms which propagates through and fuses the remainder of the cold fuel.

The "conventional" approach to ICF, also sometimes referred to as "hot-spot" ignition, assembles the fuel at nearly uniform pressure. This isobaric fuel has a low-density hot-spot at the center of a cold, dense fuel. All work described in this thesis was performed using this conventional ICF configuration.

A second approach, described by Tabak *et al* [26], sometimes known as "fast ignition", first assembles the fuel at nearly uniform density. A small region of this isochoric fuel is then rapidly heated by a second driver to produce a high-density hot-spot. Fast ignition offers the potential for about twice the gain compared to conventional ICF at a given driver energy, and with reduced symmetry requirements. However, significant additional physics and engineering challenges must be understood and overcome for that potential to be realized.

A sketch of the density and temperature profiles for the ICF configurations described is shown in Figure 2-3.

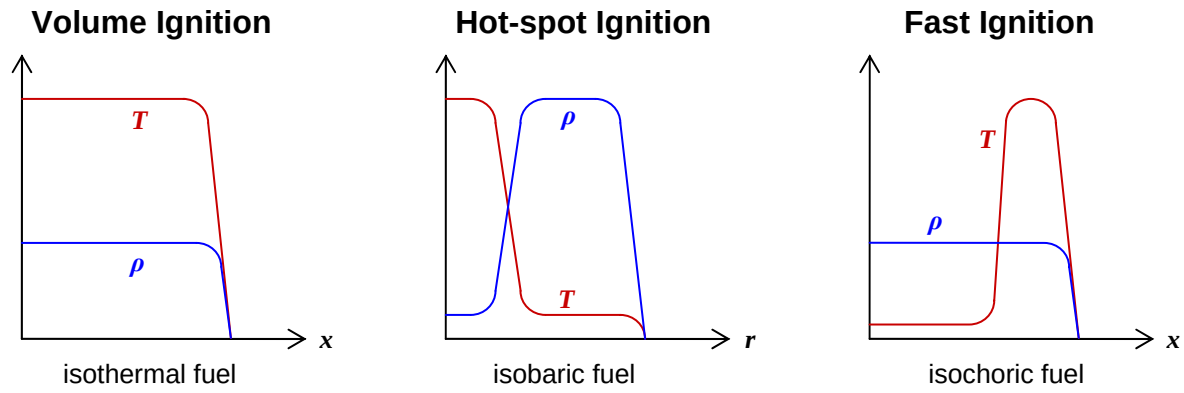

Figure 2-3: Density and temperature configurations for ignition in ICF. The conventional ICF, or "hot-spot ignition" configuration is spherical; the other two do not necessarily need to be spherical. The conventional ICF and fast ignition configurations require substantially less energy to assemble than the volume ignition configuration. The work reported in this thesis was performed using the conventional ICF configuration.

2.2.3 Compression

In order to calculate the actual fusion energy released, we must still determine the mass of the fuel. So far, the only confinement criterion that has been identified is a lower limit on the areal density, which can be related to the total fuel mass M as:

$$M = \frac{4\pi}{3}\frac{(\rho R)^3}{\rho^2}. \tag{2-15}$$

If we use the uncompressed solid DT density, $\rho = 0.21$ g/cm^3, then a mass of 1.5 kg would be required to attain a ρR of 2.5 g/cm^2. The radius of such a DT fuel would be 12 cm, and the fusion yield with $f_B = 30\%$ would be 1.5×10^8 MJ, more than twice the energy released by the Hiroshima bomb!

Furthermore, if the gain on the driver energy takes the isothermal value of 10, then 1.5×10^7 MJ would be needed to drive the implosion. The driver energy requirement would be prohibitive even using the higher gains achievable using the hot-spot or fast ignition configurations.

Clearly, a smaller fuel mass must be used, so that both the energy yield is not catastrophic, and the energy required to quickly assemble the fuel and heat it to temperatures necessary for fusion can be accomplished by using methods other than an atomic blast[7]. Because the fuel mass depends on the inverse square of the density, compression of the fuel to ~1000 times solid density is needed to produce manageable energy yields (below 1000 MJ).

The energy requirement for compression of a material is most efficiently accomplished at low temperatures and pressures, since this will reduce the necessary amount of PdV work. At low temperatures and high densities, the pressure is dominated by the quantum electron degeneracy pressure. The Fermi-Dirac electron degeneracy pressure is used to derive the internal energy per unit mass:

$$E_{FD} = C_{FD}\frac{Z^{2/3}}{A^{5/3}}\left(\frac{\rho}{1\,g/cm^3}\right)^{2/3}, \tag{2-16}$$

where the constant coefficient $C_{FD} = 327$ MJ/kg. Compression of a DT plasma to 300 g/cm^3 requires $E_{FD} = 1.5\times10^4$ MJ/kg. This energy requirement is nearly a factor of 100 less than the energy required to heat the fuel to ignition temperatures.

In practice, the internal energy of a compressed fuel will be higher than the ideal, zero-temperature compression energy. The internal energy of the compressed fuel E_{cf} will be some multiple of the Fermi-Dirac internal energy:

$$E_{cf} = \alpha_{cf}\, E_{FD}, \tag{2-17}$$

where the adiabat $\alpha_{cf} \geq 1$. A representative value $\alpha_{cf} = 2$ will be assumed.

[7] The fusion fuel in a hydrogen bomb is inertially confined, has a mass of several kilograms, and is ignited using the energy released by a conventional atomic bomb.

Let us examine the fuel assembly and driver energy requirements necessary to achieve a fusion energy yield of 300 MJ. With a total ρR of 2.5 g/cm^2, the fuel mass needed will be about 3 mg. The energy required to compress this mass to a density of 300 g/cm^3 with $\alpha_{cf} = 2$ is about 0.09 MJ. If we reserve 1% of the fuel mass for the hot-spot, the energy required to heat the hot-spot to 8.6 keV is about 0.01 MJ. The driver energy required to assemble this plasma, with $\eta = 10\%$, is 1 MJ, resulting in $G = 300$.

Although 300 is a promising gain on our invested driver energy, the gain that is actually realized will be lower due to an array of instabilities and challenges, described in Section 2.4. For maximal gain, constraining the adiabat to close to one is desirable, as any excess energy that goes into the cold compressed fuel will substantially reduce the achievable gain.

2.2.4 ICF drivers and capsule assembly

It has been shown that significant gain can be achieved, resulting in manageable yields using only milligrams of DT fuel, assuming a clever arrangement of the fuel into compressed and heated regions. Although the driver energy requirement may be reasonable, how exactly is the plasma assembled? The bulk of the plasma must be compressed to over 1000 times solid density, and a small region at the core must be heated to several keV without excessive heating of the surrounding cold fuel. This entire assembly process must occur very rapidly, as the plasma is confined for a very brief time by only its own inertia.

Compression of matter to such extreme densities is accomplished by implosion of a spherical shell (see Figure 2-4). Rapid deposition of the driver energy in the form of lasers or x-rays on the surface of a spherical target heats the outer layer and causes it to expand, which dramatically increases the pressure at the surface. The very high pressure on the outer surface relative to the initial pressure still present in the core of the capsule compels the material to accelerate inwards. As the driver continues to deposit energy, material from the heated surface ablates outwards, and drives the inner material inwards.[8]

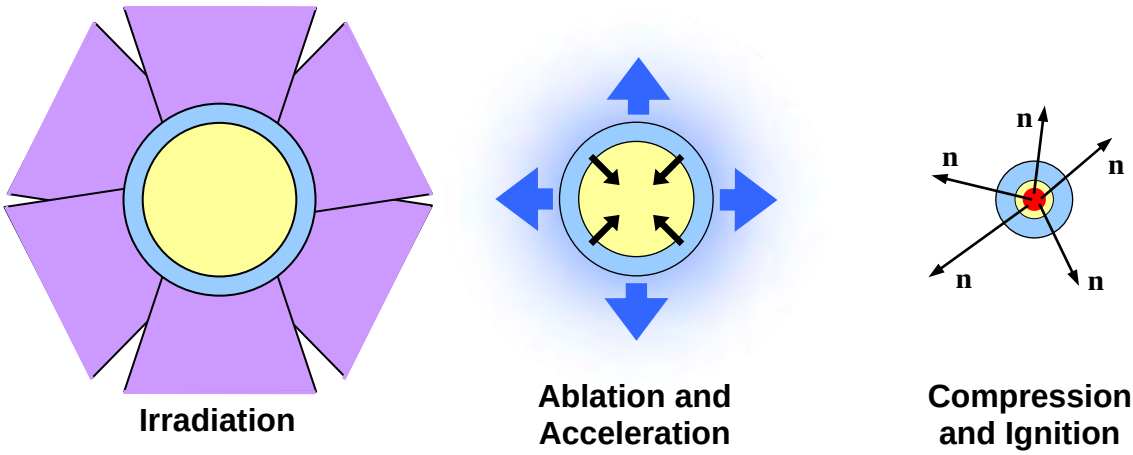

Figure 2-4: Timeline schematic of an ICF implosion. A spherical shell is irradiated by lasers or x-rays, which ablates the surface material and accelerates the capsule inwards. The fuel is compressed by the imploding shell, thereby igniting the target and initiating a fusion burn wave through the fusion fuel.

[8] This ablation driven implosion can be viewed as a spherical rocket, with the ablative "exhaust" pushing the inner "payload" inwards.

The driver energy is thus converted to the kinetic energy of the imploding shell. The shell material compresses as it converges, converting kinetic energy into the internal compression energy of the fuel. The density compression factor is greatly enhanced in spherical geometry for a given linear compression factor C_r, where the density scales as $\sim C_r^3$ (as compared to $\sim C_r^2$ in cylindrical and $\sim C_r$ in planar geometry).

In the "hot-spot" ignition scheme, the target shell has a gaseous DT fill, which is compressed by the imploding shell and heated by shocks launched by the ablation drive to form the hot-spot. Strong shocks are needed to heat the hot-spot to ignition temperatures, but since the shocks must propagate through the main fuel in the shell on their way to the hot-spot, they heat the main fuel, raising its adiabat α_{cf}. To maximize gain, then, an optimal balance must be found between compressing the main fuel with minimal heating and heating the hot-spot as efficiently as possible.

Several means of delivering the driver energy have been considered, including intense heavy-ion and light-ion beams, as well as lasers of various wavelengths. Ion beams offer the potential of delivering the energy with a higher driver or "wall-plug" efficiency, but ion beams of sufficient intensity to drive ICF implosions have not yet been produced. Energetic lasers which can easily manage the needed intensities (10^{15} W/cm^2) have rather poor driver efficiencies. Dramatic improvement in the efficiency of high-energy lasers will be necessary for inertial fusion energy to be viable.

Two driver configurations have been studied for conventional ICF (see Figure 2-5): direct-drive [27] and indirect-drive [17]. For direct-drive implosions, the laser is directly incident on the surface of the spherical target capsule. For indirect-drive implosions, the laser is absorbed on the inner surface of a cylindrical "hohlraum" and converted to x-rays, which then drive the target capsule. Indirect drive offers improved illumination symmetry and reduced sensitivity to hydrodynamic instabilities (see Section 2.4), at the expense of reduced coupling efficiency η.

All experiments in this thesis were performed using laser drivers in the direct-drive configuration.

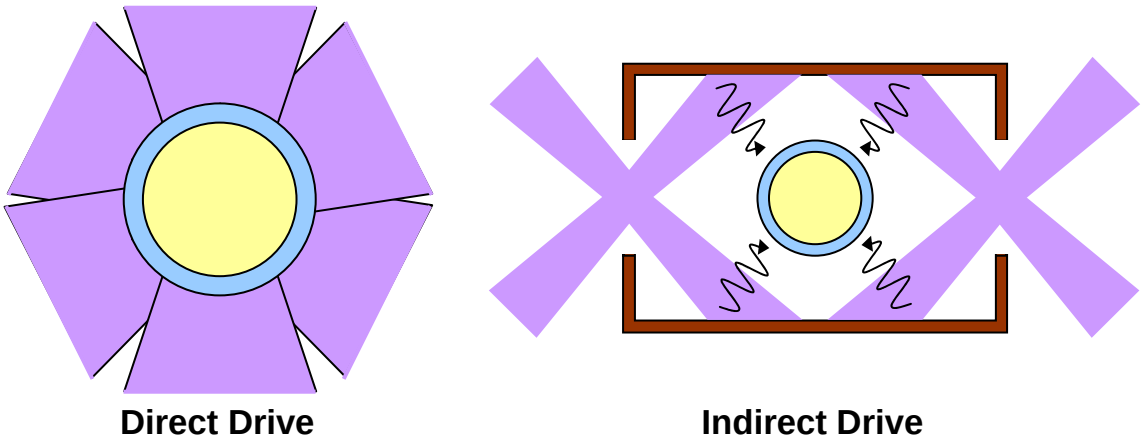

Figure 2-5: Direct drive and indirect drive configurations. For direct-drive implosions, the laser is directly incident on the surface of the spherical target capsule. For indirect-drive implosions, the laser is absorbed on the inner surface of a cylindrical "hohlraum" and converted to x-rays, which then drive the spherical target capsule.

2.3 Implosion physics

2.3.1 ICF targets and simulations

Direct-drive ignition designs for the National Ignition Facility (NIF) [14], under construction in Livermore, California, use the 192 laser beams to deliver up to 1.8 MJ of laser energy to a spherical target. The baseline capsules are 3.4 mm in diameter and consist of a 340 μm layer of DT ice enclosed by a 3 μm thick polystyrene (CH) shell (Figure 2-6). A specially shaped laser pulse with a 10 TW "foot", and a 450 TW main drive is designed to put the main fuel on an adiabat $\alpha_{cf} = 3$, and is predicted by 1-D simulations to produce a gain of 45 [28].

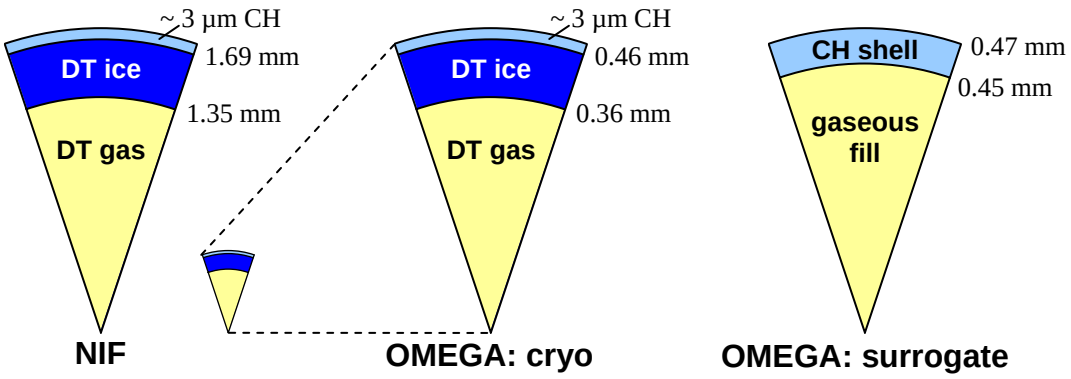

Figure 2-6: NIF direct-drive ignition targets, OMEGA cryogenic targets, and OMEGA surrogate targets. OMEGA cryogenic targets are energy-scaled from NIF ignition designs, with the laser energy scaling as the cube of the radius, and using $E_{NIF} = 1.5$ MJ, $E_{OMEGA} = 30$ kJ. The small capsule image to the right of the NIF capsule diagram is an OMEGA target drawn to the same scale as the NIF target. OMEGA surrogate targets have a thick CH shell that is the mass-equivalent of the ice-layer in OMEGA cryogenic targets.

ICF cryogenic target designs for the currently operating 30 kJ OMEGA laser facility [29][30] (see Section 2.5) are energy-scaled from ignition designs on the NIF [28]. Although implosions of cryogenic targets on OMEGA do not produce fusion energy gain, they provide an important test-bed for studying capsule assembly and testing predictive computer models. Cryo-surrogate "warm" targets have mass-equivalent shells made of CH, and can be used to test many aspects of capsule assembly. They are often used in place of cryogenic targets because they are much easier to manufacture.

A diverse set of physical phenomena describe the driving, compression, and nuclear burn in an ICF implosion, and analytical tools can only model limited aspects of these processes. Numerical calculations are therefore used to predict the performance of ICF targets in experiments. A wide array of different computer codes, many with hundreds of man-years of development time, have been produced to simulate the behavior of ICF implosions, as well as to simulate in detail different physical phenomena of relevance to ICF. The utility of these codes relies on proper understanding and implementation of relevant physical processes. Tradeoffs are always made between the accuracy and complexity of the model versus the ability to run the simulation in a reasonable time.

Experimental benchmarking is also of essential importance to the utility of the predictive codes. A constant interplay between code development and experimental verification or refutation must take place to refine the codes and improve confidence in their results.

The radiation-hydrodynamic code LILAC [31] was used for most numerical simulations shown in this thesis. LILAC is a one-dimensional (1-D) Lagrangian hydrodynamic code which includes laser beam ray-tracing, a Thomas-Fermi equation of state, and multi-group diffusion radiation transport. The electron thermal energy is transported using a flux-limited diffusion model in which the effective energy flux is defined as the minimum of the diffusion flux and a fraction f of the free-streaming flux, where the flux limiter $f = 0.06$, unless otherwise specified.

Two "input decks" were used to set parameters for the LILAC simulations. Unless otherwise specified, results shown are from simulations using the "old" input deck. A "new" input deck which has modified fluid element zoning, early pulse laser absorption, and equation of state parameters was first used in 2005. The use of this new input deck was partly motivated by experimental results attained for and reported in this thesis (see Chapter 5), and had significant effects on the simulated shock yield and timing.

In addition, a simple numerical code, based on a self-similar fluid model, was developed and used to model aspects of nuclear production after the shock collapse. A description of and representative from this code results are shown in Chapter 6.

2.3.2 Simulation of an OMEGA implosion

Important features and events common to ICF implosions will be discussed in this subsection using a specific shot (shot 38525) as an example. Although the timing and specific values of physical events and parameters are specific to warm-target surrogate OMEGA implosions, most essential features are qualitatively shared by simulations of ignition design implosions.

OMEGA shot 38525 had a spherical target capsule with a 24 μm thick plastic (CH) shell, a 428 μm outer radius, a gaseous fill of 6 atm D_2 and 12 atm ^3He, and an outer aluminum flash coating of about 0.1 μm. The gases were filled at a temperature of 293 K, resulting in a fill density of 0.0025 g/cm^3. The target was shot with a typical 1-ns square laser pulse, which delivered 22.1 kJ of 0.351 μm UV light, with a peak power of 22 TW and a peak intensity of 9.6×10^{14} W/cm^2. The beam-to-beam energy imbalance among the 60 beams on this shot was 2.5% rms, which resulted in an on-target root-mean-square (rms) illumination non-uniformity of about 1.4%.

Figure 2-7 shows results from a LILAC simulation of OMEGA shot 38525 using the new input deck. Subfigure (a) shows the laser pulse and the D^3He proton production history, and subfigure (b) shows the space-time trajectories of shocks, fluid elements, and the interface between the fuel and the shell. Important events are highlighted in both subfigures, and are also summarized in Table 2-3. A summary of different time phases during the implosion is provided Table 2-4.

Table 2-3: Timeline of important events in a typical OMEGA implosion driven with a 1 ns square pulse.

item	Event	time	Description
1	Laser on	0.0 ns	Laser intensity reaches 3% of maximum
2	Shock breakout	0.5 ns	Shock breaks out from inner shell surface
3	Laser off	1.25 ns	Laser intensity falls below 3% of maximum
4	Shock coalescence	1.3 ns	1st and 2nd shocks coalesce in the gas
5	Shock collapse	1.7 ns	Converging shock collapses and reflects at center of capsule
6	Shock-bang time	1.75 ns	Maximum D^3He-p production rate in shock peak
7	Deceleration phase onset	1.8 ns	Reflected, outgoing shock encounters imploding shell
8	Bang time	2.1 ns	Maximum nuclear production rate
9	Stagnation	2.2 ns	Time of maximal convergence and highest central pressure

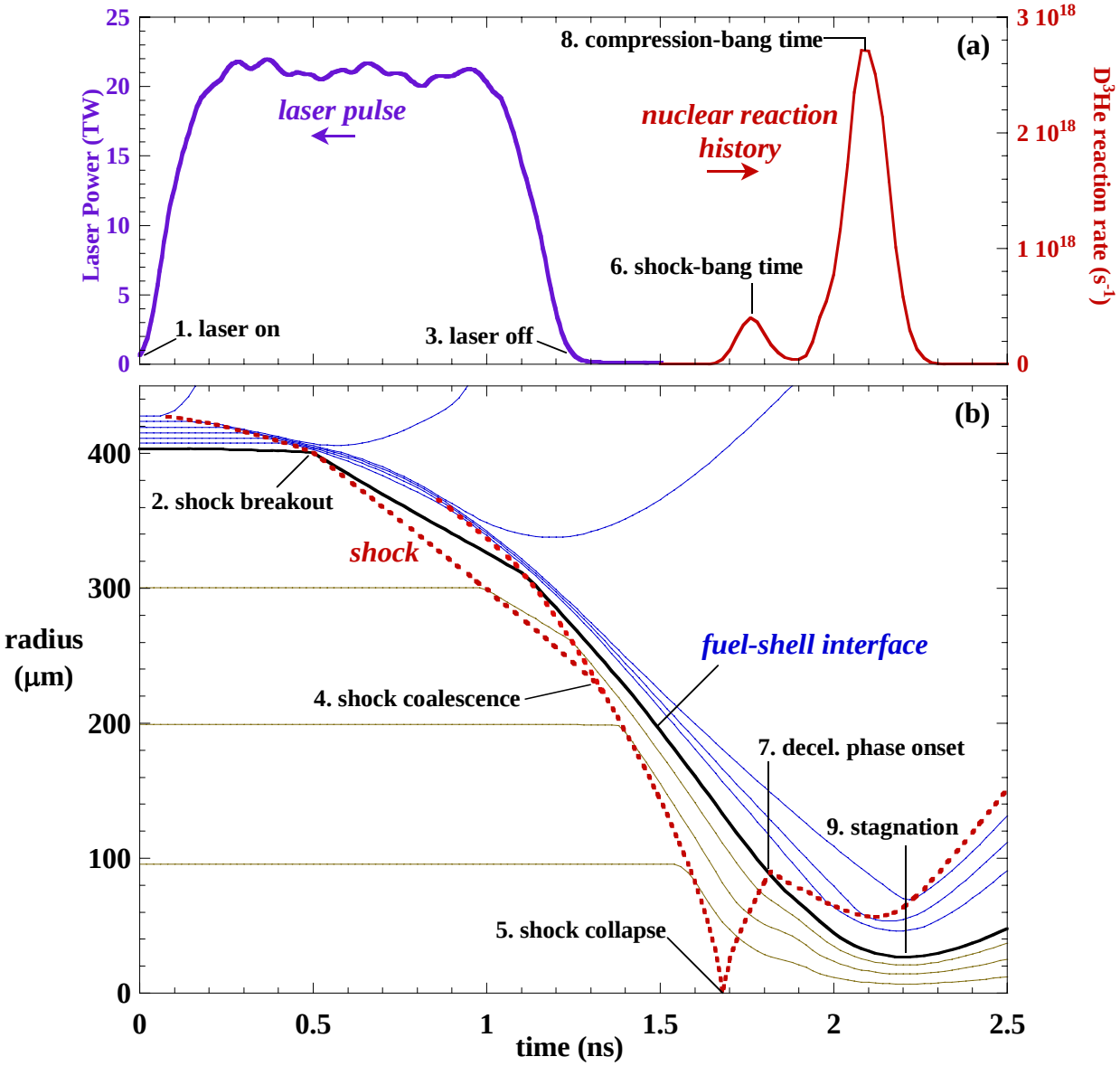

Figure 2-7: LILAC simulation of OMEGA shot 38525. This was a 24 μm, 18 atm D^3He target shot with 23 kJ. Events of interest from Table 2-3 are labeled. (a) The 1 ns square driving pulse (the experimental measurement is used for the post-shot simulation) and the D^3He nuclear reaction history. (b) Fluid element trajectories and shock path. The simulation does not track the shock path near the moment of collapse, so instead a best fit Guderley trajectory was used.

The incidence of the laser pulse (1) on the target begins the clock, as the reference time t=0 is defined by the time the target illumination intensity reaches 3% of its peak value. Although the plastic is transparent at lower intensities, such a high intensity quickly ionizes the surface of the capsule. A low density plasma corona is formed, where the laser is absorbed near the critical surface[9], and the heat is transported inwards by electron thermal conduction. The surface of the remaining high density shell absorbs this incoming energy and ablates. Mass flow off the ablation front increases the pressure to about 50 Mbar[10], which forms an ingoing shock front. This early phase of the implosion is sometimes known as "shock transit" (I).

The ingoing shock eventually breaks out from the inner surface of the shell (2), which is transmitted into the fuel, and an outgoing rarefaction (release wave) is sent back through the shell. The return of the rarefaction to the ablation front initiates the "acceleration phase" (II), and launches a second ingoing shock. The shell is sharply accelerated during the acceleration phase, from about 50 km/s (50 km/s = 50 μm/ns) at shock breakout to nearly 300 km/s by the end of the laser pulse (3), an average acceleration of 3×10^{14} m/s^2 (= 3×10^{13} g).

Table 2-4: Phases of an OMEGA implosion driven with a 1ns square pulse.

Phase	Phase name	start and finish events	Description
I	Shock transit	event 1-2	Initial shock transits through the shell
II	Acceleration Phase	event 2-3	Shell is accelerated by ablation of outer material
III	Coasting Phase	event 3-7	Shell coasts inwards at constant speed
IV	Deceleration Phase	event 7-9	Increasing pressure in the core decelerates imploding shell
V	Reexpansion	event 9-	Highly compressed material re-expands

During the "coasting phase" (III), the shell ballistically moves inward at a constant speed of about 300 km/s. The second shock, meanwhile, has been traveling faster than the first shock, since it is moving through a medium that is moving inwards. Eventually, the second shock overtakes the first shock, coalescing with it to create a stronger shock (4)[11]. This strong coalesced shock continues to rapidly converge, and soon collapses at the center (5). The shock collapse launches a new, reflected, outgoing shock, which heats the inflowing fuel sufficiently to initiate nuclear production. The D^3He reaction is particularly temperature dependent, and so its production history will often have an additional feature, where the instant of maximum production during this phase is known as shock-bang time (6).

The reflected shock soon encounters the imploding shell (7), thus marking the beginning of the deceleration phase (IV), during which the shell is decelerated by about 10^{15} m/s^2. The convergent compression and heating of the fuel increases its density and temperature sufficiently for nuclear reactions to occur, where the maximum nuclear production rate is labeled as compression-bang time (8) (or sometimes just "bang-time"). This compression burn is characterized by a higher density and lower temperature than at shock-bang time (4 g/cm^3 and 3 keV at compression-bang time, versus 0.1 g/cm^3 and 8 keV at shock-bang time, see Figure 2-8).

[9] The critical surface is the surface where the plasma frequency equals the laser frequency. For a wavelength of 0.351 μm in a CH plasma, this occurs where the mass density is ρ_{crit} = 0.027 g/cm^3.

[10] A Mbar of pressure is equal to 10^{11} Pa, or approximately 10^6 atmospheres.

[11] Shock coalescence (4) does not always occur before the laser turns off (3) – the time order depends on the details of the laser pulse and capsule parameters.

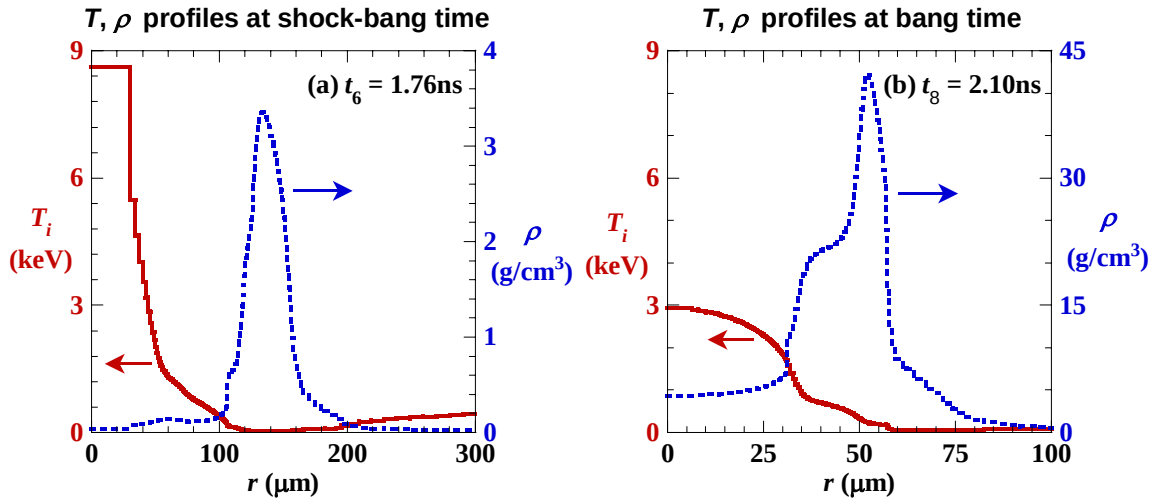

Figure 2-8: Simulated mass density and ion temperature profiles of shot 38525 at (a) shock-bang time (1.76ns) and (b) compression-bang time (2.10ns).

The extreme densities and temperatures raise the pressure in the fuel to a maximum of 15,000 Mbar, which rapidly decelerates the shell, until stagnation (9), where it is at a stop. In the reexpansion phase (V), the stagnated capsule expands and cools, which soon quenches the nuclear production.

2.4 Challenges

Many scientific and engineering challenges must be understood and overcome in order to obtain ignition and high gain in ICF. Drivers must be constructed to deliver a few MJ of energy in just a few ns in a precisely controlled way. Spherical targets must be fabricated with uniform layers of DT ice and maintained at temperatures near 19.8 K (the triple point of DT) before being shot by the driver.

Even with drivers and targets in hand, attaining ignition and optimal gain requires proper understanding of the coupling of the driver to the target and the reaction of the target to the absorbed driver energy. For laser drivers, details of the absorption of high-intensity ($\sim 10^{15}$ W/cm^2)[12] laser light are still not thoroughly understood – a number of laser-plasma instabilities [20] can degrade the achievable gain with a given driver energy.

The pressure and energy content of a material at different densities and temperatures are generally described as the material's equation of state (EOS). The EOS bears directly on the energy required to compress and heat a material to a given density and temperature, and also has significant impact on implosion dynamics such as shock propagation and thermal conduction. The EOS of many materials is not precisely known at the extreme conditions relevant to ICF.

In addition to the challenges that occur in the idealized, "1-D" picture of ICF implosions, numerous additional problems arise when considering the 3-dimensional nature of actual ICF implosions. The growth of various hydrodynamic instabilities greatly amplifies any initial non-uniformities, which can result in dramatically asymmetric implosions. Asymmetric implosions

[12] For reference, the intensity of the sun at the earth's surface on a sunny day is less than 0.1 W/cm^2.

will always perform worse than symmetric implosions driven with equivalent energy. The mitigation of hydro-instabilities puts stringent symmetry requirements on the laser illumination and the capsule fabrication. The remainder of this section will review the basics of these hydrodynamic instabilities.

2.4.1 The Rayleigh-Taylor Instability

The Rayleigh-Taylor (RT) instability [32][33] is considered one of the greatest challenges to the success of ICF, and detailed explanations of RT and other hydrodynamic instabilities can be found many places in the literature (e.g. References [17], [19], and [22]).

When a fluid of density ρ_1 supports a heavier fluid of density ρ_2, the fluid interface is RT unstable[13]. Small perturbations of initial amplitude h_0 grow exponentially in time, $h(t) = h_0\, e^{\gamma t}$. The classical RT growth rate of a perturbation of wave number $k = 2\pi/\lambda$ is given by:

$$\gamma_{RT} = \sqrt{A_t\, k\, g}\,, \tag{2-18}$$

where g is the acceleration, and A_t is the Atwood number,

$$A_t = \frac{\rho_2 - \rho_1}{\rho_2 + \rho_1}\,. \tag{2-19}$$

For classical RT growth, perturbations with the shortest wavelengths grow fastest.

The RT growth rate is reduced from its classical value when the effects of ablation and finite density gradients are included. The density profile between two fluids typically varies continuously with a scale length $L_\rho = \rho|d\rho/dr|^{-1}$ rather than as a sharp discontinuity at the fluid boundary. This density gradient has a minimal effect on perturbations with long wavelengths, but will reduce the growth rate for perturbations with wavelengths less than L_ρ. Ablation of the high density material will also reduce the growth rate of the RT instability, and will even stabilize the shortest wavelengths.

An approximation for the growth rate of the RT instability for a directly-driven CH ablator material over a wide range of thicknesses and laser intensities is given by Betti *et al* [34]:

$$\gamma_{abl} = \sqrt{\frac{k\, g}{1 + kL_\rho}} - \beta\, k\, v_a\,, \tag{2-20}$$

where $0.7 < L_\rho < 1$ μm, v_a is the ablation velocity, and β is a constant equal to 1.7.

The rapid, exponential growth of the perturbations saturates when the amplitude becomes comparable to the wavelength. The growth then enters a nonlinear regime where "spikes" of the heavy fluid penetrate into the light fluid, and "bubbles" of the light fluid rise into the heavy fluid. In the nonlinear regime, spike and bubble amplitudes grow quadratically in time [35]:

[13] A familiar example of the RT instability is the interchange of oil and water when a bottle containing both is overturned. An alternative but equivalent way to produce the RT instability is to accelerate a heavy fluid with a lighter fluid. In fact, any region where the gradients of density and potential (whether a gravitational or pressure potential) are opposed will be RT unstable.

$$h(t) = \alpha_{RT} A_t \, g \, t^2 , \tag{2-21}$$

where α_{RT} is a constant that is near 0.05 for bubbles, and for spikes varies between 0.05 (same rate as bubbles) and 0.5 (free fall) as A_t varies between 0 ($\rho_2 \approx \rho_1$) and 1 ($\rho_2 >> \rho_1$).

As the spikes and bubbles continue to interpenetrate, velocity shear between the two fluids results in further instability (the drag-driven Kelvin-Helmholtz instability: see the following subsection), which eventually causes the spike tips to "mushroom" and roll up on increasingly finer scales, thereby increasing the vorticity of the flow and eventually leading to atomic-scale mixing of the two fluids. A schematic of the linear and nonlinear growth phases of the RT instability is shown in Figure 2-9.

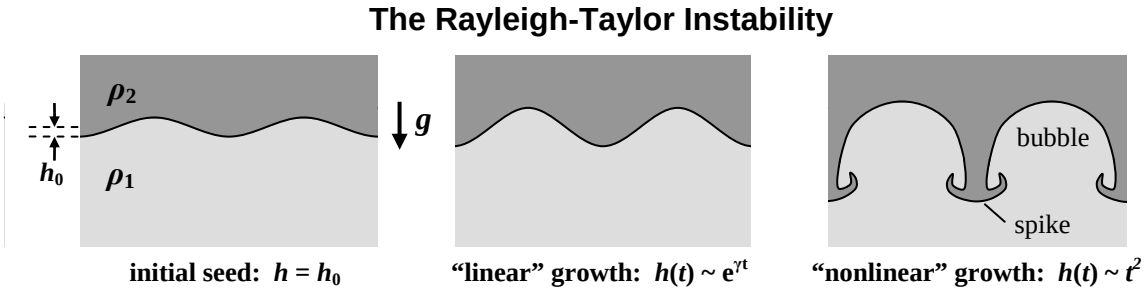

Figure 2-9: Linear and nonlinear growth of perturbations due to the Rayleigh-Taylor instability. When a light fluid (ρ_1) supports a heavy fluid (ρ_2) against an acceleration field (in this example, consider gravity pulling down), any initial perturbation seed (of amplitude h_0) will at first grow in a linear fashion, and eventually saturate into a nonlinear regime. An unfortunate naming convention leaves us with the fact that the amplitude grows exponentially with time during the linear phase, and quadratically with time during the nonlinear phase.

In ICF, RT-unstable surfaces exist during both the acceleration and deceleration phases. The low density ablating mass pushes against the high density "payload" during the acceleration phase, and after further convergence and compression, the high density shell is stopped by the low density hot-spot during the deceleration phase. Initial perturbations are seeded by laser and target nonuniformities, and growth of these perturbations during the acceleration phase can feed through to the inner surface and contribute to seeding perturbations for the deceleration phase.

Unmitigated RT growth during the acceleration phase can eventually break through the shell, which will compromise its compressibility and reduce the attainable areal density of the assembled target at stagnation. RT growth during the deceleration phase can send spikes of cold, dense fuel into the nascent hot-spot, potentially disrupting its formation. Even if the spikes do not reach the center, their penetration and the resultant mixing of the cold, dense shell with the hot, low density hot-spot will cool the outer regions of the hot-spot and reduce the volume participating in nuclear production. Reduction of the hot-spot temperature and volume will result in lower yields, which, if low enough, could fail to ignite the capsule.

2.4.2 Other Hydrodynamic Instabilities

The drag-driven Kelvin-Helmoltz (KH) instability arises when layers of fluids are in relative motion, where viscous forces amplify perturbations in regions of shear flow. Like the RT instability, the KH instability initially grows exponentially with time, $h(t) = h_0 \, e^{\gamma t}$. In the simplest

case of equal density fluids under zero acceleration and with no surface tension, a tangential velocity discontinuity Δu will result in a KH growth rate of:

$$\gamma_{KH} = k\left|\Delta u\right|, \tag{2-22}$$

where k is the wave number of the perturbation parallel to the direction of the velocity difference. Perturbations orthogonal to the velocity shear experience no growth.

Later in time, when the amplitude becomes comparable to the wavelength, the "tops" of the perturbations are pushed in the direction of the fluid flow, and the interface begins to roll up. This phenomenon occurs in late stages of RT growth, and is responsible for the "mushrooming" of spike tips (see Figure 2-9). Rolling up on progressively finer scales eventually reaches the atomic scale, and the two fluids will be atomically mixed.

The growth of perturbations on an interface that is accelerated by the passage of a shock is known as the Richtmyer-Meshkov (RM) instability (see Figure 2-10). The initial perturbation amplitude will be amplified linearly in time, $h(t) = h_0(1 + \gamma_{RM}\, t)$, where γ_{RM} is the RM growth rate. If the shock impulsively accelerates an interface, changing the interface velocity by Δu, then perturbations of wave number k will have a RM growth rate of:

$$\gamma_{RM} = A_t\, k\, \Delta u, \tag{2-23}$$

where A_t is the Atwood number.

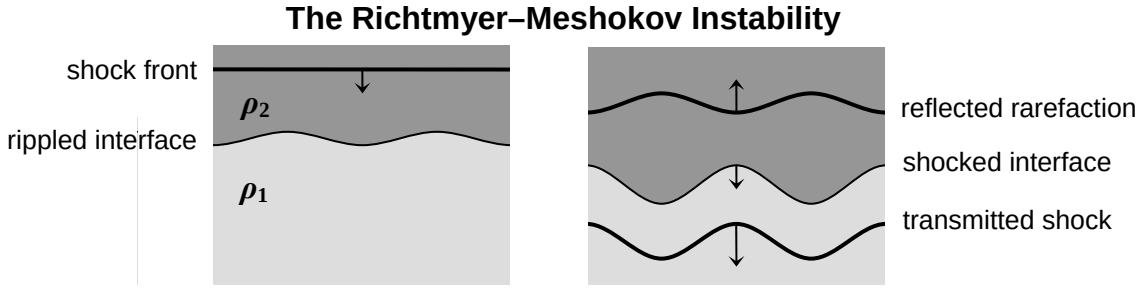

Figure 2-10: The incidence of a planar shock on a rippled density interface results in a perturbed transmitted shock and reflected rarefaction, as well as an impulsive acceleration of the interface. Richtmyer-Meshkov growth is the linear growth in time of the interface ripples after the passage of the shock. Shown here is the situation of a shock passing from a heavier fluid (ρ_2) into a lighter fluid (ρ_1), but the phenomenon also occurs for shocks traveling in the other direction.

RM growth is generally considered less of a problem for ICF than RT growth, since the amplification is linear in time rather than exponential. RM growth of initial surface perturbations on the fuel-shell interface induced by shock breakout is still a concern, however, since it can increase the seed amplitude for the RT instability before the onset of the deceleration phase.

More thorough explanations of the KH and RM instabilities can be found in, for example, References [19] and [22].

2.5 The OMEGA facility

All experiments described in this thesis were performed at the OMEGA laser facility [29][30], located in Rochester, New York at the Laboratory for Laser Energetics (LLE). It is a 60-beam, neodymium-glass laser capable of delivering up to 30 kJ at a wavelength of 351 nm at a shot rate of about 1 per hour. A variety of pulse shapes are possible, with durations ranging from 100 ps to 3 ns. Individual beam timing can be controlled to 10 ps, and the beams can be pointed with an accuracy of 16 μm.

Phase plates [36] can be inserted to control the spatial beam shape. The "SG4" phase plates, installed in May 2003, produce an intensity profile that is a super-Gaussian of order 3.7 and with a 95% enclosed energy diameter of 865 μm at the focal plane. High-mode intensity nonuniformities can optionally be smoothed using polarization smoothing, and using 2-D smoothing by spectral dispersion (SSD) with a 1 THz bandwidth [37]. The overall irradiation uniformity can thus be controlled to better than 2% rms on a spherical surface of radius 865 μm.

The OMEGA target chamber is a 3.3 m diameter spherical vacuum chamber with a typical operating vacuum of 10^{-5} Torr. It has 60 beam ports and 32 diagnostic ports, up to 10 of which can be used for charged particle diagnostics (see Figure 2-13). The target is positioned at the target chamber center (TCC) within 5 μm.

Cryogenic targets are scaled from ignition designs on the National Ignition Facility (NIF) (see Figure 2-6 and Reference [28]). Cryo-surrogate "warm" targets have mass-equivalent shells made of plastic. They are typically 860-880 μm in diameter, and are filled with gaseous fusion "fuels" such as DT, pure D_2, or D_2 and ^{3}He. Although DT fuel will be used in the first ignition experiments, D_2 and D^{3}He fuels are commonly used in surrogate implosions for diagnostic purposes and due to ease of handling compared to the radioactive tritium fuel.

Targets for the set of experiments described here had shell thicknesses between 15 and 27 μm, gaseous fill pressures between 3 and 20 atm, and fill compositions of pure D_2, pure ^{3}He, and mixtures of D_2 and ^{3}He. The "reference" target has 20 μm of CH (composition ratio = 1.38 H per C), and is filled with 6 atm of D_2 and 12 atm of ^{3}He (at room temperature, 293 K). The driving laser pulse is a 1-ns flat top, with 100 ps rise and fall times, SG4 phase plates, and a total laser energy of 23 kJ. Targets are typically treated with a flash coating of Aluminum (about 100 nm thick) to reduce the leak rate of the fill gases as the target is placed at TCC.

OMEGA has been the workhorse for the U.S. Inertial Fusion program for over five years, and will continue to be an extremely important experimental facility even after the expected completion of the National Ignition Facility (NIF) [14] at the Lawrence Livermore National Laboratory (LLNL) in 2010.

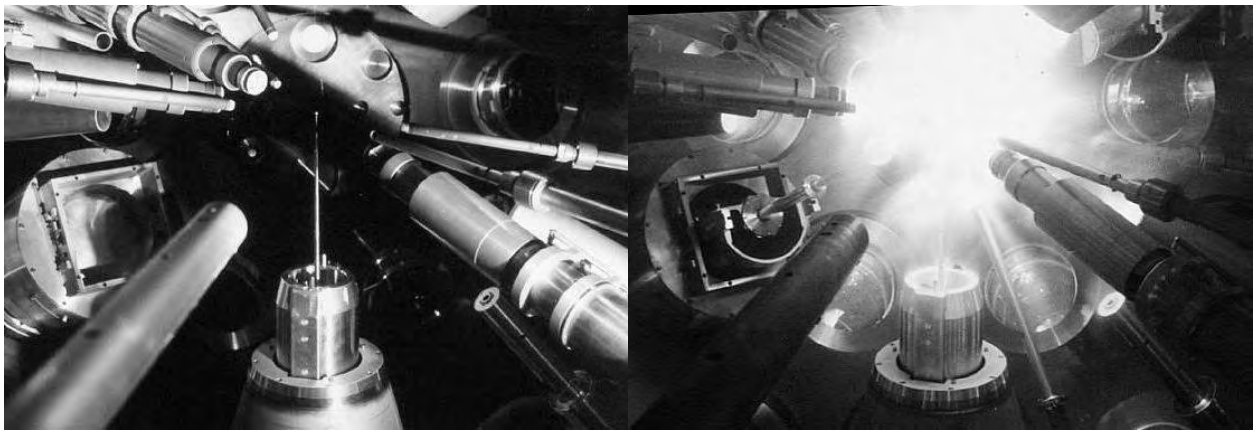

Figure 2-11: An implosion at the OMEGA laser facility. The left image was taken shortly before the shot – reflection off the 1-mm-diameter target is just visible in the upper middle of the photograph. The right image was taken during the implosion.

Figure 2-12: The OMEGA target bay during the installation of the CPS-2 diagnostic. The CPS-2 housing contains 4000 lbs of lead and polyethylene shielding to reduce the neutron background on the detectors.

2.6 ICF diagnostics

A large suite of diagnostics is available on the OMEGA facility; these diagnostics are used to determine capsule conditions at different times during the implosion, and to reveal how those conditions deviate from what was expected. The suite includes diagnostics for spatial, spectral, and temporal measurements of photons, neutrons, and charged-particles. Measurements of photons in the optical and x-ray bands provide a rich and diverse view of implosion dynamics, and dominate the literature. In this thesis, the focus will be on diagnostics of nuclear products, which include neutrons and charged-particles, with particular focus on 14.7 MeV D^3He protons emitted from the capsule during nuclear burn.

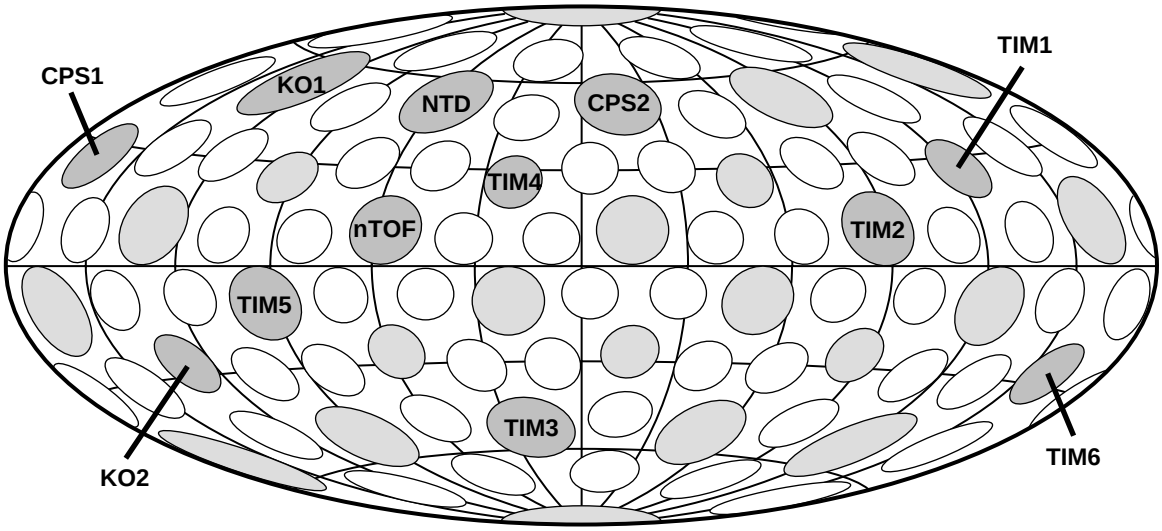

Figure 2-13: OMEGA target chamber port diagram. There are 60 laser beam ports (white) and 32 diagnostic ports (grey).

The 3.2 m diameter OMEGA target chamber has 32 diagnostic ports, of which two are dedicated to neutron diagnostics (NTD and nTOF), two to magnet-based charged-particle spectrometers (CPS), and 8 others which can be used for additional charged particle diagnostics (KO and TIM). Figure 2-13 shows the layout of these ports in an Aitoff projection of the OMEGA target chamber.

2.6.1 Nuclear Products and Spectra

The yield of primary fusion reactions provides one of the most fundamental indicators of implosion performance, and is the observable that must be maximized for a given driver energy to produce high gain implosions for energy production. The yield is the total number of fusion reactions of a particular reaction type that occurs during the shot.[14] The thermonuclear yield Y for the reaction $A + B \rightarrow C + D$ is the spatial and temporal integral of the product of the reactant densities (n_A, n_B) times the local thermal reactivity ($\langle\sigma v\rangle_{AB}$):

[14] The yield is sometimes measured as the total nuclear energy released during the shot.

$$Y_{AB} = \int \frac{1}{1+\delta_{AB}} n_A\, n_B\, <\sigma v>_{AB}\, d^3\vec{r}\, dt\,, \tag{2-24}$$

The temperature (which determines $<\sigma v>_{AB}$) and the densities are in general functions of space and time, and δ_{AB} is the Kronecker delta – equal to one if A and B are the same type of particle, and equal to zero otherwise. This term corrects for the double counting of identical particles.

In addition to yields of thermonuclear reactions among fuel ions ("primary" yields), there are other, non-thermal processes that can result in fusion production. A "secondary" reaction can occur if a product from a primary reaction (such as the T or ^{3}He products from DD-p and DD-n reactions) fuses with a fuel ion (typically a D) before it escapes the capsule or slows down to thermal temperatures. "Knock-on" (KO) interactions are the result of elastic scattering of ions in the capsule by primary neutrons. Table 2-5 lists relevant primary, secondary, and knock-on nuclear interactions, as well as the range of yields on OMEGA.

Secondary and knock-on yields depend on details of the implosion, and are typically of order 10^{-3} and 10^{-4} per primary reaction, respectively. Because neutrons are very penetrating, the yield of down-scattered neutrons from KO interactions scales linearly with the areal density for all ρR's of interest to ICF. However, for ρR's above 100-250 mg/cm^2, KO charged particles will start to range out (depending on the KO particle species). Secondary yields scale linearly with areal density only if the areal density is small (≤ 3 mg/cm^2). At higher areal densities, the primary products get ranged out and the secondary yield saturates [38].

The energy released in a fusion reaction (Q) takes the form of kinetic energy of the fusion products, which is split according to their relative mass. The mean energy of primary fusion product "C" in the reaction A + B → C + D is [39]:

$$\langle E_C \rangle = \frac{m_D}{m_C + m_D} Q\,. \tag{2-25}$$

Small thermal and relativistic [40] corrections, of order T/Q and Q/M, respectively, have been neglected, where T is the temperature and M is the total reactant mass, $M = m_A + m_B$.

The energies of thermonuclear fusion products are broadened about their mean energies due to the variation in collision velocities of reactants in a thermal plasma. The resulting thermonuclear product spectra are well approximated by Gaussian energy distributions of the form:

$$f(E_C) \propto \exp\left[-\frac{\left(E_C - \langle E_C \rangle\right)^2}{2\Sigma^2}\right], \tag{2-26}$$

where the variance Σ^2 is due to thermal (or "Doppler") broadening:

$$\Sigma^2 = \frac{2 m_C m_D}{(m_C + m_D) M} QT\,. \tag{2-27}$$

The energy spectra of secondary fusion products are much broader than their primary counterparts, since in this case one reactant (the DD-p or DD-n primary product) has an energy much greater than the thermal energy. The energy spectra of knock-on particles are continua that

reach upper endpoints determined by kinematics. Table 2-5 lists the mean energies and standard deviations of primary product spectra, as well as the energy range of secondary and knock-on product spectra.

Table 2-5: Nuclear interactions, with product energies and the range of OMEGA yields. The mean (E_C, E_D) and standard deviation (Σ) of the primary product spectra are shown for primary reactions. Subscripts "C" and "D" denote the first and second nuclear products, respectively. For Σ, T_i is the ion temperature in keV.

Reaction type	Reaction	Y	E_C (MeV)	E_D (MeV)	Σ (keV)
primary	D + T → ^{4}He + n	10^9-10^{14}	3.54	14.05	75.1 $\sqrt{T_i}$
"	D + ^{3}He → ^{4}He + p	10^6-10^{12}	3.69	14.66	76.6 $\sqrt{T_i}$
"	D + D → ^{3}He + n	10^7-10^{12}	0.82	2.45	35.0 $\sqrt{T_i}$
"	D + D → T + p	10^7-10^{12}	1.01	3.02	38.9 $\sqrt{T_i}$
secondary	D + T(≤1.01 MeV) → ^{4}He + n	~$10^{-3}\times Y_{DD}$	1.4-6.7	11.8-17.1	
"	D + ^{3}He(≤0.82 MeV) → ^{4}He + p	"	1.7-6.6	12.5-17.4	
knock-on	n (14.1 MeV) + p → n' + p'	~$10^{-4}\times Y_{DT}$	≤14.1	≤14.1	
"	n (14.1 MeV) + D → n' + D'	~$10^{-5}\times Y_{DT}$	≤14.1	≤12.5	
"	n (14.1 MeV) + T → n' + T'	~$10^{-5}\times Y_{DT}$	≤14.1	≤10.6	

The spectra of nuclear products can be further modified when the particles travel through the compressed plasma as they escape the capsule. A small fraction ($\leq 10^{-4}$) of the neutrons scatters elastically in the compressed capsule, producing knock-on particles and down-scattered neutrons. Small angle scattering off plasma electrons and ions will cause charged particles to experience energy loss as they traverse the plasma. The energy loss of charged particles is strongly dependent on the plasma temperature when the velocity of the fusion-product particles (v_p) is smaller than the thermal velocity of background electrons (v_{te}), but when $v_p > v_{te}$, energy loss only depends on the energy of the fusion product.

An energetic particle of energy E_p, atomic number Z_p, and atomic mass number A_p will experience energy loss to the plasma electrons as a function of distance according to [41]:

$$\frac{dE_p}{dx} = -\frac{2\pi}{m_e}\left(\frac{e^2}{4\pi\varepsilon_0}\right)^2 \frac{{Z_p}^2 A_p}{E_p}\frac{Z_b\rho}{A_b} G(x_{p/e}) \ln\Lambda\,, \tag{2-28}$$

where Z_b, A_b, and ρ are the average atomic number, average atomic mass number, and mass density of the background plasma, respectively. The square of the ratio of the energetic particle velocity to the electron thermal velocity, $x_{p/e} = (E_p\, m_e/T\, m_p)^2$, is used as the argument for $G(x)$, a function defined in Reference [41], which scales as $x^{3/2}$ for $x<<1$, and saturates at 1 for $x>>1$. The Coulomb logarithm $\ln\Lambda = \ln(\lambda_D/r_{\min})$ is the ratio of the DeBye length, $\lambda_D = (\varepsilon_0\, T / n_e\, e^2)^{1/2}$, to the quadrature sum of the classical impact parameter for 90º scattering and the electron DeBroglie wavelength: $r_{\min} = [(Z_p e^2/3m_e u^2)+(\hbar/2m_e u)^2]^{1/2}$. Here, n_e is the plasma electron number density, and u is the average relative velocity. The fundamental constants m_e, e, ε_0, and $\hbar$ are the electron mass, fundamental charge, electric constant, and reduced Planck's constant, respectively. For high densities ($n_e > 10^{24}/\text{cm}^3$), electron quantum degeneracy effects should also be included. The formulation for energy loss to plasma ions is similar to that shown here for energy loss to plasma electrons, but for conditions of interest to ICF, ions contribute <10% of the total energy loss rate.

By re-expressing Equation (2-28) in terms of the energy loss per unit areal density ($dE/d\rho R$), it can be seen that the energy loss of energetic particles is a weak function of the plasma density (entering only through the weakly-varying coulomb logarithm) and composition (varying as Z_b/A_b, which is near 0.5 for most materials). In particular, for protons the energy loss per unit areal density can be expressed as:

$$\frac{dE_p}{d(\rho R)} \propto -\frac{1}{E_p} G(x_{p/e}), \tag{2-29}$$

where the variation due to the Coulomb logarithm is neglected. The essential feature of this expression is that when the proton velocity is much higher than the electron thermal velocity, $G(x)$ saturates at 1, and the energy loss is independent of the plasma temperature, varying only as the inverse of the proton energy.

The weak dependence of charged-particle energy loss on plasma conditions contrasts starkly with the very strong dependence of x-ray attenuation on plasma conditions. For example, the strength of the inverse Bremsstrahlung process, the dominant x-ray absorption mechanism in a fully ionized plasma, varies with plasma conditions as: $\rho^2\ T^{1/2}\ Z_b{}^3/A_b{}^2$. X-ray attenuation has an even stronger temperature and composition dependence if the plasma is not fully ionized. These differences between x-ray and charged-particle energy loss makes charged-particles a much more useful probe of areal density when plasma conditions are not precisely known.

Figure 2-14 shows $dE/d\rho R$ as a function of energy for protons passing through CH plasmas with various densities and temperatures. Relatively small correction factors are needed for plasmas of different compositions. For example, energy loss in D^3He plasmas differs by less than 10% from that in CH plasmas (compared to a ~76% difference for inverse Bremsstrahlung). A change in the mass density by a factor of 10 changes $dE/d\rho R$ by only 15%, demonstrating the weak density dependence (compared to a ~10,000% difference for inverse Bremsstrahlung). The temperature dependence is extremely weak while the energetic proton speed is much greater than the electron thermal speed, as is the case for 14.7 MeV protons for electron temperatures less than ~1 keV.

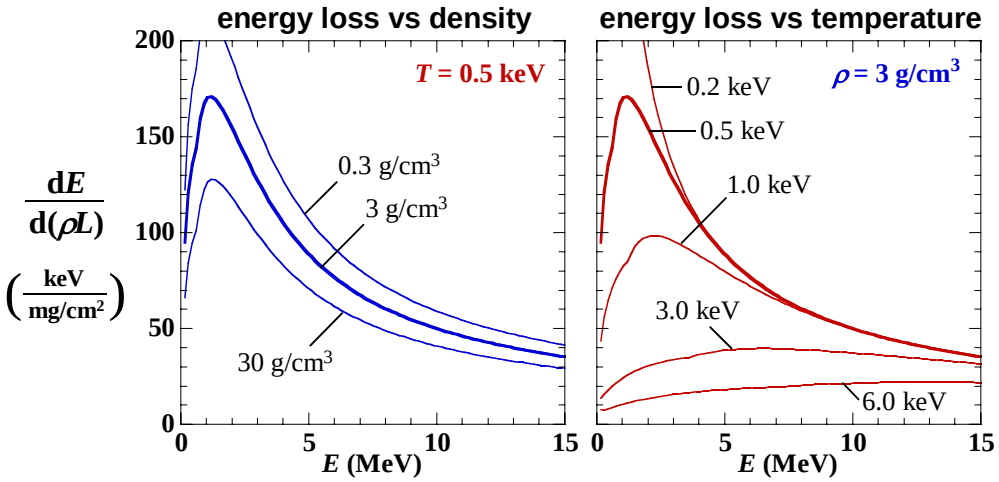

Figure 2-14: Energy loss per unit areal density ($dE/d\rho R$) as a function of energy for protons passing through CH plasmas characteristic of ICF implosions. Of particular importance is the weak dependence of $dE/d\rho R$ on temperature (for T≤1 keV) and density for proton energies near 14.7 MeV.

The weak dependence of the energy loss of 14.7 MeV protons on density, temperature, and composition makes the downshift of D^3He protons from their birth energy an excellent probe of the areal density of an imploded capsule. In practice, D^3He protons are a useful probe of ρR's up to about 200 mg/cm^2 [42], after which they are ranged out (lose all of their energy in the plasma). For higher ρR's, other methods, such as measurement of downscattered neutrons [43], must be used to determine ρR.

Under special circumstances, charged particles can also sometimes be upshifted from their birth energies [44]. Strong electric fields are created when hot electrons, generated by laser-plasma instabilities in the corona, escape into the surrounding vacuum. These (primarily radial) electric fields decay shortly after the laser pulse turns off, but if nuclear bang time occurs while the laser pulse is on, they will experience acceleration and gain several hundred keV in energy. If the areal density was also low, there will be a net upshift in the mean of the spectrum from the product birth energy. This situation can occur for implosions of capsules with very thin shells (2-3 μm thick). For all experiments discussed in this thesis, the laser pulse turns off well before the nuclear products are emitted, so the products experience negligible acceleration.

2.6.2 Yield and Spectral Diagnostics

The total neutron yield from ICF implosions can be determined by absolutely calibrated neutron activation diagnostics [45]. A sample of suitable activation material placed near the target will be rendered radioactive in proportion to the neutron fluence it intercepts. Activation of ^{63}Cu is used for 14.1 MeV DT neutron yields, and activation of ^{115}In is used for 2.45 MeV DD neutron yields. The neutron yield can also be measured through numerous other methods, including detection using current-mode scintillators [46], recoil protons [43][47], and nuclear track detectors [48].

In addition to the neutron yield, scintillator-based neutron time-of-flight (nTOF) detectors [46] can also give some limited spectral information. Thermal broadening of the neutron spectrum results in broadening of the arrival time at the detector. Assuming a Gaussian energy distribution as discussed in the previous subsection, the Σ of the neutron energy distribution can be inferred from the temporal duration of neutron arrival times. Σ, in turn, can be used to infer a mean ion temperature, which is weighted by the spatial and temporal distribution of the neutron production.

On OMEGA, nTOF scintillators are placed at 1.7, 3, 5.4, 12, and 20 meters from TCC and run simultaneously to give a large dynamic range of neutron yield sensitivity while maintaining adequate temporal resolution. The nTOF detectors are cross-calibrated with each other, and the yield is also cross-calibrated with activation yield measurements. This results in yield measurements with an absolute calibration uncertainty of approximately 10% over a wide range of neutron yields (~10^6-10^{14}). The temporal resolution of the nTOF detectors is good enough to achieve about a 0.5 keV uncertainty in the inferred neutron-burn-weighted ion temperature for temperatures above 2 keV.

A number of different kinds of detector have been suggested and implemented for charged nuclear products emitted from ICF implosions; these include solid-state nuclear track detectors, scintillators, CCDs, and other electronic detectors. Solid-state track detectors have been used with much success in ICF environments due to their relative insensitivity to the electromagnetic, x-ray, and neutron induced noise compared to electronic detection. For detection of low-mass

energetic nuclear particles (such as protons), CR-39 is the solid state nuclear track detector of choice.

CR-39[15] is a clear thermosetting plastic whose chemical composition is $C_{12}H_{18}O_7$. When an energetic charged particle passes through, it leaves a trail of damage along its path in the form of broken molecular chains and free radicals. The amount of local damage along the path is related to the local rate at which energy is lost by the particle (*dE/dx*, where *x* is the distance along the path). Etching the CR-39 in sodium hydroxide (NaOH) results in conical pits at the locations where the charged particles passed through the surface. These pits, or "tracks", are visible under the microscope (see Figure 2-15), and their diameters provide a measure of *dE/dx* for the incident particle. The energy and species of the incident particle can then be determined using the dependence of *dE/dx* on particle species and energy. Figure 2-15 shows the proton track diameter as a function of proton energy for CR-39 etched in 6.0 molar NaOH at 80 ºC for 6 hours.

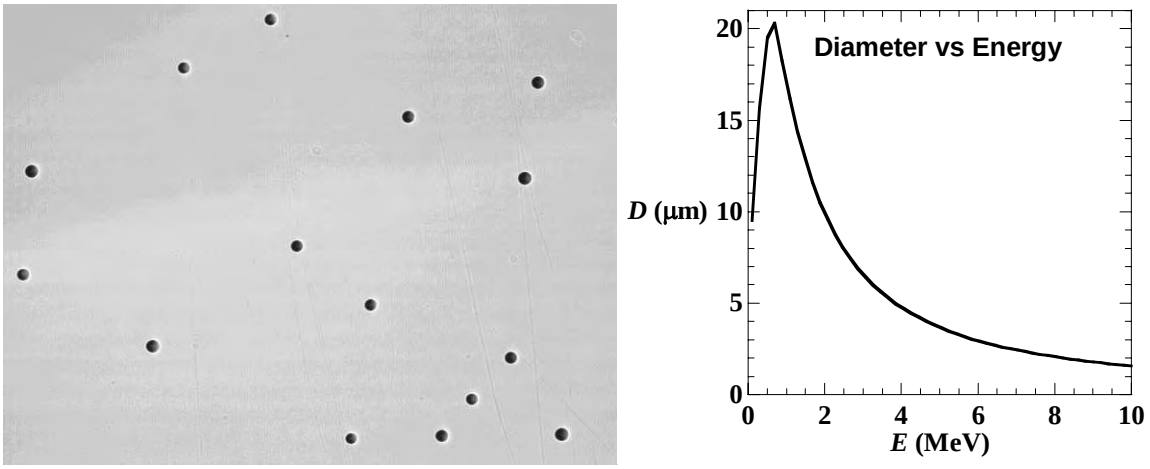

Figure 2-15: (left) Microscope image of a section of etched CR-39 nuclear detector, showing tracks left by incident 3 MeV protons. The image size is 410 x 310 μm. (right) Proton track diameter as a function of incident proton energy on CR-39, after etching for 6 hours at 80 ºC in 6.0 molar NaOH.

CR-39 has been used extensively as a detector for charged-particle spectrometry of ICF fusion products [42]. CR-39 has also been successfully used as an imaging detector to measure the spatial nuclear production profile (see Subsection 2.6.4), and to measure transient electric and magnetic fields through proton deflectometry [49].

Two magnet-based Charged-Particle Spectrometers (CPS) [42][50] are in regular use at the OMEGA facility. Each CPS uses a 7.6 kG permanent magnet in conjunction with CR-39 detectors. Protons or other charged particles enter through a collimating aperture, are deflected by the magnetic field, and are detected by pieces of CR-39.

Particle trajectories through the CPS magnets are characterized by their gyroradius R_{gyro}, which increases with particle energy as:

[15] "Columbia resin #39" is the 39th resin formula developed by the Columbia laboratories. In addition to its scientific use as a nuclear track detector, it is also commonly used in many everyday objects, such as eyeglasses, safety screens, and observation windows.

$$R_{gyro}^2 \propto (A/Z^2)E\,, \tag{2-30}$$

where Z is the atomic number, and A is the atomic mass number. The magnet was designed for values of $(A/Z^2)E$ extending from 0.05 to 30 MeV (see Figure 2-16). If A and Z are known, the particle energy can be directly determined from the detection location. Multiple species of charged particle having the same R_{gyro} can be easily distinguished by the different track diameters they leave in the CR-39. Figure 2-17 shows the results of simultaneous measurement of five different charged particle species by CPS-2.

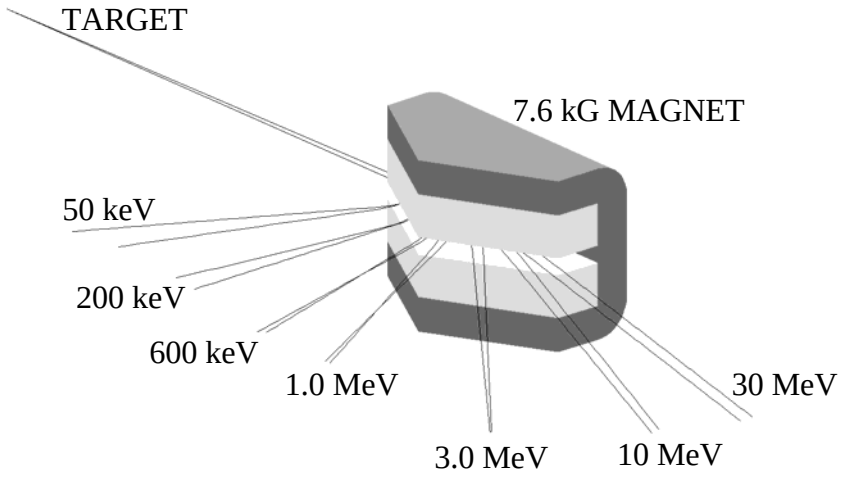

Figure 2-16: The 7.6-kG charged-particle spectrometer (CPS) magnets disperse charged particles according to gyro-radius. Trajectories of protons with selected energies are shown. Particle species can be distinguished by the track diameter on the CR-39 detectors (not shown).

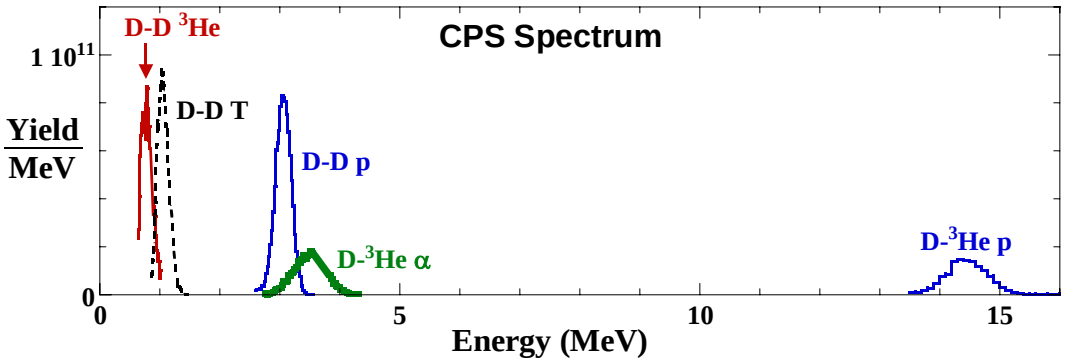

Figure 2-17: The charged particle spectrum from shot 20297 measured by CPS-2, demonstrating the simultaneous measurement of 5 different primary nuclear products.

The CPS collimating aperture can be adjusted from 0.01 to 1.0 cm. For aperture widths wider than about 0.1 cm, there is a tradeoff between instrument sensitivity and energy resolution, with higher sensitivity and lower resolution for wider apertures. Aperture widths narrower than 0.1 cm give minimal gains to the energy resolution, but allow detection of particles of very high yield without saturating the detector.

The dynamic range of particle yield measurement by CPS is over 10^4, and the detectable yield range can be extended by another factor of 10^2 by appropriate choice of the collimating aperture width. The collimating apertures are 1.5 cm high, and are located at distances of 235 cm (for CPS-1) and 100 cm (for CPS-2) from TCC. The range of detectable yields depends on the energy and spectral width of the particles of interest, but for primary yields ranges from about 2×10^7 to 4×10^{13} for CPS-2, and from about 1×10^8 to 2×10^{14} for CPS-1. Measurement of the ablator proton[16] spectrum below 1 MeV has been successful even for yields above 10^{15}/MeV [51].

The absolute energy calibration of the CPSs is accurate to ±0.02 MeV for 3 MeV protons, and ±0.1 MeV for 15 MeV protons. The energy response function for a mono-energetic proton beam is a square box with a width that is determined by the width of the collimating aperture; with a 0.1 cm width, the box has a standard deviation about the mean energy of 0.013 MeV for 3 MeV protons, and 0.19 MeV for 15 MeV protons.

Wedge-Range-Filter (WRF) proton spectrometers [42] can be used in any of the TIM or KO ports on the OMEGA target chamber, shown in Figure 2-13. The WRF design concept (see Figure 2-18) uses a wedge-shaped aluminum (Al) filter to range down the energy of incident protons, and a piece of CR-39 to detect the protons that are transmitted through the filter. The energy of the transmitted proton can be determined by its track diameter, measured on the etched CR-39. The energy of the incident proton can then be deduced using the thickness of the Al filter at the track position and the ranging characteristics of protons in Al. In addition to ranging down higher energy protons into the energy band most useful for energy analysis on the CR-39, the Al filter also shields the CR-39 from exposure to scattered light, x-rays, and debris from the implosion.

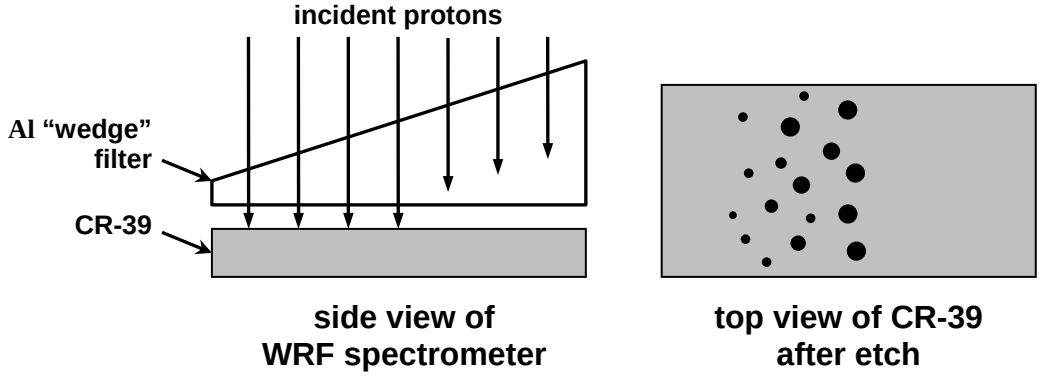

Figure 2-18: The Wedge-Range-Filter (WRF) spectrometer schematic. A wedge-shaped Al filter ranges down the energy of incident protons according to the local filter thickness. Protons with sufficient energy to penetrate the filter are incident on a piece of CR-39 nuclear detector. After the CR-39 is etched, the detected protons leave holes visible under a microscope. The diameter of the proton tracks and the local filter thickness are used to recover the incident energy of the protons.

The CR-39 area used for the proton spectrum in the WRF spectrometers is 2.4 × 2.4 cm in area. The entire spectrometer fits in a package with a 5 cm diameter, and can be placed as close as 10.5 cm from TCC. Their compact design allows the WRF spectrometers to be placed much closer to TCC than the CPSs, and so enable measurement of spectra when the proton yields are

[16] These protons are from the ablator material, and have been accelerated by radial electric fields around the capsule.

very low. In addition, the compact design can be simultaneously used in several ports, allowing comparison of spectra in multiple directions.

The Al thickness ranges between 400-1800 μm, giving the WRF spectrometers a detection bandwidth of 8-18 MeV. The WRF spectrometers have an absolute energy uncertainty of 150 keV, a resolution of 150 keV, and at 14.3 MeV, they have a precision of 70 keV.

The WRF proton spectrometers have a large dynamic range (>10^3), which can be further extended by adjusting the detector distance from TCC (10.5 to 180 cm), and by adjusting the etch time for high yield shots. Considering a typical spectral width of 3 MeV, the WRF spectrometers are insensitive to yields below 10^5, and can obtain good spectra at yields between 10^6 and 10^{11}. At yields above 10^{12}, information can still be extracted, but the detectors will be very saturated.

The background level for low neutron yields comes from intrinsic noise due to imperfections in the CR-39, and is 3×10^5/MeV at 10.5 cm and 9×10^7/MeV at 180 cm. For higher neutron yields (above 10^{10} at a WRF distance of 15 cm), the background increases linearly with Y_n.

Typical primary and secondary D^3He proton spectra measured with the WRF spectrometers are shown in Figure 2-19. The primary spectrum often shows two distinct components, corresponding to D^3He proton emission at shock-bang time and during the deceleration phase. Further compression of the shell takes place between these two times, and consequently the compression component undergoes additional downshift, producing the associated spectral separation. The secondary spectrum is broad and flat due to the kinematic distribution of energies resulting from the energetic ^3He reactant. The secondary spectrum also experiences downshift as it passes out of the compressed capsule.

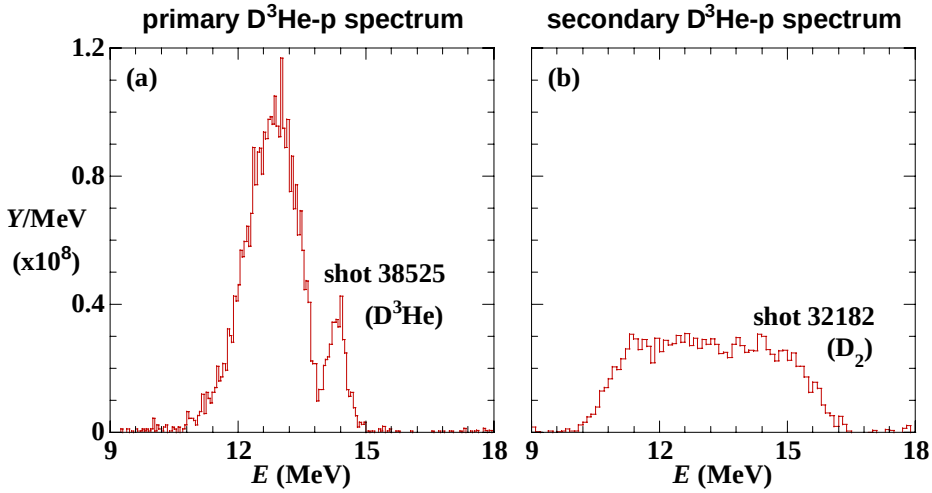

Figure 2-19: WRF spectra of (a) primary D^3He protons from shot 38525 (D^3He fuel) and of (b) secondary D^3He protons from shot 32182 (D_2 fuel). Both shots had the same CH shell thickness (24 μm) and the same laser energy (23 kJ).

Quantitative determination of the areal density of a capsule at bang time can be accomplished using these charged particle spectra. The mean downshift of energetic charged particles is proportional to the areal density traversed. Areal densities up to the range of the particle can be measured in this fashion. The energy of primary D^3He protons (birth energy 14.7 MeV) as a function of ρR traversed through plasmas characteristic of the shell at shock-bang time and

compression-bang time is shown in Figure 2-20. The D^3He protons penetrate over 200 mg/cm^2 in a typical CH plasma before being ranged out. For areal densities smaller than about 250 mg/cm^2, the areal density can be inferred from the downshift of the D^3He proton spectrum.

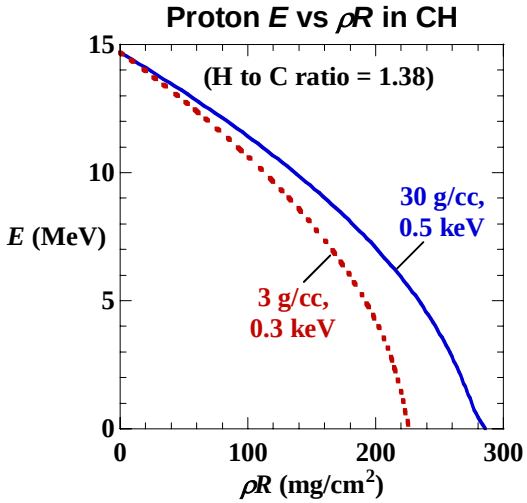

Figure 2-20: The resulting energy of 14.7 MeV protons launched through given areal densities of a plasma characteristic of the shell at shock-bang time (dotted red) and at compression-bang time (solid blue). The downshift of primary D^3He protons can thus be used to determine areal density at bang time for areal densities up to about 250 mg/cm^2.

Nuclear yields can also be used to deduce the fuel ion temperature at bang time. When products from more than one fusion reaction are measured simultaneously, the ion temperature (averaged over the nuclear production region) can be inferred using the known fuel composition and the theoretical thermal reactivities (from Figure 2-1), assuming the nuclear production regions are not too different in size. The DD-n to D^3He yield ratio is plotted as a function of ion temperature for an equimolar D^3He mixture in Figure 2-21. The yield ratio varies by over 3 decades for ion temperatures between 1 and 10 keV, which means the fractional temperature uncertainty will be much smaller than the fractional yield uncertainties.

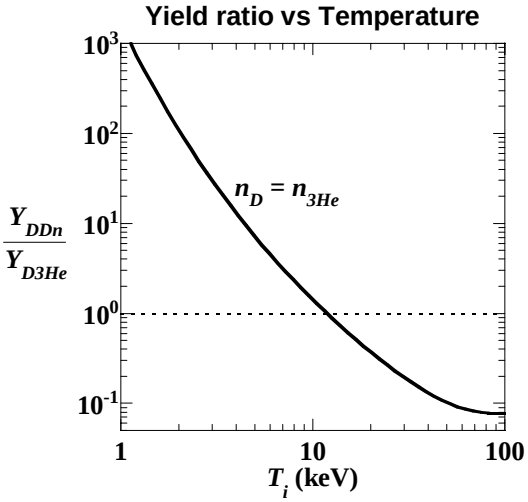

Figure 2-21: DD-n to D^3He yield ratio as a function of ion temperature, assuming a 50-50 D to ^3He composition ratio. Using measured yields and known fill composition, an average ion temperature can be inferred.

2.6.3 Temporal Diagnostics

Temporal diagnostics of nuclear products measure the timing and duration of nuclear production. Timing measurements are an important check to make sure simulations are properly treating the hydrodynamics, and the duration of nuclear production can provide insights on the confinement time, as well as deviations from ideal behavior.

Two nuclear temporal diagnostics are currently in use at OMEGA: the neutron temporal diagnostic (NTD) [52], which measures the DD-n production history, and the proton temporal diagnostic (PTD) [53][54], which measures the D^3He proton production history. These two diagnostics work on the same basic principle; the essential differences are the filter thickness and detector distance.

The principle of both diagnostics is excitement of a scintillating material (Bicron BC-422) by interactions with the nuclear product of interest (2.45 MeV neutrons for NTD, 14.7 MeV protons for PTD). A complex optical system collects the light emitted by the scintillator and transports it outside of the target chamber, where it is incident on a fast (<15 ps) streak camera. The streak camera records both the signal from the scintillator, as well as an optical fiducial pulse train from the master laser oscillator, which gives an absolute timing reference accurate to within 25 ps. Figure 2-22 illustrates the schematic of the temporal diagnostics using PTD as an example.

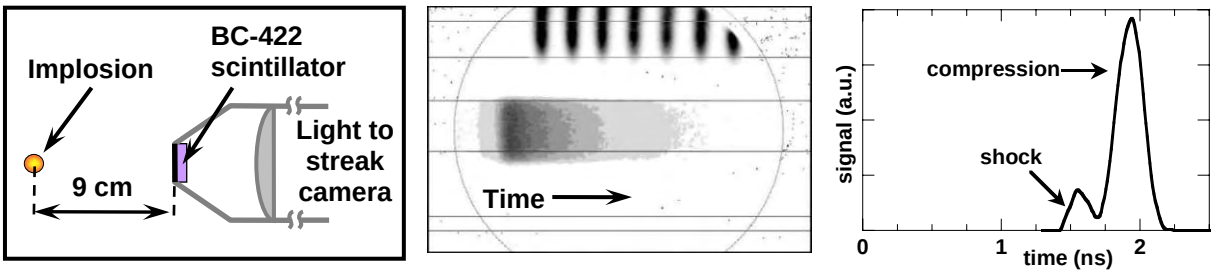

Figure 2-22: (a) Schematic of the Proton Temporal Diagnostic (PTD). Light emitted by the scintillator during the arrival of the D^3He protons is recorded by a streak camera. (b) Streak camera image. Because of the short rise and long decay time of the scintillator response, the reaction history is encoded in the leading edge of the central band. The dark vertical lines near the top are the optical fiducial signal. (c) Resulting burn history after the detector response has been deconvolved.

The scintillator has a very fast rise time of <20 ps, and a decay time of about 1.2 ns. Because the burn duration is short (~150 ps) compared to the decay time of the scintillator, the burn history information is encoded in the leading edge of the scintillator signal. Deconvolution of the scintillator response gives the resulting burn history for NTD, whereas the PTD burn history needs an additional stage of analysis to unfold the more complex proton spectrum and infer the D^3He burn history. This second analysis stage is described in detail in reference [54].

The NTD scintillator is placed 2 cm from TCC, and is shielded by a 1 mm thick nose-cone made primarily of tungsten. This filter shields the scintillator from stray light, x-rays, and charged particles (such as D^3He protons), so that it interacts only with the DD neutrons. To allow detection of D^3He protons, the PTD scintillator is shielded by a thinner filter made of 100 μm of Al and 100 μm of Ta. The PTD scintillator is placed 9 cm from TCC to enable it some time to

recover from the x-ray pulse that leaks through the filter. The DD neutrons pass through the PTD scintillator several nanoseconds after the D^3He protons, since they travel at less than half the speed (2×10^7 vs. 5×10^7 m/s). The scintillator has recovered from the D^3He proton signal by this point, so the simultaneous measurement of the DD-n bang time by the PTD can be used to give a relative timing accuracy with the NTD of better than 25 ps.

The burn histories measured by the diagnostics are broadened primarily through spectral broadening (D^3He-p) and by the transit time through the 1-mm-thick scintillator (DD-n). These effects limit the temporal resolution of the NTD to 45 ps, and the PTD to 25 ps for D^3He protons and 80 ps for DD-n. The background level for both diagnostics depends on the laser conditions and the nuclear yield, but is approximately 10^{18}/s for NTD and less than 10^{16}/s for D^3He protons on PTD.

The DD-n and D^3He reaction rate histories for shot 38525 are shown in Figure 2-23. Shot 38525 was a typical implosion of a 24 μm thick CH shell filled with 6 atm of D_2 and 12 atm of ^3He. Distinct shock and compression components are seen in the D^3He production history, whereas there is no evidence of neutrons at shock time in the DD-n production history.

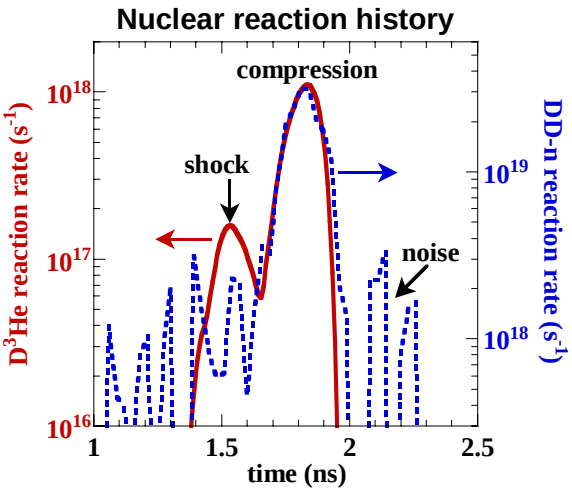

Figure 2-23: Measured D^3He proton (solid red) and DD-n (dotted blue) nuclear reaction histories of shot 38525, a 24 μm thick CH shell filled with 6 atm of D_2 and 12 atm of ^3He. The noise level in the burn histories is about 10^{18}/s for DD-n, and less than 10^{16}/s for D^3He.

For ease of comparison, data from PTD and NTD is often reduced to "bang time", the time of peak production of nuclear fusion products, and "burn duration", which is the FWHM (the full temporal width at half the maximum production rate) of the production peak. The D^3He history can sometimes be separated into distinct shock and compression peaks, each of which has its corresponding bang time and burn duration. The amplitude measured by both NTD and PTD is typically normalized to the yield measured by the nTOF or the WRF diagnostics, respectively, but yield can be directly inferred (with lower accuracy) using the NTD or PTD nuclear reaction history if the other diagnostics are not available.

2.6.4 Imaging Diagnostics

Images of the nuclear burn region can provide critical information about the complex dynamics of fuel capsule implosions. The spatial distribution of nuclear reactions is affected by such phenomena as fuel-shell mix, implosion asymmetries, and radiation and heat transport. Images of nuclear production also provide excellent tests for simulations.

The Proton Core Imaging System (PCIS) [55] is able to image nuclear protons emitted from the implosion. Both DD and D^3He protons are detectable with PCIS simultaneously. PCIS uses a circular aperture cut into a tantalum substrate, which allows protons passing through to be recorded on a CR-39 nuclear detector (Figure 2-24). Information about the size and shape of the nuclear burn region is encoded in the proton penumbra of the aperture. This information is decoded using special algorithms [56] to determine the size and shape of nuclear production.

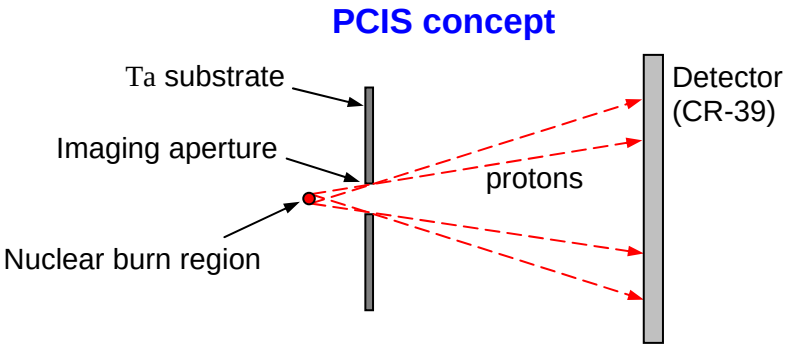

Figure 2-24: The concept of the Proton Core Imaging System (PCIS). A circular aperture cut into a tantalum (Ta) substrate allows protons through to a CR-39 detector. Information about the size and shape of the nuclear burn region is encoded in the proton penumbra of the aperture, which is captured by the CR-39.

For OMEGA implosions of CH capsules, the D^3He proton emission images are well fit by Gaussian distributions, with a typical radius between 25 and 35 μm [57]. Figure 2-25 shows the PCIS radial burn profile and the PCIS proton emission surface brightness from shot 40534.

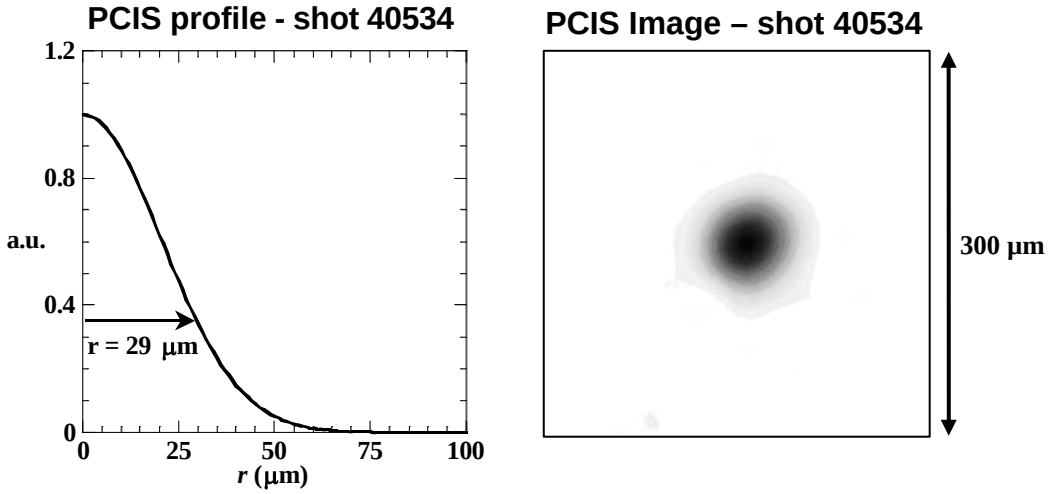

Figure 2-25: (a) D^3He radial burn profile and (b) D^3He proton emission surface brightness from shot 40534, obtained using PCIS. Shot 40534 was an 18 μm CH shell filled with 18 atm D^3He. The proton emission is very symmetric, and is well fit by a Gaussian profile with a 29 μm radius.

3 Hydrodynamic-Equivalence

Ignition and high gain in inertial confinement fusion (ICF) requires an understanding of how the choice of materials affects implosion dynamics. ICF ignition targets are typically spherical capsules with an outer shell made of plastic or beryllium, a cryogenic layer of deuterium-tritium (DT) ice, and gaseous DT at the center.

Surrogate materials or configurations provide a convenient test bed to study different aspects of ignition designs [28]. These surrogates are chosen to best mimic the implosion characteristics of the original design. For example, although ignition designs use an equal-mole DT mixture, pure D_2 is commonly used as a surrogate. However, the different mass densities can cause a difference in implosion dynamics (in particular through the Atwood number, which differs by a factor of 2 at the fuel-shell interface during the deceleration phase [58]).

To explore the effects of fill composition on implosion dynamics of surrogate fuels, a series of experiments using different ratios of D_2 and ^{3}He was performed. Evaluation of surrogate materials is best done when the materials are chosen to be as nearly hydrodynamically-equivalent as possible. D and ^{3}He have the special property that they have the same value of $(1+Z)/A$, allowing mixtures of D_2 and ^{3}He to be chosen such that the mass density and the total particle density upon full ionization are identical. This results in the same Atwood number (affecting hydrodynamic instabilities) and the same equation of state (EOS).

An additional advantage of these surrogate targets is that products from the DD nuclear reaction can be measured for all mixtures, whereas measuring the DD products from a DT implosion has proven difficult for ignition relevant implosions due to the large background of DT neutrons. A final advantage of D_2 and ^{3}He mixtures is their emission of D^{3}He protons that have been extensively used to diagnose ICF implosions at OMEGA [42][54][56].

This chapter reports the results published in reference [59]. Section 3.1 is a description of the setup and diagnostics used in the experiments. Section 3.2 describes the yield scaling expected of hydrodynamically-equivalent implosions. Section 3.3 describes the results observed in the experiments, as well as comparisons to the expected scaling and to 1-D rad-hydro simulations. Section 3.4 discusses possible explanations, and a summary is given in Section 3.5.

3.1 Experimental setup

Direct-drive implosions were conducted at OMEGA [30], with 60 beams of frequency-tripled (351 nm) UV light in a 1-ns square pulse and a total energy of 23 kJ. Distributed phase plates [36], and 2-D, 1-THz bandwidth smoothing by spectral dispersion of the laser beam were used [37]; the beam-to-beam energy imbalance was typically between 2 and 4% rms. The spherical targets were CH-shelled capsules with diameters between 860 and 880 μm, wall thickness of 15, 20, 24 or 27 μm, and a flash coating of about 0.1 μm of Aluminum.

The gaseous fill of the capsules was composed of mixtures of D_2 and ^{3}He such that the atomic composition varied from pure D to nearly pure ^{3}He. Two classes of fill pressure were used, low (equivalent to 3 atm D_2) and high (equivalent to 15 atm D_2), with predicted convergence ratios of 37 and 14, respectively. The mixtures within each class are considered hydrodynamically equivalent in that they have the same mass density (and therefore the same

Atwood number during the deceleration phase), and, upon full ionization (above a few eV), the same total particle density, and EOS (ideal monatomic).

Capsule fills are hydrodynamically-equivalent if the fill pressures of D_2 (X atm) and ^{3}He (W atm) are chosen to obey:

$$X + \frac{3}{4}W = X_0, \tag{3-1}$$

where X_0 is the hydrodynamically-equivalent pure D_2 fill pressure, in this paper equal to either 3 atm or 15 atm. The deuterium ion fraction by atom f_D scales with X and X_0 as:

$$f_D = \frac{3X}{X + 2X_0}. \tag{3-2}$$

Since there are only two components to the fill gas, $f_{3He} = 1\text{-}f_D$.

Two standard gas mixtures were used to fill targets of all types: pure D_2 ($f_D = 1.0$), and a D_2-^{3}He mixture with a 1:1 atomic ratio ($f_D = 0.5$). A series of shots with different mixtures of D_2 and ^{3}He was undertaken for the 20 and 24 μm thick, high pressure capsules. In addition to the premixed, $f_D = 1.0$ and 0.5 compositions, compositions with $f_D = 0.07$, 0.27, and 0.78 were used[17].

The error in the fill composition for the "standard" ($f_D = 0.5$) D_2-^{3}He mixture is about 1% of f_D, since it comes premixed. Fill composition errors for the other composition ratios, which must be mixed to order, are also small – less than 3% [60] of f_D. This error estimate includes uncertainties in the original fill pressure, as well as uncertainties in the leak rates of D_2 and ^{3}He through the storage cell, and through the target shell as it is handled before shot time. The total fill pressure is known to better than 10%, and is independent of the fill composition [60].

The following primary nuclear reactions occur in implosions of targets filled with mixtures of D_2 and ^{3}He:

$$\begin{aligned} \mathrm{D + D} &\rightarrow {}^3\mathrm{He + n\ (2.45\ MeV)}, \\ \mathrm{D + D} &\rightarrow \mathrm{T + p\ (\ 3.0\ MeV)}, \\ \mathrm{D + {}^3He} &\rightarrow {}^4\mathrm{He + p\ (14.7\ MeV)}, \end{aligned} \tag{3-3}$$

where the number in parentheses is the mean birth energy of the second product. Figure 3-1 shows the temperature dependence of the thermal reactivities of the D^{3}He reaction and the n-branch of the DD reaction, as determined by Bosch and Hale [23]. The branching probability of the n- and p- branches of the DD reaction are nearly equal over the temperatures of interest.

[17] The $f_D = 0.78$ shots plotted on the 20 μm thick CH subfigures actually had 19 μm thick CH shells.

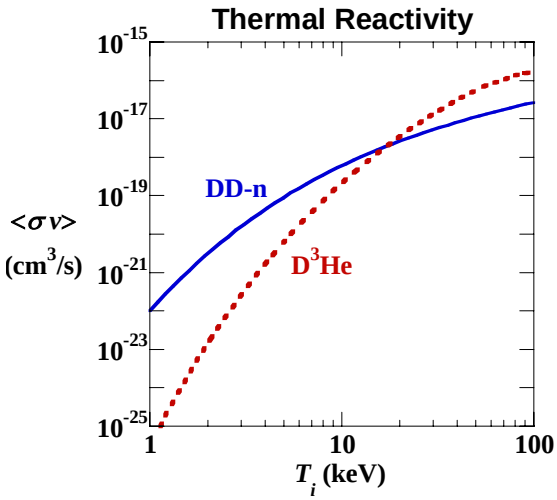

Figure 3-1: DD-n and D^3He thermal reactivities as a function of ion temperature.

The principle diagnostics for this work were neutron time-of-flight (nTOF) scintillators [46] to measure the neutron branch of the DD reaction, and multiple wedge-range-filter (WRF) proton spectrometers [42] to measure the protons from the D^3He reaction. The nTOF detectors measure neutron yield and DD-burn averaged ion temperature, determined from the Doppler broadening of the neutron signal.

The WRF spectrometers measure the D^3He proton spectrum with high resolution (~100 keV). Transient magnetic fields[18] in the implosion corona can redistribute the initially isotropic proton flux emitted by the capsule by 20% rms (typical) [42]. The average of multiple (2 to 7) spectrometers is used to obtain an estimate of the total yield. The mean downshift of the D^3He protons from their birth energy of 14.7 MeV is used to infer the areal density (ρR) of the imploded capsule averaged over the D^3He proton production. [42]

An alternative measurement of the burn-averaged ion temperature is given by the "ratio method" [61]. The ratio of primary yields can be used to infer the ion temperature using the thermal reactivities (Figure 3-1) and the fuel composition. The ratio of DD-n to D^3He reactivities changes by more than three decades from 1 keV to 10 keV, giving a determination of temperature that is not highly sensitive to the exact yields. Differences in burn duration or burn volume of the two constituent reactions result in only minor corrections to the inferred temperature (for example, see the very similar burn histories for DD-n and D^3He compression in Figure 3-2). This correction is small mainly because both reactions are dominated by the high-temperature region near the center.

Temporal diagnostics of the nuclear products include the Neutron Temporal Diagnostic (NTD) [52] for measuring the DD-n burn history, and the Proton Temporal Diagnostic (PTD) for measuring the D^3He burn history [53][54]. The D^3He burn history typically exhibits two periods of proton emission [62] – the first is the "shock burn", which occurs after the first convergence of the shock, near the end of the coasting phase, and before the capsule has fully compressed. About 300 ps later is the "compression burn" (see Figure 3-2) which occurs during the deceleration and stagnation phases. Spectral measurements of the emitted D^3He protons from

[18] Tangential electric fields have not been excluded as the cause for the anisotropic proton emission, but for these implosions there is no radial E field when the protons are emitted.

such capsules can often be decomposed into such "shock" and "compression" components, due to the different areal densities they pass through while escaping the capsule (~10 mg/cm^2 at shock and ~60 mg/cm^2 during compression). Due to the much weaker temperature dependence of the DD-n reactivity, the contribution of the high-temperature, low-density shock burn phase to the total yield is much lower than for D^{3}He (typically 0.5-1% rather than 5-20%).

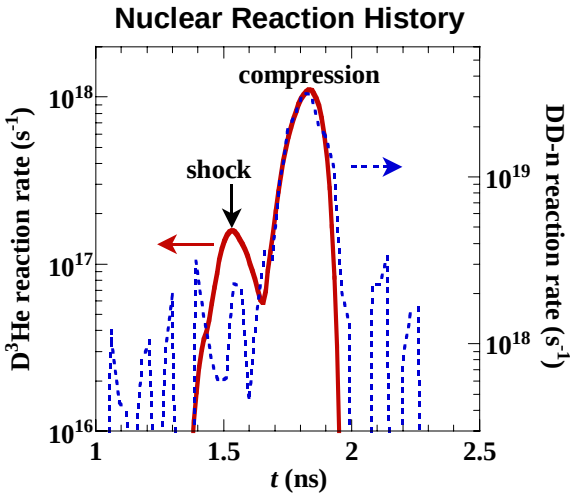

Figure 3-2: Measured D^{3}He proton (solid red) and DD-n (dashed blue) nuclear production histories of a 24 μm thick CH shell filled with 6 atm of D_2 and 12 atm of ^{3}He (shot 38525). Distinct shock and compression components are seen in the D^{3}He production history, whereas there is no evidence of neutrons at shock time in the DD-n production history. The noise level in the burn histories is about 10^{18}/s for DD-n, and less than 10^{16}/s for D^{3}He.

1-D rad-hydro simulations of these implosions were done using the code LILAC [31] using the new input deck, and with a flux limiter of 0.06. Composition scaling simulations were run by changing the initial fill composition, while using the same target and laser conditions. In order to obtain yields of both reactions using compositions of $f_D = 0.0$ and 1.0, the results of those simulations were post-processed as having a trace of the minority species.

3.2 Expected scaling

The nuclear yield is the spatial and temporal integral of the product of reactant densities times the temperature-dependent thermal reactivity of the nuclear reaction under consideration:

$$Y_n = \int \frac{1}{2} {n_D}^2(\vec{r},t) < \sigma v >_{DD-n} d^3\vec{r}dt,$$
$$Y_p = \int n_D(\vec{r},t) n_{3He}(\vec{r},t) < \sigma v >_{D3He} d^3\vec{r}dt, \quad (3\text{-}4)$$

where Y_n and Y_p are the DD neutron and D^{3}He proton yields, n_D and n_{3He} are the number densities of D and ^{3}He, and $<\sigma v>$ is the local thermal reactivity averaged over a Maxwellian ion velocity distribution with temperature T_i. The particle densities and ion temperature will in general be functions of position and time. The factor of 1/2 for Y_n accounts for the double-counting of identical reactants.

For the hydrodynamically-equivalent mixtures of D_2 and ^{3}He considered here, and using the relation $n_i = \rho/A\ m_p = \rho/(3 - f_D)m_p$, the yields can be re-expressed in terms of f_D:

$$Y_n = \frac{f_D{}^2}{(3-f_D)^2}\int \frac{\rho^2(\vec{r},t)}{2m_p{}^2} < \sigma v >_{DD-n} d^3\vec{r}dt,$$
$$Y_p = \frac{f_D(1-f_D)}{(3-f_D)^2}\int \frac{\rho^2(\vec{r},t)}{m_p{}^2} < \sigma v >_{D3He} d^3\vec{r}dt, \quad (3\text{-}5)$$

where m_p is the proton mass and ρ is the mass density. The factor $(3 - f_D)^2$ is equal to A^2, and adjusts for the slightly different ion number densities of D_2 and ^{3}He plasmas at equal mass density. The advantage of this form is that the dependence on the fill composition, that determines the difference between hydro-equivalent targets, is taken out of the integral.

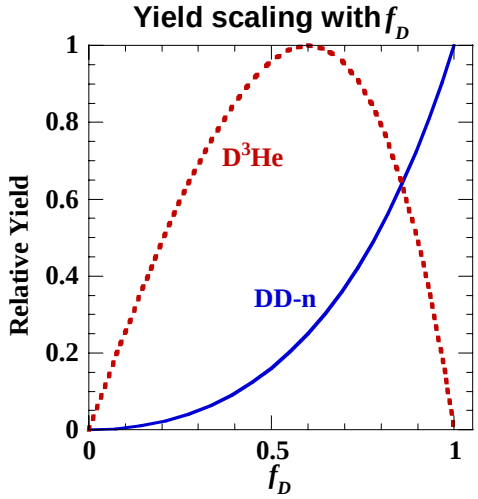

Figure 3-3: Yield dependence of the DD-n and D^{3}He reactions on the D fraction by atom (f_D).

Figure 3-3 shows the predicted scaling of the DD neutron and D^{3}He proton yields as a function of fill composition for hydro-equivalent fuels. Although the character of the composition scaling is very different for the different nuclear reactions, both curves are independent of the implosion dynamics, so the composition contribution to the yield can be factored out.

All subsequent yields in this paper will be scaled according to Equation (3-6), unless otherwise noted:

$$\tilde{Y}_n = Y_n \frac{(3-f_D)^2}{f_D{}^2},$$
$$\tilde{Y}_p = Y_p \frac{(3-f_D)^2}{f_D(1-f_D)}, \quad (3\text{-}6)$$

where $\tilde{Y}_n$ and $\tilde{Y}_p$ denote the scaled DD-n and D^{3}He yields, respectively.

3.3 Experimental observations

The hydrodynamic equivalence of D_2 and ^3He mixtures is most clearly demonstrated by measurements of implosion timing. The time of peak neutron emission (DD-n bang time), as well as the duration of the neutron emission (characterized by the full-width at half maximum as measured by the NTD) are independent of f_D. In addition, the time of peak proton emission during the compression phase (D^3He compression bang time), and the duration of proton emission (characterized by the FWHM of the compression peak as measured by PTD) are also independent of f_D. Table 3-1 lists the experimental mean and error in the mean of DD-n and D^3He bang time and burn duration, as measured over each group of nominally identical shots.

Figure 3-4 plots the bang time and burn duration of both nuclear products as a function of f_D for 20 and 24 μm thick CH shells. Bang times and burn durations of the two nuclear products are also in good agreement with each other, an example of which can be seen fully in Figure 3-2.

Table 3-1: DD-n and D^3He bang time and burn duration for variation values of f_D for implosions of capsules with 20 and 24 μm of CH. The timing of nuclear production is independent of f_D.

Shell	f_D	Num shots	DD bang (ps)	err	DD burn (ps)	err	D^3He bang (ps)	err	D^3He burn (ps)	err
20 μm CH	1.000	22	1758	15	172	6	-		-	
"	0.778	5	1681	13	158	11	1702	15	183	15
"	0.500	8	1753	22	157	9	1736	17	155	11
"	0.273	4	1754	33	138	19	1764	15	160	15
"	0.073	3	-		-		1743	17	165	17
24 μm CH	1.000	10	1936	11	189	8	-		-	
"	0.778	2	1861	21	167	18	1860	21	156	21
"	0.500	9	1878	21	159	18	1887	17	167	11
"	0.073	3	-		-		1830	17	144	17

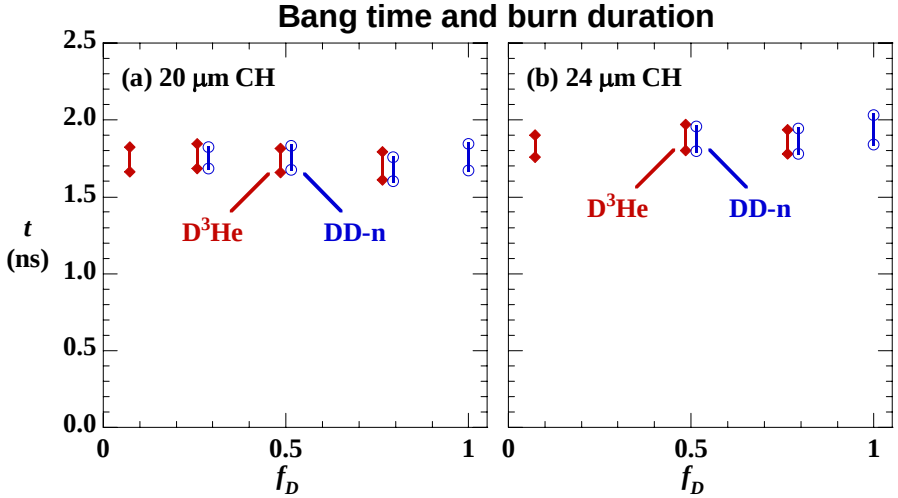

Figure 3-4: Nuclear bang time and burn duration as a function of fill composition, for implosions with (a) 20 μm and (b) 24 μm of CH. Solid diamonds and open circles are the times of half max of peak emission of the D^3He protons and DD-neutrons, respectively. Adjacent D^3He and DD-n burn lines are from the same group of shots, but have been artificially separated in f_D for clarity.

The measured yield of these hydrodynamically equivalent implosions deviates from the anticipated scaling shown in Figure 3-3. The deviation of the scaled DD-n and D^3He compression yields ($\tilde{Y}_n$ and $\tilde{Y}_{p\text{-}c}$) for 20 and 24 μm CH shells with high pressure fills is shown in Figure 3-5. The yields have been scaled to the fill composition according to Equation (3-6), and in addition have been normalized to the yield at $f_D = 0.5$, to emphasize the composition scaling for different measurements. Yields from targets with D rich and ^3He rich fuels are typically twice as high as yields from targets with $f_D = 0.5$. This trend is seen for both DD-n and D^3He yields, and for both 20 and 24 μm shells[19].

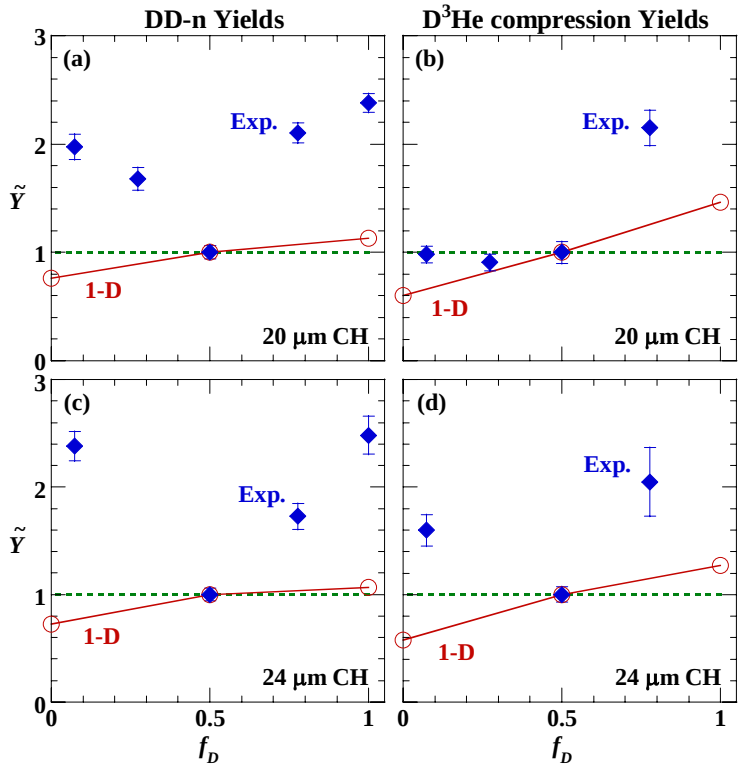

Figure 3-5: Scaled DD-n and D^3He compression yields for high pressure ($X_0 = 15$ atm) fills of shells with 20 and 24 μm of CH. (a) $\tilde{Y}_n$, 20 μm; (b) $\tilde{Y}_{p\text{-}c}$, 20 μm; (c) $\tilde{Y}_n$, 24 μm; (d) $\tilde{Y}_{p\text{-}c}$, 24 μm. All yields have been scaled to fill composition according to Equation (3-6), and normalized to the yields at $f_D = 0.5$. True hydro-equivalent implosions would scale to the same yield (dotted line). 1-D simulations with LILAC (open circles, solid line) deviate slightly from hydro-equivalence, but not nearly as much as experimental measurements (blue diamonds). Diamonds are the mean yield and standard error in the mean of measurements from a group of nominally identical capsules. The 20 μm plots show data reduced from a total of 42 shots, and the 24 μm plots show data reduced from a total of 24 shots.

This observed deviation is not seen in 1-D simulations (dashed line in Figure 3-5), which instead more nearly follow the hydro-equivalent scaling, with only minor deviations. Table 3-2 shows the absolute yields of the normalization points at $f_D = 0.5$, as observed experimentally and as calculated by LILAC, as well as the absolute DD-n yield at $f_D = 1.0$. The DD-n experimental yield over calculated yield (YOC) is 21% for $f_D = 0.5$, and 43% or 48% for $f_D = 1.0$.

Comparison of the YOC for DD-n and D^3He on shots with $f_D = 0.5$ illustrates the utility of simultaneous measurement of two nuclear reactions. As shown in Table 3-2, the D^3He

[19] Except for the D^3He yield from the ^3He rich, 20 μm thick target implosions.

compression YOC is about 35%, compared to the DD-n YOC of 21%. The difference in the YOCs for the two nuclear reactions is due to their probing the deviation between the simulated and actual implosion in different ways as a result of their different temperature sensitivities.

Table 3-2: Absolute (unscaled) compression yields of DD-n for $f_D = 1.0$ and 0.5 shots, and D^3He for $f_D = 0.5$ shots, as observed experimentally and as calculated by LILAC. The experimental yield over calculated yield (YOC) is also shown.

		$f_D = 1.0$	$f_D = 0.5$	
Shell	Type	Y_n ($\times 10^{10}$)	Y_n ($\times 10^{10}$)	$Y_{p\text{-}c}$ ($\times 10^{8}$)
20 μm CH	observed	19.2	1.29	6.10
"	calculated	44.6	6.29	18.4
"	YOC	43.1%	20.5%	33.2%
24 μm CH	observed	9.0	0.58	1.53
"	calculated	18.7	2.80	4.22
"	YOC	48.1%	20.7%	36.2%

The "factor of two" deviation of the yield scaling seen in these 20 and 24 μm CH shell, high pressure composition campaigns has also been seen over a diverse set of target configurations. Targets with 15, 20, 24, and 27 μm thick CH shells, and with both high and low fill pressure, were filled with the two standard compositions, $f_D = 1.0$ and 0.5. Implosions of targets with both composition types emit DD-neutrons, and so a comparison of $\tilde{Y}_n$ for like implosions with different compositions was done. Figure 3-6 shows the ratio of scaled yields, $\tilde{Y}_n[f_D = 1.0]/\tilde{Y}_n[f_D = 0.5]$ for these implosions. The points at 15 atm, and at 20 and 24 μm are the same as the points at $f_D = 1.0$ in subfigures (a) and (c) of Figure 3-5. Data reduced from 118 shots predominantly gives a ratio greater than two, where a ratio of one is anticipated for all capsule types.

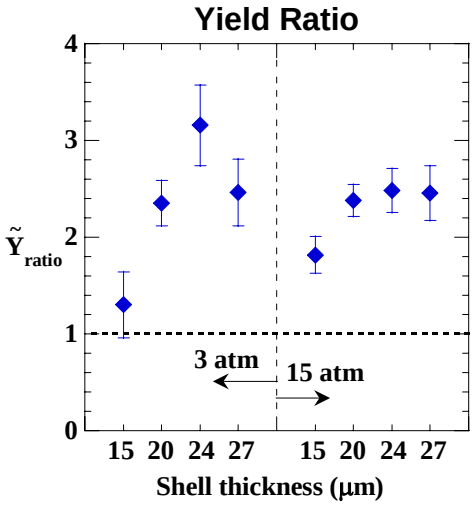

Figure 3-6: The ratio of measured $\tilde{Y}_n$ for $f_D = 1.0$ shots over $\tilde{Y}_n$ for $f_D = 0.5$ shots. The ratio anticipated by the scaling in Equation (3-6) is one (horizontal dotted line) for all target parameters. The points are the ratio of scaled average yields, and the errors are the quadrature sum of the standard errors of the yields from groups of targets with the two fill compositions. This plot shows data reduced from 118 shots.

The observed ion temperatures are not sufficient to explain the observed yield deviation. The mean ion temperature was measured using two methods – nTOF Doppler broadening and the yield ratio method. The nTOF does not show a trend in the ion temperature, whereas ion the ratio method suggests increasing temperatures for higher D content fuels (see Figure 3-7). 1-D LILAC simulations give burn-averaged temperatures that are not strongly dependent on fill composition. Areal density measurements using the downshift of primary D^3He protons (D^3He fuels) or secondary D^3He protons (pure D_2 fuel) show a lower value at compression time for $f_D = 0.5$ (for 24 μm shells) (Figure 3-8), suggesting slightly less compression for those shots.

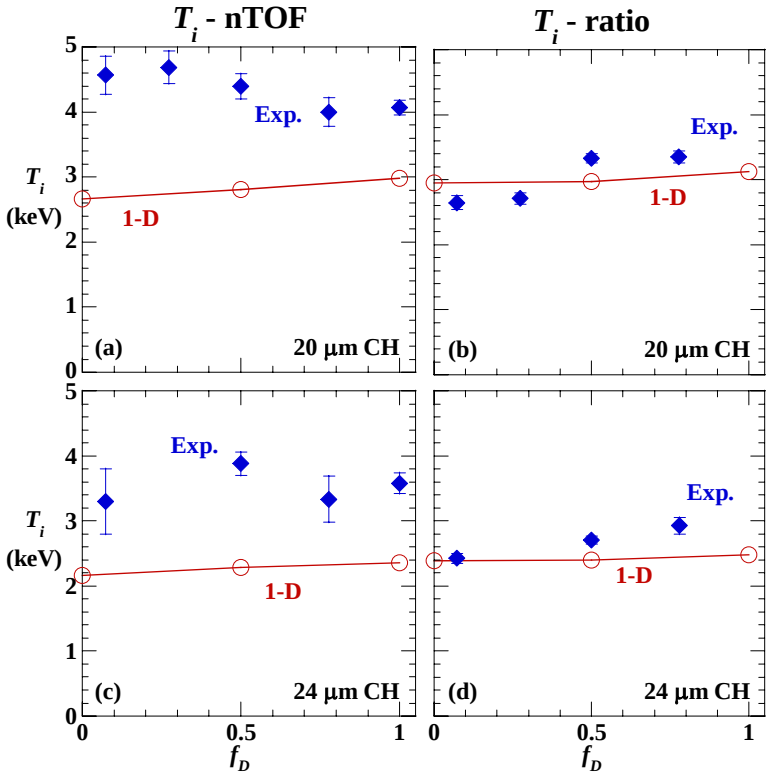

Figure 3-7: Ion temperature as a function of fill composition, as determined by nTOF for high pressure fills of (a) 20 μm and (c) 24 μm shells, and using the ratio method for (b) 20 μm and (d) 24 μm. Solid diamonds: mean and error of the mean of experimental observations. Open circles: 1-D simulations.

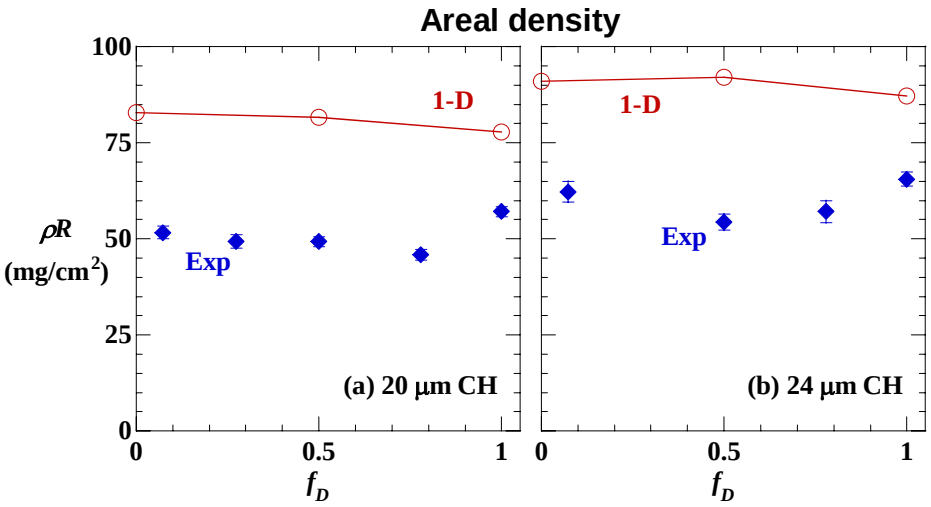

Figure 3-8: Inferred compression-burn-averaged ρR as a function of fill composition, for high pressure fills of 20 μm (a) and 24 μm (b) thick shells. Solid diamonds: mean and error of experimental observations. Open circles: 1-D simulations. For each plot, higher ρR corresponds to more compression, since all targets started with the same shell thickness.

A similar deviation from the anticipated scaling is also seen for the D^3He shock yield ($\tilde{Y}_{p\text{-}s}$), which is emitted about 300 ps earlier than the compression yield, and is produced under very different conditions, before the start of the deceleration phase and the onset of turbulent mixing (see Chapter 4), at temperatures twice as high as that at compression time, and at mass densities less than 10% those at compression time. Figure 3-9 shows the scaled D^3He shock yield and the shock-yield-averaged ρR for implosions with 24 μm CH shells. The results at shock time are reminiscent of the results at compression time, with lower scaled yield and ρR for the $f_D = 0.5$ shots than for D-rich or ^3He-rich mixtures.

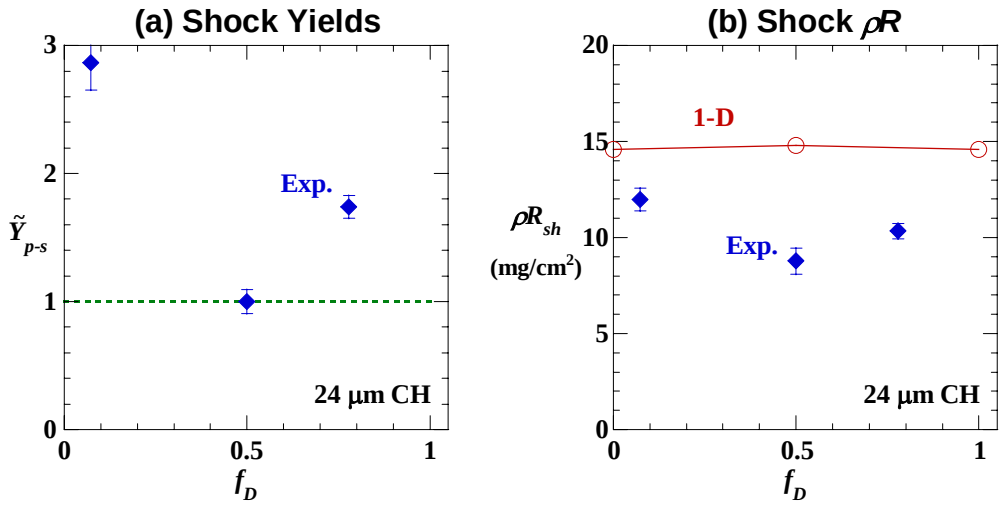

Figure 3-9: D^3He shock results for 24 μm CH capsules. (a) Scaled shock yield and (b) shock-yield-averaged ρR as a function of fill composition. Dotted line: hydro-equivalent scaling. Open circles and solid line: 1-D simulations. Solid diamonds: average and standard error of experimental observations.

A summary of yield, temperature, and compression results presented in this section is listed in Table 3-3 for different mixtures of high pressure fills in shells with 20 and 24 μm of CH.

Table 3-3: D fraction by atom, number of shots averaged, DD-n, D^3He compression and shock yields (scaled by fill composition and normalized to $f_D = 0.5$), ion temperature, and areal density, for high pressure fills of two different shell thicknesses.

Shell	f_D	Num shots	$\lvert\tilde{Y}_n\rvert$	err	$\lvert\tilde{Y}_{p\text{-}c}\rvert$	err	$\lvert\tilde{Y}_{p\text{-}s}\rvert$	err	T_{ntof} (keV)	err	T_{rat} (keV)	err	ρR (mg/cm^2)	err
20 μm	1.00	22	2.38	0.09	-		-		4.1	0.1	-		57.1	1.3
"	0.78	5	2.10	0.09	2.15	0.16	1.51	0.16	4.0	0.2	3.3	0.1	45.8	1.4
"	0.50	8	1.00	0.06	1.00	0.10	0.95	0.10	4.4	0.2	3.3	0.1	49.3	1.3
"	0.27	4	1.68	0.11	0.91	0.08	0.71	0.08	4.7	0.3	2.7	0.1	49.3	1.7
"	0.07	3	1.97	0.11	0.98	0.08	1.08	0.06	4.6	0.3	2.6	0.1	51.6	1.7
24 μm	1.00	10	2.48	0.18	-		-		3.6	0.2	-		65.5	1.9
"	0.78	2	1.73	0.12	2.05	0.32	1.74	0.09	3.3	0.4	2.9	0.1	57.1	2.9
"	0.50	9	1.00	0.06	1.00	0.07	1.00	0.09	3.9	0.2	2.7	0.1	54.4	2.1
"	0.07	3	2.38	0.14	1.60	0.15	2.87	0.21	3.3	0.5	2.4	0.1	62.2	2.7

3.4 Discussion

A closer look at the possibility of a measurement error is certainly warranted when observations deviate so far from the scaling derived from simple principles, as well as from computer simulations. The individual measurement error on a given shot is about 10% for both DD-n and D^3He yields; however, the shot-to-shot yield variation for nominally identical shots is closer to 20% rms. Averaging the results from many like shots reduces the standard deviation of the mean considerably, in most cases below 10%. Systematic yield uncertainties in the diagnostics are unlikely to cause the yield scaling. The yield measurements for the two nuclear reactions use different diagnostics, using different principles, yet measured the same deviation.

From Equation (3-4), the deviation in the yield scaling must then be explained through differences in composition, temperature, density, burn volume, or burn duration of the target during the implosion. According to temporal measurements of nuclear burn histories, the implosion timing does not depend on the fill composition. Uncertainty in the composition is at most a couple of percent, which is not enough to affect the yields by a factor of 2. In addition, composition errors affect the DD-n and D^3He yield scaling in different ways (Figure 3-3), yet the same deviation is seen for both.

The observed trend of the ratio-inferred ion temperature could be part of the story, due to the strong dependence of the thermal reactivities of both reactions at the temperatures of interest. The DD-n and D^3He reactivities scale approximately as T_i^4 and T_i^7 near $T_i = 3$ keV. A linear fit through the observed ratio-inferred T_i in Figure 3-7d was used to adjust the hydro-equivalent $\tilde{Y}_n$ scaling. The solid curve in Figure 3-10a plots this T_i-ratio yield scaling against the observed yields from Figure 3-5c. This corrected scaling looks better for D-rich fuels, but deviates further than the uncorrected hydro-equivalent scaling from the observed yields for ^3He-rich fuels. Since there was no clear trend in the nTOF-derived temperatures, a similar yield scaling fit was not done using the nTOF temperatures.

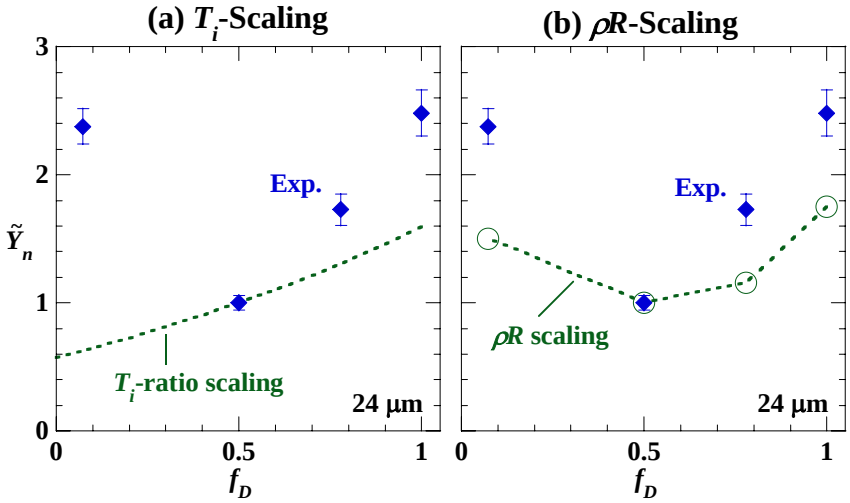

Figure 3-10: Measured (solid diamonds) DD-n yields as a function of f_D for 24 µm shells with high pressure, from Figure 3-5c. In these plots, the hydro-equivalent scaling has been adjusted to take into account effects of measured ion temperature and areal density on the yield. (a) The dotted line is a T_i-corrected scaling curve, based on a linear fit to the experimental T_i-ratios in Figure 3-7d. (b) The open circles and connecting line include a ρR correction based on the measured ρR values shown in Figure 3-8b.

The two remaining factors of fuel density and burn volume are related to the compression of the capsule, which can be inferred by measurements of ρR. A simple model of the implosion, that assumes that the shell temperature and shell aspect ratio at bang time does not depend on fill composition, determines that the yield scales approximately as $(\rho R)^3$. The open circles in Figure 3-10b plots this ρR yield scaling against the observed yields from Figure 3-5c. Higher ρR's were observed for high and low D concentrations compared to the 50/50 mixture. The shape predicted from the $(\rho R)^3$-scaling is in qualitative agreement with the measurements, though it does not show quite as strong a scaling.

Although additional measurements suggest that some combination of ion temperature and density might be sufficient to explain the observed yield deviation, these factors must come from some physical mechanism, a number of which will be explored below.

The deviation from the assumed hydro-equivalence is unlikely to be explained by 2-D or 3-D hydro effects, including hydrodynamic instabilities and turbulent mixing that would reduce the burn volume and truncate the burn duration. A similar trend was experimentally observed over a wide range of physical situations in which 2-D hydro effects would likely have behaved very differently. Implosions with thicker shells are considered to be more hydrodynamically stable [63], yet the same yield trend is seen for 20 and 24 µm shells with high fill pressure. Implosions with low fill pressure are considered less hydrodynamically stable, yet the yield trend is the same as for high fill pressure (Figure 3-6). A similar trend is also seen for D^3He shock burn measurements, despite the fact that there is no atomic level mixing in the burn region at shock time (see Chapter 4). Thus, pure hydrodynamics can not explain the observed differences.

A wealth of data seems to exclude pure hydrodynamic differences between these mixtures as the mechanism for the observed variation in their yields (as it should be since they were chosen to be hydro-equivalent). The deviation from hydrodynamic equivalence is likely to be due to the microscopic details of the mixture. It may have something to do with the variation in the average

Z in the fuel, which varies from 1 (pure D_2), to nearly 2 (^{3}He rich), the difference in ion masses, or a subtlety in the statistical treatment of mixtures.

Bremsstrahlung radiation scales as $\sim \rho^2 T_e^{1/2} Z^3/A^2$, which for these mixtures differs by a factor of 3.6 from pure D_2 (low) to pure ^{3}He, assuming the same density and temperature. A factor of 3 difference in the radiated power may then trigger differences in the absorption in the CH, and initiate changes in the implosion dynamics. However, the yield discrepancy trend is about the same for cases with significantly different radiative properties, such as for low pressure and high pressure fills, as well as at both shock and compression time. The difference in density in these scenarios radically affects the efficiency of Bremsstrahlung radiation. In addition, the yield deviation is not monotonic with D fraction, so Bremsstrahlung radiation seems unlikely as the sole mechanism.

Thermal conduction in these dynamic implosions can be difficult to calculate due to steep gradients, complex magnetic field geometries, non-equilibrium conditions, and other non-local effects. However, to get a sense of the scaling, consider Spitzer-Harm electron thermal conduction [64]:

$$\begin{aligned} q_{SH} &= -K\nabla T, \\ K &\propto \delta(Z)\frac{T_e^{5/2}}{Zm_e^{1/2}\ln\Lambda}, \\ \delta(z) &= \frac{Z+0.24}{Z+4.2}. \end{aligned} \tag{3-7}$$

Ignoring the coulomb logarithm variation, pure D_2 has a 32% higher classical conductivity than pure ^{3}He, and 17% higher than the standard D_2-^{3}He mixture (using "average" ions). Ion thermal conduction has a similar form, but with a much stronger Z dependence [65]. Ion conduction is relatively small when the ion and electron temperatures are equal, but can become important when the ion temperature is higher, such as for shock heating. But for both types of thermal conduction, the trend is again monotonic with D fraction.

Shock heating initially puts most energy into heating the ions, with more energy going to heavier ions [21]. Equal-density mixtures of D_2 and ^{3}He will absorb the same total amount of energy from a shock front, but mixtures with a higher concentration of ^{3}He will have a higher initial ion temperature due to the higher average ion mass (and corresponding lower ion density). A slight difference in this initial state of the gas might, after compression, be enough to change the dynamics and the resulting nuclear yields. However, the compression condition will be quite a bit different for the different implosions types (high, low pressure; thin, thick shells), yet the same deviation is seen in many cases. It is also difficult to explain the non-monotonic trend with this picture.

It is possible that there is stratification of the ion species during the deceleration phase. The scaled performance of the "pure" fuels seems to be greatest, so perhaps the mixture of different species is important. During the deceleration phase, the ^{3}He concentration might be slightly enhanced near the center. The hot center will then have a lower nuclear yield due to scarcer D ions. In this picture, though, the ^{3}He rich fuels should also have a reduced yield, so the non-monotonic trend is again a problem.

The plausibility of stratification can be considered using simple arguments. Because of the high density during the compression phase, any concentration enhancement will have to come through a difference in diffusion of the D and ^{3}He ions. With plasma parameters typical of the fill early in the compression burn (4 keV, 3 g/cc), it is found that the time it takes even one particle to diffuse across the capsule is very much longer than the implosion time.

Kinetic effects could play an important role in the observed yield scaling. A non-Maxwellian velocity distribution could significantly alter nuclear production, particularly at the time of shock collapse, where the distribution is far from Maxwellian. It has also been suggested that yield degradation could result from the loss of ions in the tail of the distribution, which normally dominate the nuclear production. The longer mean-free-paths of the ions in the tail may allow them to escape the fuel region if the $\rho R < 10$ mg/cm^2 [66]. It is not sufficient, though, that kinetic effects only change the nuclear production; a kinetic effect must change the nuclear production non-monotonically with D fraction, and by a factor of two between pure and mixed D and ^{3}He.

Many processes to explain the observed yield scaling have been considered here, but no single mechanism is sufficient to explain the trend.

3.5 Hydro-Equivalence Summary

In summary, experimental observations of the scaling of nuclear yields from implosions with hydro-equivalent mixtures of D_2 and ^{3}He deviate from the scaling determined using a simple consideration of composition ratios, as well as from a scaling based on 1-D rad-hydro simulations. This deviation is particularly puzzling since the trend is not monotonic with D fraction – the scaled D^{3}He yield is lower than the scaled yields on both the D_2 rich and ^{3}He rich sides.

The same scaling deviation is observed in diverse physical situations, including implosions of targets with initial fill pressures of 3 and 15 atm, and target shell thicknesses of 15, 20, 24, and 27 μm of CH. A similar yield scaling deviation is observed for both DD-n and D^{3}He yields, despite drastically different dependence of their yields on composition and temperature. Overall, a similar scaling deviation is seen for both the shock and compression components of the D^{3}He yield, corresponding to times separated by several hundred picoseconds, and reflecting very different plasma conditions.

It has been shown that measurements of the burn-averaged ion temperature, using two different methods, are insufficient to explain the entire yield scaling deviation. Errors in the initial fill composition of the D_2 and ^{3}He mixtures, and differences in the implosion timing have also been excluded. Measurements of the burn-averaged areal density, ρR, are suggestive that D_2 and ^{3}He mixtures with f_D near 0.5 might experience less compression, resulting in a lower yield.

A number of possible mechanisms to cause the scaling are considered, but no dominant mechanism has been identified. Differences in the radiative and transport properties of different D_2 and ^{3}He mixtures are included in 1-D simulations, but do not apparently have as great an effect on the yield as what was observed. Hydrodynamic instabilities in 2- and 3-D appear to be ruled out. The initial gas state set by the converging shock, ion species stratification, and kinetic effects were also considered.

This study raises some concern as to the near equivalence of D_2 as a DT fuel surrogate for studying implosion dynamics. Even when the mass density of the D_2 and ^{3}He mixtures is the same, we see discrepancies in the yield, although it is not clear what mechanism causes the discrepancy, and whether it is due to a difference in average *Z*, in ion masses, or in transport properties of mixed materials. To explore such issues, further scrutiny of the ion conductivity and its effects on implosion dynamics is underway, which may be an important factor due to its strong *Z* dependence.

Investigation of the yield scaling at constant *Z* could be accomplished by using different fuel mixtures, including mixtures of D and T, and an extension of this study with mixtures of D_2, ^{3}He, and either H_2 or ^{4}He. Experiments are being actively planned that would vary the D and T mixture with the aim of measuring simultaneously the absolute yield of both DT and DD[20], the results of which will have direct relevance for the fills of ignition targets, and will take us a step closer to understanding the present conundrum.

[20] Only recent technological advances have made the detection of DD neutrons in the background of DT neutrons feasible. See V. Yu Glebov *et al*, "Development of Nuclear Diagnostics for the National Ignition Facility", High Temperature Plasma Diagnostics Conference, May 2006 (invited), to be published in Rev. Sci. Instrum.

4 Mix Dynamics

Turbulent mix [67] is a vital concern in inertial confinement fusion (ICF), as it can quench the nuclear burn in the hot-spot prematurely, or even extinguish it entirely. The saturation of Rayleigh-Taylor (RT) instability growth at a density interface leads to small-scale, turbulent eddies, which in turn leads to the mixing of the high and low density material. These mixing processes can disrupt the formation of the low density hot-spot, by lowering its temperature and reducing its volume, and the resulting lower nuclear production can fail to ignite the capsule. Understanding the timing and extent of mix under different conditions is a crucial step toward mitigating the adverse effects of mix.

A substantial and sustained effort to understand hydrodynamic instabilities and mix has been ongoing for many decades, due in large part to their heavy impact on ICF. Good reviews of the literature on experimental, computational, and theoretical work on hydrodynamic stabilities and mix can be found on the first page of References [35] and [68]. Other work on mix in ICF implosions includes papers by Li [69], Radha [70], Regan [71], Wilson [72], as well as many others.

Although it has been previously demonstrated that there is no mix in the burn region at shock bang time [62], it was unknown how long after shock collapse it takes for atomic mixing to occur. This chapter presents the first time-dependent nuclear burn measurements of the mix region in ICF implosions. A brief review of the causes and effects of mix can be found in Section 4.1. The experimental setup is described in Section 4.2. Experimental observations are shown in Section 4.3. Section 4.4 demonstrates a method for constraining the amount of fuel-shell mix between shock collapse and deceleration phase onset. Section 4.5 summarizes the results.

4.1 Causes and effects of mix

When a fluid of density ρ_1 accelerates a heavier fluid of density ρ_2, the fluid interface is RT unstable (see Subsection 2.4.1). The rapid growth of initial perturbations sends spikes of the heavy fluid into the light fluid, while bubbles of the light fluid push back into the heavy fluid. The exponential growth eventually saturates into a nonlinear regime where the spike and bubble amplitudes grow quadratically in time according to [35]:

$$h(t) = \alpha A_t g t^2, \tag{4-1}$$

where g is the acceleration, $A_t = (\rho_2-\rho_1)/(\rho_2+\rho_1)$ is the Atwood number, and α is a constant that is near 0.05 for bubbles, and for spikes varies between 0.05 (same rate as bubbles) and 0.5 (free fall) as A_t varies between 0 and 1.

As the spikes and bubbles continue to interpenetrate, velocity shear between the two fluids results in further instability (the drag-driven Kelvin-Helmholtz instability) which causes the spike tips to “mushroom” and roll up on increasingly finer scales, increasing the vorticity of the flow and eventually leading to mixing of the two fluids on the atomic scale.

Regions where the turbulent mixing process has reached the atomic scale will be referred to as “atomically” mixed, to distinguish them from regions of “chunk” mix, where there are still distinct volumes of the nearly pure, original fluids (e.g. bubbles and spikes during the early

stages). Turbulent mixing processes result in a combination of both “atomic” and “chunk” mixing, with chunk mix dominating at early times, and atomic mix taking over at later times.

In ICF, both the acceleration and deceleration phases have RT unstable surfaces. The low density ablating mass pushes against the high density “payload” during the acceleration phase, and after further convergence and compression, the high density shell is stopped by the low density hot-spot during the deceleration phase. Initial perturbations are seeded by laser and target surface nonuniformities, and growth of these perturbations during the acceleration phase can feed through to the inner surface and contribute to seeding perturbations for the deceleration phase.

Unmitigated RT growth during the acceleration phase can eventually break through the shell, which will compromise its compressibility, and reduce the attainable areal density of the assembled target at stagnation. RT growth during the deceleration phase can send spikes of cold, dense fuel into the central hot-spot, potentially disrupting its formation. But even if the spikes don’t reach the center, their penetration and the resultant mixing of the cold, dense shell with the hot, low density hot-spot will cool the outer regions of the hot-spot, and reduce the volume participating in nuclear production. Reduction of the hot-spot temperature and volume will result in lower hot-spot yields, which, if low enough, could fail to ignite the capsule.

The impulsive acceleration of a density interface by a shock results in Richtmyer-Meshkov (RM) growth of any initial perturbations (see Subsection 2.4.2). RM growth of initial surface perturbations in the fuel-shell interface induced by shock breakout will enhance the seed amplitude for the RT instability during the deceleration phase. In addition, turbulence resulting from RM perturbation growth offers a possible mechanism to produce atomic-scale mixing of the fuel and shell before the onset of the deceleration phase.

4.2 Experimental setup

Direct-drive implosions were conducted at OMEGA [30], with 60 beams of frequency-tripled (351 nm) UV light in a 1-ns square pulse and a total energy of 23 kJ. SG4 phase plates [36], and 1 THz bandwidth smoothing by spectral dispersion of the laser beam were used [37]. The beam-to-beam energy imbalance was typically between 2 and 4% rms. The spherical capsules had diameters between 860 and 880 μm, a plastic shell thickness of 20 μm, and a flash coating of about 0.1 μm of Aluminum.

The target composition is configured in three ways (Figure 4-1). The first configuration (type I) has a shell made of plastic (CH), and a gaseous fill of D_2 and ^{3}He (with a 1:1 atomic ratio). The second configuration (type II) has a gaseous fill of pure ^{3}He, and a shell made mostly of CH, except for a 1 μm layer of deuterated plastic (CD) on the inner surface. The third configuration (type III) is like the second, except that the 1 μm CD layer is offset from the inner surface by 1 μm of CH. The composition of the ordinary plastic consists of an H to C ratio of 1.38, and the deuterated plastic has a D to C ratio of 1.56 [69].

The pure ^{3}He gases were filled to initial pressures of 4 and 20 atm at a temperature of 293 K, corresponding to initial mass densities of 0.5 and 2.5 mg/cm^3. The D_2-^{3}He gas is an equimolar mixture of D to ^{3}He by atom, and is filled to a hydrodynamically-equivalent initial pressure as the pure ^{3}He fill, as described in Section 3.1 and Reference [59]. Because fully ionized D and ^{3}He have the same value of $(1+Z)/A$, mixtures with the same mass density and A_t will also have

the same total particle density and equation of state, and can be considered hydrodynamically equivalent. For the 4 and 20 atm ^{3}He fills, the hydrodynamically-equivalent D_2-^{3}He pressures are 3.6 and 18 atm, respectively.

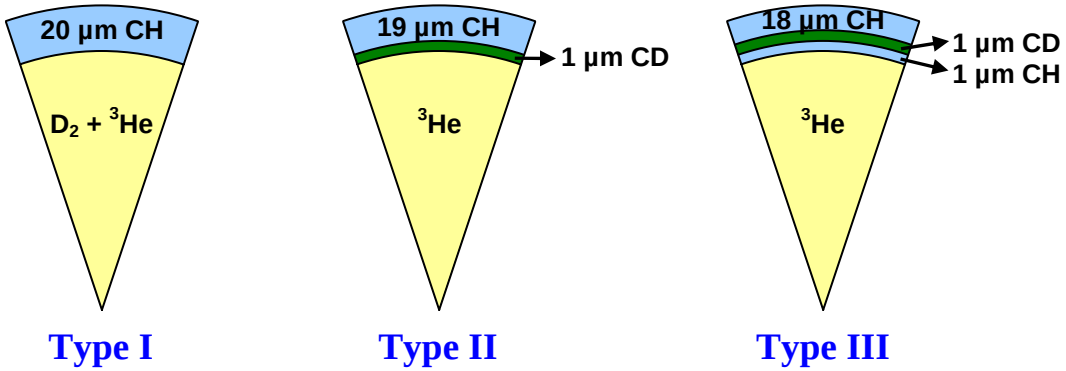

Figure 4-1: Target diagrams for the mix experiments. Pure ^{3}He gas fills a 20 μm thick plastic shell with a 1 μm deuterated layer either adjacent to the inner surface (type II) or offset from the inner surface by 1 μm (type III). The reference target (type I) contains D^{3}He gas and has no deuterated layer.

This set of capsules is ideal for studying the nature and extent of turbulent mix in ICF implosions. Whereas implosions of type I capsules will produce D^{3}He protons whenever the fuel gas gets sufficiently hot, heating alone is not sufficient for D^{3}He production in type II and III capsules. To produce measurable D^{3}He yields, these capsules require in addition the mixing of the fuel and shell on an atomic scale. Measurement or absence of the D^{3}He yield implosions of type III capsules can be used to ascertain the extent into the shell that turbulent mixing processes reach.

Fuel-shell mix is not a requirement to produce DD-n yields in type II and III implosions, but measurement of the DD-n yield provides a useful way to determine if the CD layer was heated to temperatures near 1 keV.

The primary diagnostics for this study were the Proton Temporal Diagnostic (PTD) [54], to measure the D^{3}He reaction history; multiple Wedge-Range-Filter (WRF) spectrometers [42], to measure the D^{3}He proton yield and spectrum; and the neutron Time-of-Flight (nTOF) scintillator detectors [46], to measure the DD-n yield and DD-n burn averaged ion temperature (see Section 2.6).

4.3 Nuclear observations of mix

4.3.1 Yield measurements

The existence of turbulent mixing of the fuel and shell is demonstrated by measurements of finite D^{3}He yields (Y_p) in type II capsules (see Figure 4-2 and Reference [69]). The average D^{3}He yield from implosions of type II capsules filled with 4 and 20 atm was 2.5×10^7 and 1.4×10^7, respectively. In addition, heating of the CD layer produced average DD-n yields (Y_n) in these implosions of 9.4×10^8 and 5.1×10^8.

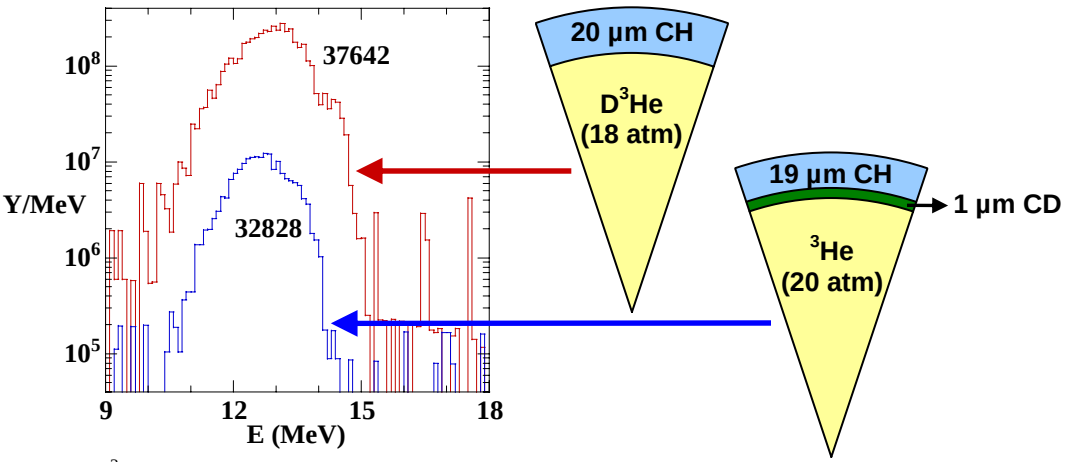

Figure 4-2: D^3He proton spectra from a type I capsule (shot 37642) and from a type II capsule (shot 32828). The high D^3He yield from type II implosions demonstrates the existence of fuel-shell mix. The type II yield, although substantially less than the type I yield, is at least two orders of magnitude higher than what would be expected in the absence of turbulent fuel-shell mix.

The D^3He yields from type II capsules are at least two orders of magnitude higher than would be expected by the interaction of thermal ^3He ions penetrating through the CD layer surface, even with enhanced surface area due to chunk mixing. For yields as high as has been observed, there must be a region which has been heated above at least 1 keV, and where the fuel and shell have experienced atomic mix.

The decreasing yields for increasing fill pressures in type II capsules contrasts strongly with the increasing yields for increasing fill pressures in type I capsules (see Figure 4-3). This is evidence that the extent of mix is reduced for increasing fill pressure, since Y_p in type II implosions is lower, even though the core conditions are more favorable for nuclear production, as seen by the higher value of Y_p for type I implosions.

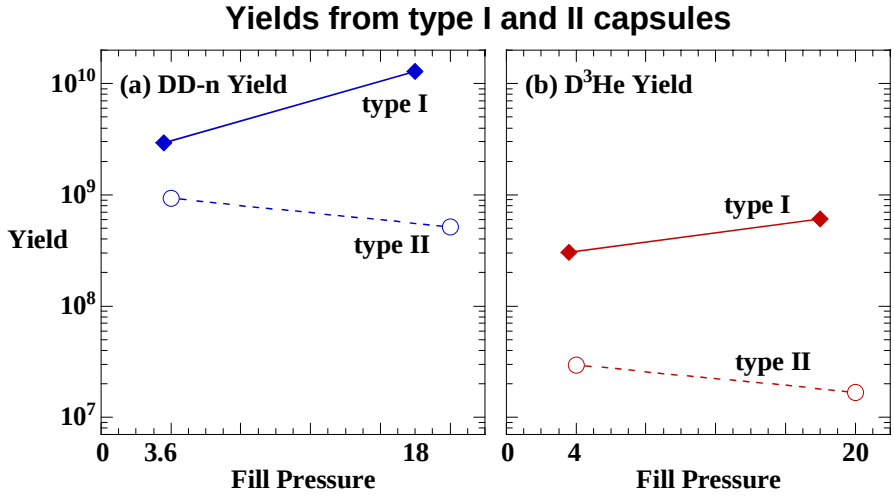

Figure 4-3: (a) DD-n and (b) D^3He yields from type I (solid diamonds) and type II (open circles) implosions as a function of capsule fill pressure. Yields from type II implosions decrease with increasing fill pressure, in contrast to the increasing yields from type I implosions. The standard error in the yield is about the same size as the markers.

The lower Y_n for type II implosions with high fill pressure indicates that less heating of the CD layer occurred in these implosions. Additional heating of the inner surface of the shell can occur through thermal conduction from and turbulent mix with the hot fuel. The lower Y_n supports the picture of reduced mix for higher pressure fills. This enhanced stability to RT-induced mixing of high pressure fills is expected based on Equation (4-1), since a lower fill pressure will result in lower fuel density and higher A_t for the same amount of compression.

Significant D^{3}He yield from type III implosions with low fill pressure (4 atm ^{3}He) demonstrates that there is substantial mixing of the fuel with the "second" μm of the shell (Figure 4-4). Thermal ^{3}He ions can not penetrate through the first μm of the shell to produce these yields, so the second μm must be exposed to the fuel by bubble growth, then mixed through turbulent processes. Comparison of the yields from type II and III capsules with low pressure fills shows that Y_n drops by a factor of 7, and Y_p by a factor of 9.

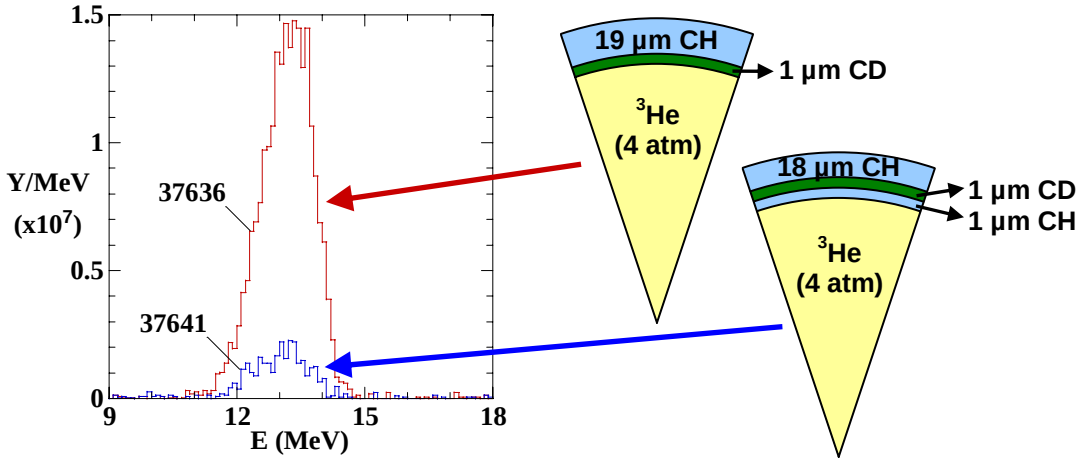

Figure 4-4: The D^{3}He yield drops by a factor of about 9 when the 1 μm CD layer is offset from the inner surface by 1 μm. The DD-n yield drops by a factor of about 7. This demonstrates that some of the second micron of the shell also gets mixed with the fuel.

The experimental results of the mix experiments described in this and the following subsections are summarized in Table 4-1. The mean and standard error are shown of the DD-n and D^{3}He yields (Y_n and Y_p), the DD and D^{3}He compression-bang time, and the areal density ρR inferred from the mean downshift of 14.7 MeV D^{3}He protons for type I, II and III capsules with high and low fill pressure. Also shown is the number of shots of each kind. The mean is the average of measured values for a given kind of shot, and the standard error is the standard deviation of the measurements divided by the square root of the number of shots.

Table 4-1: Experimental timing, yield, and compression results of type I, II, and III capsules with different fill pressures. The values shown are the mean and error of the mean for all shots in a particular group. Only the compression component of the D^3He yield is quoted for type I capsules.

Type	Pres (atm)	Num shots	DD bang (ps)	err	DD burn (ps)	err	D^3He bang (ps)	err	D^3He burn (ps)	err	Y_n ($\times 10^8$)	err (%)	Y_p ($\times 10^7$)	err (%)	ρR (mg/cm^2)	err
I	18	8	1753	22	157	9	1736	17	155	11	129	6.1	61.0	10	49.3	1.3
"	3.6	8	1694	20	148	11	1700	14	123	12	29	8.8	30.4	16	55.9	1.3
II	20	7	-		-		1830	32	154	15	5.1	9.2	1.68	11	58.3	3.1
"	4	5	-		-		1785	21	153	13	9.4	6.9	2.96	13	60.5	3.2
III	4	1	-		-		-		-		1.27	10	0.28	10	52.9	5.8

4.3.2 Timing measurements

No D^3He protons were seen at shock-bang time in the D^3He reaction history of type II capsules (Figure 4-5). This observation demonstrates that there is no fuel-shell mix at shock-bang time, or at least that any such mix is not heated sufficiently for nuclear production. This is consistent with the picture that shock-bang time occurs before the deceleration phase (Table 2-4), when saturation of RT growth induces turbulent mixing.

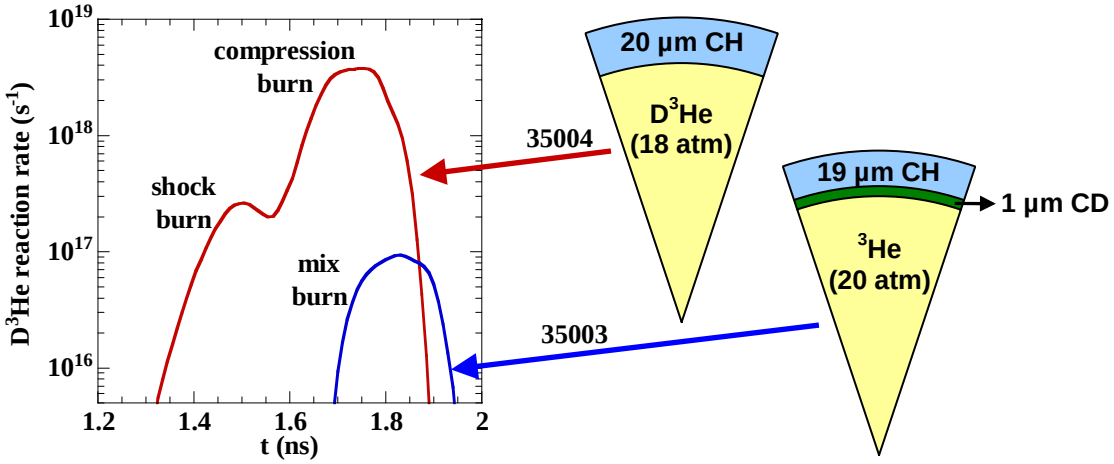

Figure 4-5: Measurements of the D^3He burn history of CD-layer (type II) capsules show that they experience fuel-shell mix during the deceleration phase, but that there is no mix at shock-bang time (or at least, any such mix is not heated). Bang time in type II implosions occurs later than compression-bang time in type I implosions. Nuclear production in type II implosions continues even after the compression burn ends in type I capsules, staying well above the typical type II noise level of about 2×10^{15}/s for an additional 50 ps.

The DD-n and D^3He compression bang times measured by NTD and PTD are in good agreement for type I implosions, yet the D^3He bang time occurs 90 ps later for type II than for type I implosions, as shown in Figure 4-6 (also see Table 4-1). This bang time delay is consistent for both high and low fill pressures. The D^3He burn duration for type I and II targets were

consistent (within the measurement uncertainty of the instrument) at about 150 ps. An interesting consequence of the later D^3He bang time and similar burn duration of type II implosions compared to type I is that the nuclear production in type II implosions continues even after nuclear production in type I implosions has ended (see Figure 4-5).

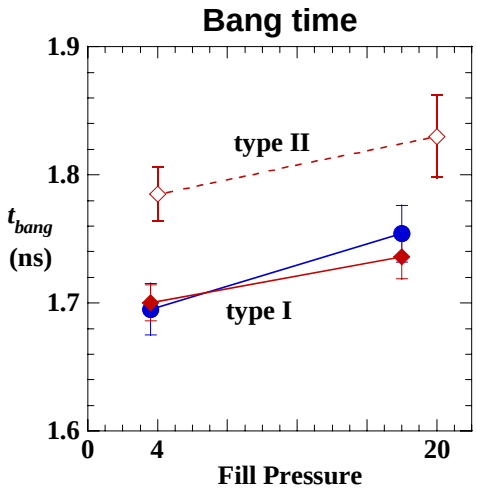

Figure 4-6: D^3He (red diamonds) and DD-n (blue circles) compression-bang times from type I (solid markers) and type II (open markers) implosions as a function of capsule fill pressure. Markers and error bars show the mean of and standard error in the bang time for a given kind of shot. The D^3He bang time occurs about 90 ps later for type II targets.

The timing difference of type I and II capsules is not caused by hydrodynamic differences due to changes in the fill composition. As was shown in Chapter 3 and reference [59], the timing of nuclear production is the same for hydrodynamically-equivalent mixtures of D_2 and ^3He, even for mixtures of nearly pure ^3He. However, yields from capsule implosions with ^3He-rich fuels were observed to be as much as a factor of two higher than for equimolar D^3He fuel.

A possible explanation for the observed delay in the reaction history for type II capsules is due to the difference in how mix caused by the RT instability effects nuclear production in type I and II capsules. Whereas mix tends to quench the nuclear production in type I capsules through dilution and cooling of the hot fuel, in type II capsules, mix enhances nuclear production by the addition and heating of the D reactant in the shell.

Nuclear production in type II capsules does not occur until later in the deceleration phase, when the growth and saturation of the RT instability can induce turbulent mix. The enhancement of the reactant densities by continued mix in the later stages prolongs nuclear production even after the burn would have been quenched in a type I implosion.

4.3.3 Compression measurements

Further evidence for the delay in nuclear production can be found through measurement of the compression of the target at bang time by means of ρR. Areal density is inferred from the mean downshift of the D^3He proton spectrum from their birth energy of 14.7 MeV, so the inferred ρR is an average measurement of ρR over the time of nuclear production. Because the capsule continues to compress, and ρR to increase, throughout the deceleration phase, one would

expect that if bang-time occurs during a later stage of the deceleration phase for an otherwise equivalent implosion, then the average ρR would be higher.

As seen in Figure 4-7, the inferred burn-averaged ρR is higher for implosions of type II capsules than for type I capsules. This is qualitatively consistent with the later bang-times measured for type II capsules. However, it should also be considered that a similar increase in ρR was sometimes seen in type I capsules with high (but not pure) concentrations of ^{3}He compared to standard D^{3}He mixtures (see Figure 3-8).

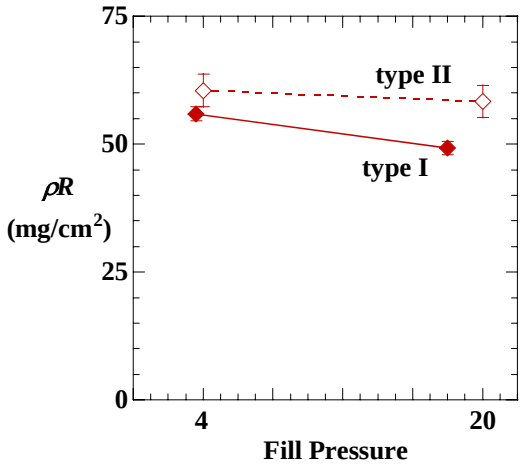

Figure 4-7: Mean and standard error of ρR's for type I (filled markers) and type II (open markers) implosions as a function of fill pressure. The D^{3}He burn averaged ρR is higher for type II capsule because bang time occurs later.

4.4 Constraining the extent of mix at shock time

Comparative analysis of D^{3}He-p spectra from type I and II implosions can be used to place an upper bound on the possible amount of mix at shock time. For the representative spectrum of a type I capsule shown in Figure 4-8, the total yield in the region from 14.2 to 14.7 MeV, corresponding to the shock component, is $1.70\pm0.15\times10^7$, or $3.72\pm0.34\%$ of the total yield. The yield in the same region of the representative spectrum from a type II capsule comes to $2.6\pm2.5\times10^4$, equal to $0.14\pm0.13\%$ of the total yield, and consistent with zero.

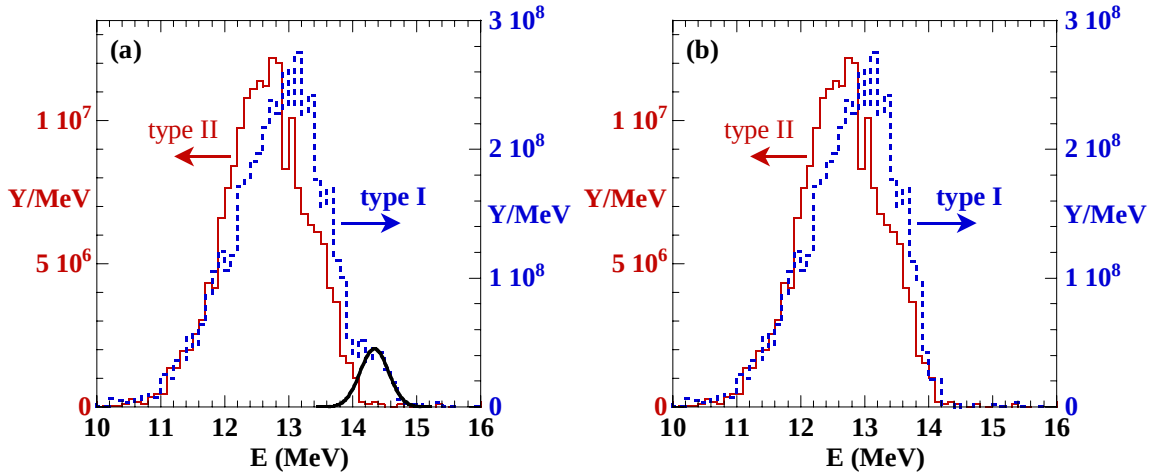

Figure 4-8: (a) WRF spectra for 20 μm shell implosions of type II (shot 32828, solid red) and type I (shot 37642, dotted blue) capsules. Also shown (solid black) is the shock component fit to the spectrum of shot 37642. (b) Same spectra, but with the shock component subtracted from the spectrum of shot 37642, demonstrating that the type II spectrum has the same "look" as a type I spectrum with no shock.

The total "shock yield" of the type II implosion ($\leq 2.6\times10^{4}$) comes to at most 0.15% of the shock yield of the corresponding type I implosion (1.7×10^{7}). This yield ratio can be used to impose a constrain on the deuterium fraction in the type II implosion, $f_D \leq 0.05\%$, through application of Equation (3-5). This constraint is likely a bit conservative, since we'd expect the scaled shock yield in a nearly pure ^{3}He gas to be larger, due to both the stronger ion heating, and due to the "equivalence" scaling (Chapter 3 and reference [59]). The use of Equation (3-5) implicitly assumes that f_D is uniform through the fuel region, so does not preclude the more likely physical situation of deuterium concentrations higher than the above constraint in the outer, cooler region of the fuel.

A similar method to constrain the D^{3}He shock yield in type II capsules, can be applied using the D^{3}He temporal burn history. The higher relative noise level on PTD compared to the WRFs results in a weaker constraint: the D^{3}He shock yield in type II implosions cannot be higher than 1% of the total yield. This constrains $f_D \leq 0.5\%$, using the same assumptions described above.

Limits on the relative shock yields in type I and II implosions could provide a useful way to distinguish between contamination and mix in other types of mix experiments. For example, Wilson *et al* [73] reported significant DT nuclear production in the later stages of the coasting phase in implosions of tritium filled, CD shelled capsules (much like the type II capsules, but with a T_2 fill gas instead of ^{3}He). The DT yield before the shock reached the ingoing plastic shell accounted for about 10% of the total yield. Wilson *et al* proposed chemical exchange of D in the shell with T in the gas, or a gas jet induced by the support stalk as possible mechanisms to insert D into the gas by the time of shock-burn. The original contamination of D in the T_2 was at least a factor of 20 too low to be the source. The low D^{3}He yields from the type II capsule experiments suggest that it is chemical exchange (which does not occur with ^{3}He fill) rather than a gas jet (which would occur for ^{3}He fill) which introduces the early D contamination.

4.5 Mix Summary

The extent of fuel-shell mix has been shown to include a substantial amount of the shell from the inner 1st and 2nd μm of the original material using a novel target configuration. The observed yields are higher than is consistent with diffusive mixing, and so must be the result of turbulent mixing down to the atomic scale.

The improved stability of capsules with higher initial fuel density to mix induced by hydrodynamic instabilities has been confirmed by comparing the yield trends of type I and II capsules. Increasing the capsule fill pressure decreased the D^3He and DD-n yields for type II capsules, and increased the yields for type I capsules demonstrates that the extent of mix is reduced for increasing fill pressure.

The D^3He bang time for type II capsules occurs 90 ps later than for type I capsules, independent of the initial fill pressure. This delay is attributed to the time it takes for the RT instability to saturate and induce turbulent mixing. The continued mix and transport of heat into the mix region maintains the nuclear production in type II capsules even after it is quenched in type I capsules.

The D^3He shock yield in type II capsules with high pressure was constrained to be less than 0.14% of the total yield, and the atomic fraction of deuterium in the fuel during the shock-burn has been constrained to be less than 0.05%, and is consistent with zero.

5 Shock Convergence

Precise timing of multiple shocks is of critical importance for ignition and high gain in inertial confinement fusion (ICF). Strong, spherically convergent shocks are formed by such events as the onset and rise of the laser pulse intensity. Any shocks formed after the first shock must propagate through already-shocked material, which introduces uncertainty into the shock speed and strength. Shock mistiming could prematurely heat the cold fuel, or could inadequately heat the hot-spot, leading to failed ignition or reduced gain. Thorough understanding of shock speeds in cold and heated material, and in planar and convergent geometries, will be essential for satisfactory ICF implosion performance.

Previous studies of shock propagation relevant to ICF have largely focused on planar geometry [74][75]. The planar approximation works well for the propagation of converging shocks in the shell at early times, but breaks down as the shock approaches the center of collapse.

This chapter presents results of nuclear measurements of the shock collapse. Preliminary results of these measurements were published in references [62] and [54]; this chapter will expand on those results. Section 5.1 provides a brief review of shocks, and Section 5.2 describes the role of shocks in ICF. Section 5.3 shows the results of experimental observations of the shock burn in ICF implosions, along with a brief discussion of the implications of the observed trends, and a comparison to 1-D simulations. Section 5.4 explains the experimental setup and observations made of the shock burn induced by an asymmetric laser drive. Section 5.5 summarizes the results and conclusions.

5.1 Shocks

Shocks are disturbances in a fluid that propagate faster than the local speed of sound. They can be formed by rapid energy deposition (such as the absorption of intense laser light) or by the interaction of supersonic flows (such as motion of, or collisions between, objects moving at supersonic speeds) [21]. The shocking of a material changes its flow parameters (velocity, density and pressure), and results in an irreversible change in entropy. The location of the abrupt change in flow parameters is referred to as the shock front, and is often idealized as a true discontinuity, although real shock fronts will have a finite width which is characterized by the mean free path of the constituent particles.

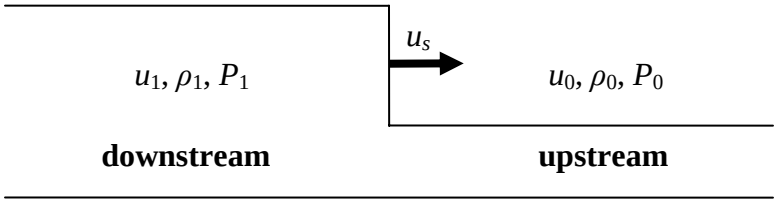

Figure 5-1: Example of a planar shock. The shock front moves to the right at speed u_s, into the "upstream" medium. The passage of the shock front results in a "downstream" medium with higher density (ρ) and pressure (P) than the upstream medium.

[21] A familiar example of a shock is the "sonic boom" heard shortly after being passed by a supersonic aircraft.

Figure 5-1 sketches the scenario of a shock front in planar geometry. The shock front moves into the unshocked, "upstream" medium (denoted by subscript 0) at speed u_s. The passage of the shock front results in a sudden change in the velocity u, density ρ, and pressure P of the downstream medium (denoted by subscript 1) with respect to their upstream values. Any velocity components tangential to the shock surface must be continuous across the shock front, and can be set to zero with an appropriate choice of coordinate system.

The boundary conditions at the shock front can be determined using conservation of mass, momentum, and energy in a fluid system:

$$\begin{aligned} \rho_1 v_1 &= \rho_0 v_0, \\ P_1 + \rho_1 v_1^2 &= P_0 + \rho_0 v_0^2, \\ \varepsilon(P_1,\rho_1) + \frac{P_1}{\rho_1} + \frac{1}{2}v_1^2 &= \varepsilon(P_0,\rho_0) + \frac{P_0}{\rho_0} + \frac{1}{2}v_0^2, \end{aligned} \tag{5-1}$$

where v is the fluid velocity with respect to the shock front, $v_i = u_i - u_s$. The specific energy ε is the energy per unit mass of the fluid, and is a function of density and pressure, $\varepsilon = \varepsilon(\rho,P)$, whose specific form depends on the equation of state (EOS) of the fluid.

For an ideal gas with adiabatic index γ, the specific energy can be expressed as $\varepsilon = P/\rho(\gamma - 1)$, and Equations (5-1) can be solved for the density or pressure ratio across the shock front:

$$\begin{aligned} \frac{\rho_1}{\rho_0} &= \frac{(\gamma+1)P_1 + (\gamma-1)P_0}{(\gamma+1)P_0 + (\gamma-1)P_1}, \\ \frac{P_1}{P_0} &= \frac{(\gamma+1)\rho_1 - (\gamma-1)\rho_0}{(\gamma+1)\rho_0 - (\gamma-1)\rho_1}. \end{aligned} \tag{5-2}$$

This pressure ratio is an explicit form of the Hugoniot relation for ideal gases. Considering the case of a stationary upstream medium (which can be satisfied in all cases by a change of reference frame), the speed of the shock can be related to the speed of sound in the upstream medium (c_{s0}) using the ratio of downstream to upstream pressures; for an ideal gas this takes the form:

$$u_s^2 = \frac{c_{s0}^2}{2\gamma}\left[(\gamma-1) + (\gamma+1)\frac{P_1}{P_0}\right], \tag{5-3}$$

where the speed of sound in an ideal gas is given by $c_s^2 = \gamma P/\rho$. The shock speed is often characterized by the Mach number M_s, which is the ratio of the shock speed to the local speed of sound in the upstream medium, $M_s = u_s/c_{s0} > 1$.

Weak shocks, characterized by $M_s \approx 1$ (or equivalently, $P_1/P_0 \approx 1$), propagate at nearly the speed of sound, and have very small pressure, density, and velocity changes across the shock front.

Strong shocks are characterized by $M_s >> 1$ (or equivalently, $P_1/P_0 >> 1$). A fluid cannot be compressed to arbitrary densities by a single strong shock; the compression ratio is limited to:

$$\frac{\rho_1}{\rho_0} = \frac{\gamma+1}{\gamma-1}, \tag{5-4}$$

which for a monatomic gas with $\gamma = 5/3$ is equal to 4. Since the density does not depend on the downstream pressure for very strong shocks, the downstream temperature is proportional to the pressure:

$$T_1 = \frac{\rho_0}{\rho_1}\frac{P_1}{\rho_0} = \frac{\gamma-1}{\gamma+1}\frac{P_1}{\rho_0}. \tag{5-5}$$

The speed of a strong shock is related to the downstream pressure over the upstream density:

$$u_s^2 = \frac{\gamma+1}{2}\frac{P_1}{\rho_0}, \tag{5-6}$$

in the frame where $u_0 = 0$. The downstream fluid velocity after a strong shock in this frame is:

$$u_1 = \frac{2}{\gamma+1}u_s, \tag{5-7}$$

which for a monatomic ideal gas is equal to 3/4 of the shock speed.

A further consideration arises in the analysis of shocks in plasmas, due to the fact that a plasma is a two-component system. The two components (ions and electrons) have dramatically different masses; this allows distinct electron and ion temperatures to be sustained. A consequence of the distinct temperatures and different masses is a more complex shock structure, as shown in Figure 5-2.

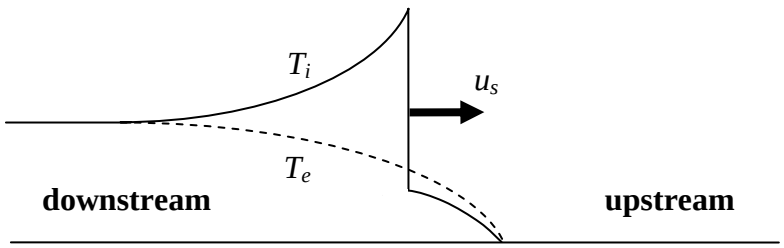

Figure 5-2: A planar shock in a plasma. A shock "precursor" due to electron thermal conduction precedes the shock front; and a relaxation tail follows the shock front as the electron and ion temperatures (T_e and T_i) equilibrate.

The temperature of a fluid increases at a shock front due to viscous heating of the upstream medium by the supersonic flow behind the shock front. The viscosity of a plasma is dominated by the massive ions, which absorb the majority of the thermal energy imparted by the shock.[22] The long thermal equilibration time between electrons and ions (see Chapter 6) results in a thermal relaxation tail behind the shock front. The high thermal conductivity of the low-mass

[22] The thermal energy absorbed by a particle species is proportional to its mass and fractional number density. For example, in a pure D_2 plasma, the ions absorb 3670 times more thermal energy than the electrons.

electrons allow them to smooth out their temperature profile, and in fact even to heat material before arrival of the shock front in a shock "precursor".[23]

The characteristic scale length of both the shock precursor and the relaxation tail increases with the electron-ion thermal equilibration time τ_{eq}, which in turn scales with electron temperature T_e, mass density ρ, and mass ratio as: $\tau_{eq} \sim T_e^{3/2}\rho^{-1}(m_i/m_e)^{1/2}$. The structure of the shock front strongly depends on plasma parameters, and in the limit of a cold, dense plasma, the ideal shock front structure is recovered.

Readers with interest in additional details of shock dynamics are referred to the books by Zel'dovich and Raizer [21] and Drake [22].

5.2 Shocks in ICF

In ICF, shocks play a crucial role in setting the entropy of the high-density fuel, and in heating the hot-spot. In order to ignite a capsule, the hot-spot must be heated as much as possible to maximize the initial self-heating. In addition, to achieve maximal gain, a high areal density must be obtained through extreme compression of the cold fuel. Premature heating of the cold fuel by a strong shock will reduce its compressibility, yet a strong shock is necessary to adequately heat the hot-spot. A careful balance must be maintained between maximization of cold fuel compression and hot-spot heating.

Although limited compression can be attained with a single strong shock, a sequence of multiple, weaker shocks can attain higher compression without excess heating. If these shocks can be timed to coalesce at the inner surface of the high-density fuel, a single, stronger shock will form, which will more effectively heat the low density hot-spot, and induce ignition.

The adiabatic compression heating of the hot-spot by the imploding shell can be further enhanced by a suitably strong convergent shock. An ingoing shock will gain strength due to spherical convergence effects as it nears the center, increasing its effective heating. After the shock collapses at the center, a second, outgoing shock will be formed which will further heat and compress the inflowing fuel material. Chapter 6 discusses the collapsing shock in additional detail.

Current ignition designs plan to coordinate such a multi-shock series to simultaneously coalesce at the inner surface of the DT ice [76]. The precise timing of multiple shocks depends on tight control of the laser pulse shape, as well as a thorough understanding of shock speeds in heated gases. Shock mistiming could prematurely heat the cold fuel, or could fail to adequately heat the hot-spot, leading to failed ignition or reduced gain.

A two-shock sequence occurs in OMEGA targets scaled from ignition designs, and irradiated with a 1ns square laser pulse, as can be seen in Figure 5-3. The incidence of the laser pulse launches the first strong, ingoing shock into the plastic shell. The breakout of the shock from the inside of the shell forms a rarefaction (decompression wave) that travels back through the shell, and eventually returns to the ablation front. The shape of the density and pressure profiles in the shell at the time the rarefaction reaches the ablation front initiates acceleration of the shell, and the resulting compression wave soon forms into a second ingoing shock.

[23] The downstream electron thermal speed is larger than the shock speed, which is proportional to the downstream ion thermal speed. This "speed" advantage allows the electrons to reach slightly past the shock front.

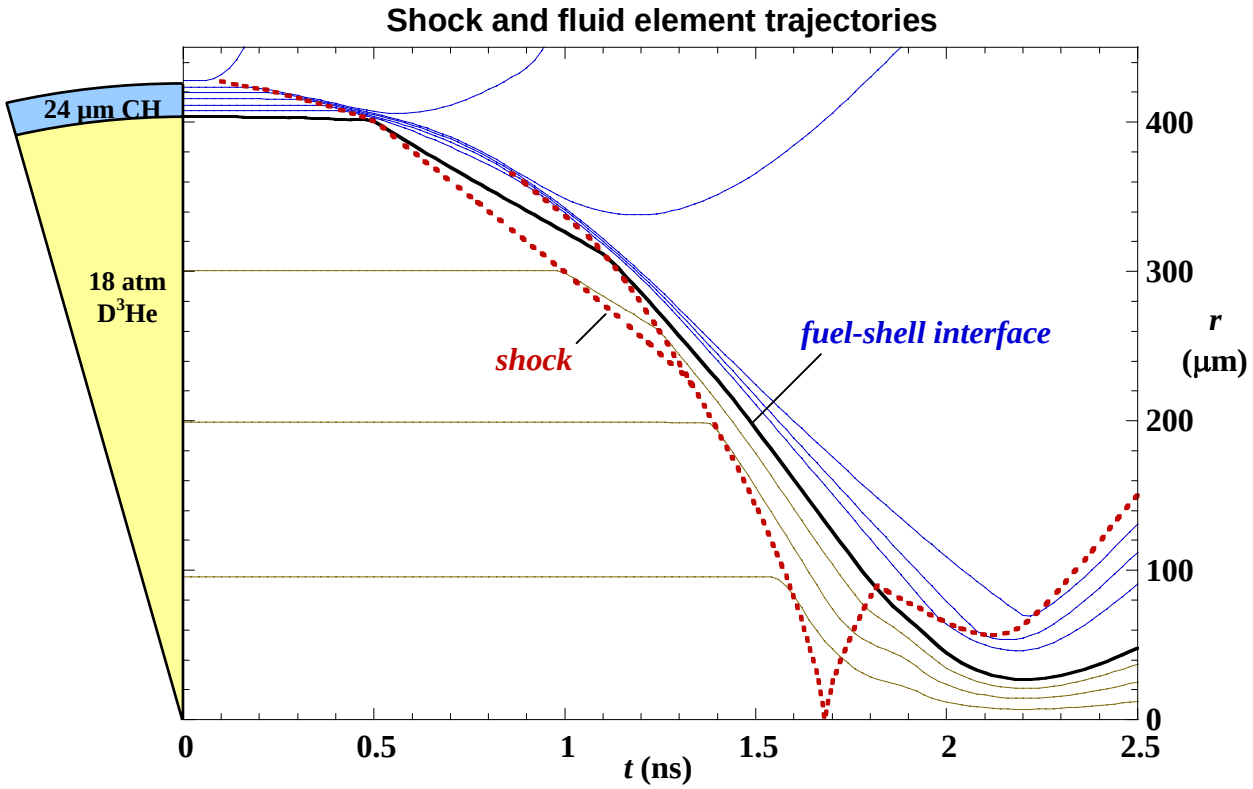

Figure 5-3: Diagram of the shock trajectory, as well as trajectories of selected fluid elements in r-t space in a simulation of shot 38525 (from Figure 2-7b). Shot 38525 had a 24 μm, 18 atm D^3He target (see capsule section, left side). It was shot with a 22 kJ, 1 ns square laser pulse, and was simulated using the "new" input deck with a flux limiter $f = 0.06$. The shock trajectory near the instant of shock collapse is not calculated directly by the simulation, and so instead is plotted using a Guderley shock trajectory (see Chapter 6).

This second shock moves more rapidly through the already-shocked material, and coalesces with and strengthens the first shock before it converges toward the center. After the shock collapses at the center, a reflected, outgoing shock is created, that reheats the already shocked material to the point that fusion starts to occur. The deceleration phase then begins when the outgoing shock encounters the ingoing shell. The transmitted shock continues to propagate outwards as the shell compresses the fuel and decelerates due to the resulting high pressure that is generated as a result.

Nuclear production during and shortly after the shock collapse can be hard to simulate precisely due to ion mean-free-paths that are longer than the simulation mesh size, and due to rapid fluid dynamics that take place before the plasma in a simulation zone has time to thermalize. The assumptions of short mean free paths and rapid equilibration compared to simulation mesh sizes and time scales are valid for nuclear production during the deceleration phase, but the breakdown in these assumptions near shock bang time can complicate the calculation of many important effects, such as thermal conduction and nuclear production.

5.3 Nuclear measurements of shock burn

Direct-drive implosions were conducted at OMEGA [30], with 60 beams of frequency-tripled (351 nm) UV light in a 1-ns square pulse and a total energy of 23 kJ. SG4 phase plates [36], and 1 THz bandwidth smoothing by spectral dispersion of the laser beam were used [37]. The beam-to-beam energy imbalance was typically between 2 and 4% rms. The spherical capsules had diameters between 860 and 880 μm, plastic shell thicknesses of 15, 20, 24, or 27 μm, and a flash coating of about 0.1 μm of Aluminum. The capsules were filled with an equimolar (by atom) mixture of D_2 and ^3He with a total fill pressure of 3.6 or 18 atm.

Diagnostics for this study were the proton and neutron temporal diagnostics (PTD and NTD) [54][52], to measure the D^3He and DD-n reaction histories; multiple wedge-range-filter (WRF) spectrometers [42], to measure the D^3He proton yield and spectrum; and the magnet-based charged-particle spectrometer (CPS-2) [42], to measure the DD protons emitted at shock-bang time (see Section 2.6).

5.3.1 Shock timing

The D^3He proton production history shows two distinct times of nuclear production (Figure 5-4a): "shock-burn" begins shortly after shock collapse, and ends near the beginning of the deceleration phase; "compression-burn" begins near the onset of deceleration phase, and lasts approximately until stagnation. 1-D hydrodynamic simulations of the implosions with LILAC [31] show the same components in the D^3He burn history, but the simulations typically predict a higher production rate, and a later bang time (Figure 5-4b).

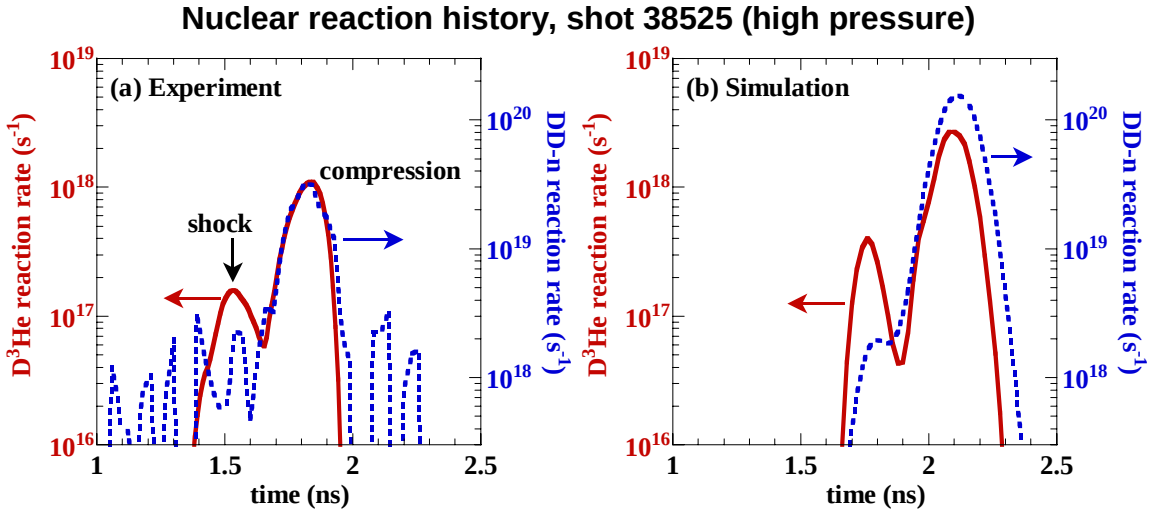

Figure 5-4: D^3He proton (solid red) and DD-n (dotted blue) reaction rates from a 24 μm thick CH shell filled with 18 atm of D^3He (shot 38525). (a) Experimental observations. (b) Simulated burn history, using the code LILAC with the new input deck and $f = 0.06$. The simulations typically predict a higher production rate, and a later bang time.

The shock burn is relatively small compared to the compression burn in the DD-n nuclear production history. The weaker dependence of the DD-n thermal reactivity on temperature results in less of a nuclear production boost during the shock-burn phase compared to the D^3He history. For ordinary D^3He mixtures, the DD-n reaction rate at shock-bang time is below the

noise level; however, for shots of capsules filled with pure D_2, the DD-n shock reaction rate comes above the noise, and can be directly measured with NTD (Figure 5-5).

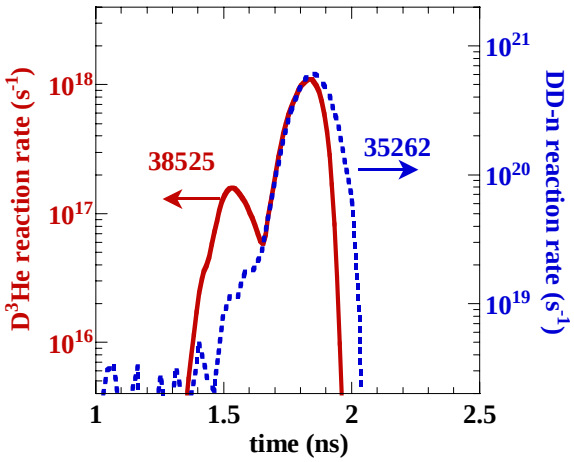

Figure 5-5: Reaction rates of D^3He from shot 38525 (solid red) and DD-n from shot 35262 (dotted blue). These shots were hydrodynamically-equivalent D^3He and pure D_2 fills of 24 μm thick CH shells. The pure D_2 fuel gives a NTD signal that is well above the noise, allowing measurement of the DD-n shock burn. The shock yield in these capsules is only about 1.5% of the total DD-n yield, whereas it makes up about 11% of the D^3He yield.

Shock-bang times observed by PTD and simulated by LILAC are shown in Figure 5-6, and the shock burn duration observed by PTD is shown in Figure 5-7, for capsules with different fill pressures and shell thicknesses. The shock bang time is the time of peak D^3He nuclear production during the shock-burn phase, and the shock-burn duration is the full-width at half maximum (FWHM) of the shock peak in the D^3He reaction history. These figures plot the mean and standard error among values for a given type of shot; the calculation of these values is discussed in Appendix B.

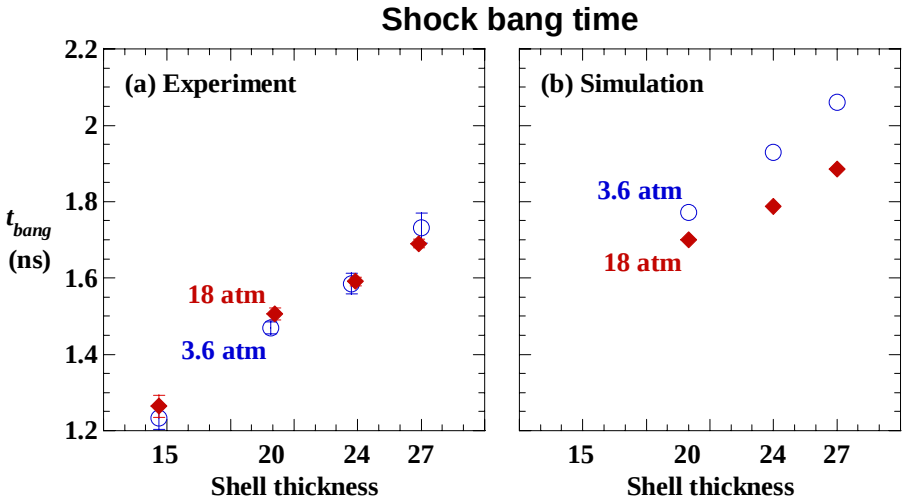

Figure 5-6: (a) Experimental and (b) simulated shock-bang time as a function of shell thickness for capsules filled with 18 atm (solid diamonds) and 3.6 atm (open circles) of D^3He. Markers and error bars show the mean and error among measured values of a certain capsule type.

Simulations predict much later shock-bang times than is seen in the experiments. The simulations predict shock-bang time to occur 200 ps later in capsules with 18 atm fills, and 300 to 350 ps later in capsules with 3.6 atm fills. This is well outside of the experimental error; the standard error in the experimental shock-bang time is typically less than 20 ps, and always less than 35 ps. The simulated shock-bang time can be adjusted to match experiment by increasing the flux limiter; however, increasing the flux limiter will also push the shock yield and ρR to further disagreement with experiment.

Experiments and simulations both show that shock-bang time occurs later in implosions of capsules with thicker shells. This time delay is linear with shell thickness, with an additional delay of 37 ps per μm of additional shell thickness for experimental shock-bang times. A shock-bang time delay of 41 and 26 ps per μm is seen in capsules filled with 3.6 and 18 atm D^3He, respectively. This linear time delay is due to both the longer propagation time of the 1st shock transit through the shell, as well as linear delays of the return rarefaction and second shock through the added shell thickness.

Experimental observations demonstrate that shock-bang time is independent of capsule fill pressure, in contrast with expectations based on 1-D simulations. The simulations predict that shock-bang time will occur 100 to 150 ps later for 3.6 atm compared to 18 atm fills of capsules with the same shell thickness.

The duration of the shock burn is not apparently affected by the thickness of the shell. Reduction of the fill pressure from 18 atm to 3.6 atm seems to reduce the shock-burn duration by about 20 ps. This trend is particularly surprising given that shock-bang time does not depend on fill pressure.

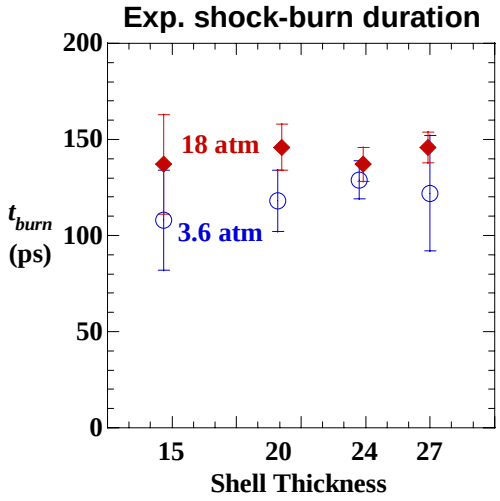

Figure 5-7: Experimental shock-burn duration as a function of shell thickness for capsules filled with 18 atm (solid diamonds) and 3.6 atm (open circles) of D^3He. Markers and error bars show the mean and error among measured values of a certain capsule type. The shock burn duration is shorter for low fill pressure, but is independent of shell thickness.

5.3.2 Shock yields

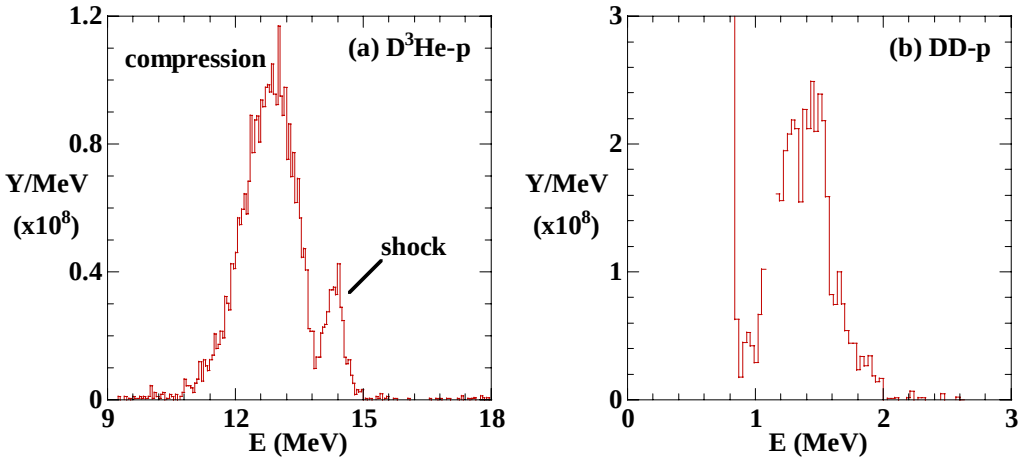

Figure 5-8: (a) Spectrum of emitted D^3He protons from shot 38525, showing shock and compression components. (b) Spectrum of emitted DD-p from the same shot. The DD-protons are only emitted at shock time, before the ρR gets too high. The break in the spectrum at E = 1.05 MeV is due to a small gap between adjacent detectors in CPS-2. The sharp increase in the spectrum at E = 0.83 MeV is the proton ablator endpoint feature[24]. Shot 38525 had a 24 μm thick capsule filled with 18 atm of D^3He.

Distinct shock and compression components can often be seen in D^3He proton spectra (Figure 5-8a). The protons emitted at shock-bang time experience relatively little downshift (~0.4 MeV) due to the low total areal density (ρR) at that time. The shell continues to compress as the shock burn ends, and by compression-bang time the areal density has increased enough to downshift the D^3He protons by several MeV.

The areal density at shock-bang time is low enough to also allow the 3.0 MeV DD protons to escape the capsule (Figure 5-8b). Measurement of DD protons emitted at shock time provide a valuable measurement of the DD shock yield when the reaction rate is below the NTD threshold, or a double check of the DD shock yield otherwise. Measurement of their downshift can also provide a double check on the ρR at shock-bang time inferred using the D^3He proton spectra, or the sole measurement in cases where the shock component of the D^3He proton spectrum cannot be separated from the compression component. The shock-burn contribution to the total DD yield is typically about 1-2%, compared with 5-20% for the D^3He shock-burn contribution to the total yield.

[24] The capsule typically charges up to a bit less than a megavolt while the laser is on, due to ejection of fast electrons generated through laser-plasma instabilities. Copious protons (>10^{15}) from the shell (or "ablator" material) are accelerated by the resulting large radial electric field, and detected by CPS. See Section 2.6.2.

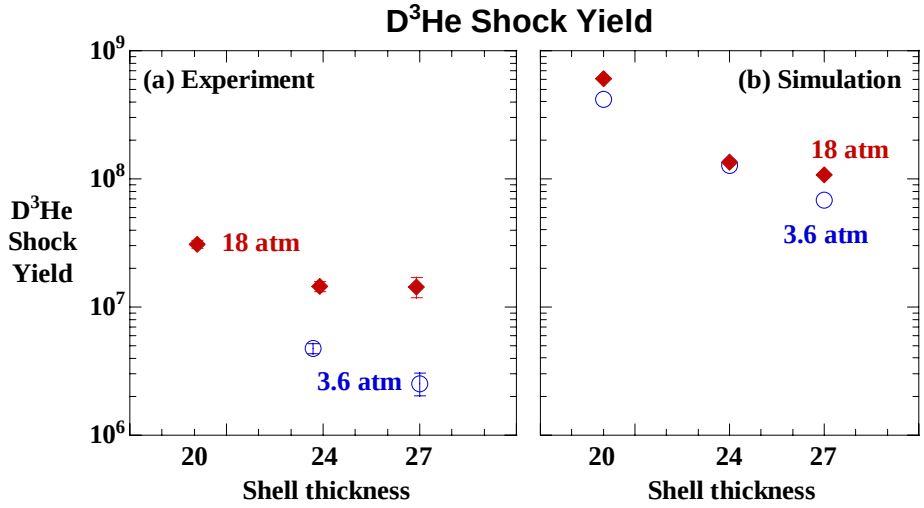

Figure 5-9: (a) Experimental measurements and (b) numerical simulations of D^3He shock yields as a function of shell thickness for capsules filled with 18 atm (solid diamonds) and 3.6 atm (open circles) of D^3He. Simulations always predict much higher shock yields than are measured experimentally.

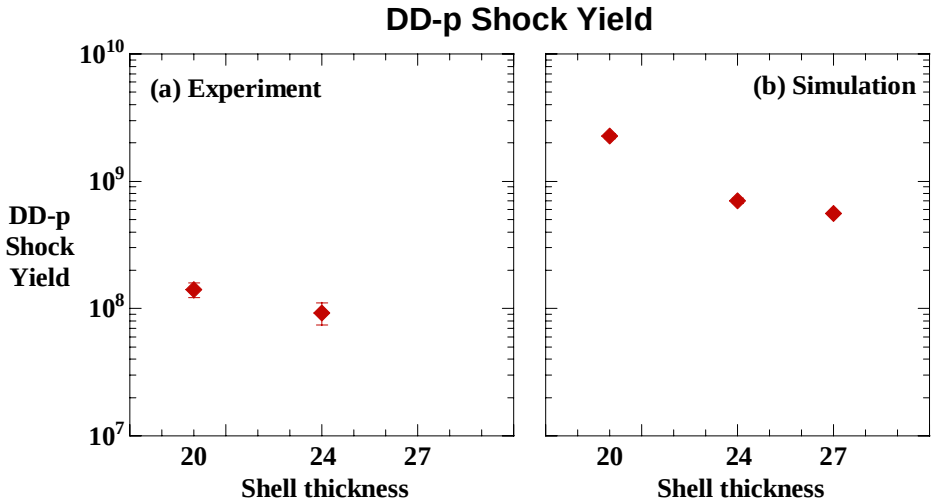

Figure 5-10: (a) Experimental measurements and (b) numerical simulations of DD-p shock yields as a function of shell thickness for capsules filled with 18 atm of D^3He. Simulations always predict much higher shock yields than are measured experimentally.

The observed D^3He shock yield is lower for implosions of targets with thicker shells and lower fill pressures. Figure 5-9 shows the experimental and simulated D^3He shock yield trends for implosions of targets with 20, 24, and 27 μm thick CH shells filled with 3.6 and 18 atm of D^3He. Figure 5-10 shows the experimental and simulated DD-p shock yield trends.

1-D simulations tend to over-predict both the D^3He and DD-p shock yields. The YOC (experimental yield over simulated yield) for D^3He shock yields is about 3.5% in low pressure targets, and 5-12% in high pressure targets. The DD-p shock YOC is 7-14%. The simulated shock yields can be adjusted to match experiment by decreasing the flux limiter; however, decreasing the flux limiter will also push the shock-bang time to further disagreement with experiment. No value of the flux limiter can match both the shock timing and yield simultaneously (Figure 5-11).

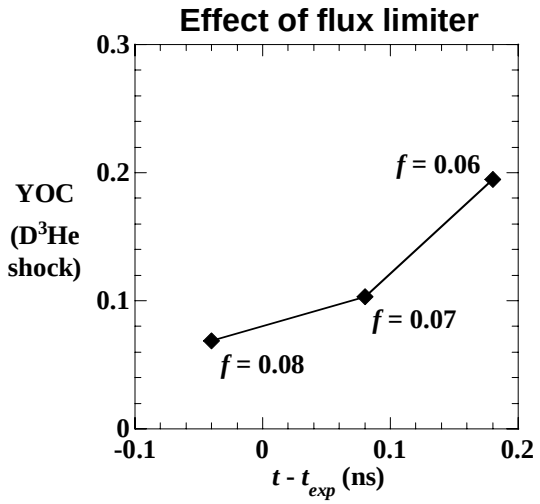

Figure 5-11: The D^3He shock YOC (defined as the experimental D^3He shock yield over the simulated yield) as a function of the time delay of the simulated shock-bang time compared to the experimental shock-bang time, shown for simulations of shot 36586 (high pressure fill of 19 μm thick shell) with flux limiters of 0.06, 0.07, and 0.08. The flux limiter can be adjusted to change the shock yield and shock-bang time, but no value of the flux limiter can match both experimental values (which would correspond to the point (0,1) in the plot).

The shock yield is reduced for implosions of targets with thicker shells due to the weaker coalesced shock that is generated in thicker shells. The rarefaction that returns to the ablation front from shock breakout will have shallower density and pressure gradients due to the added thickness. These smaller gradients result in the formation of a weaker second shock, which takes longer to catch up with the first and is then slower to collapse at the center. The weaker shock collapse is the reason for the lower yields.

The lower fuel density in targets with low fill pressure is the reason for the reduction in shock yields compared with high pressure targets. However, the reduction factor takes a lower value than the value of 25 expected from only the density dependence of the nuclear fusion rate. The lower density results in less efficient thermal coupling between ions and electrons, so that the ion temperature, and consequently the nuclear fusion rate, stays higher.

The lower shock YOCs and the additional delay in shock-bang time for implosions of targets with low fill pressure is not due to a later shock collapse, but rather due to additional heating of the fuel from a reflection of the outgoing shock from the ingoing shell[25]. No evidence of heating due to this shock reverberation is seen in the experimental reaction rates (see Figure 5-12).

[25] This reflection event would occur at t =1.8 ns, r =80 μm on the plot in Figure 5-3.

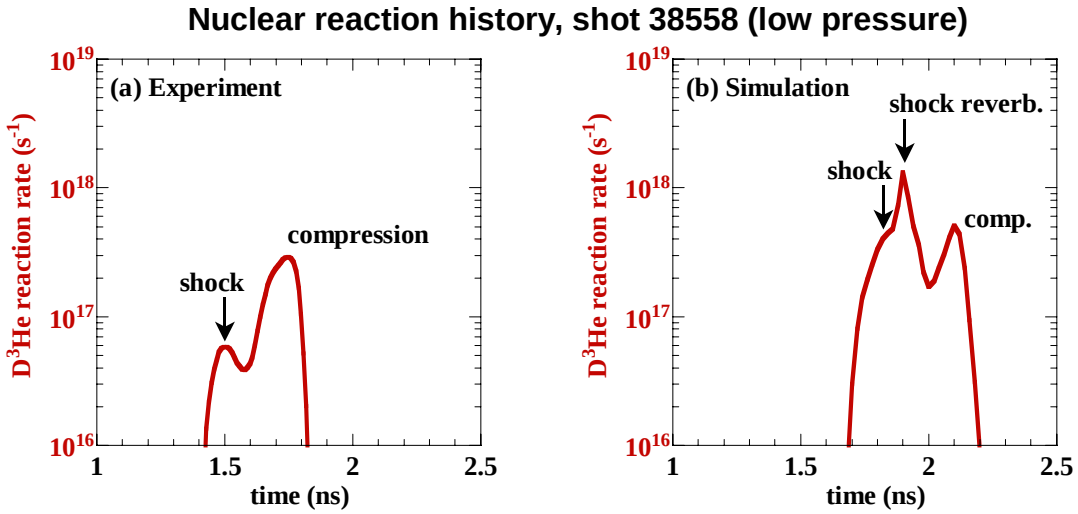

Figure 5-12: D^3He proton reaction rate from a 24 μm thick CH shell filled with 3.6 atm of D^3He (shot 38558). (a) Experimental observations. (b) Simulated burn history, using the old input deck. No evidence of the reverberating shock predicted in the simulations for low pressure fills is observed experimentally.

Measurement of two nuclear products at shock-bang time allows the use of the ratio method (see Figure 2-21) to infer the shock-burn averaged ion temperature, $\langle T_i \rangle_{sh}$. The shock temperature decreases in implosions of capsules with thicker shells, and simulations anticipate a slightly higher shock temperature than is observed in the experiments. The shock temperature of 5.4±0.4 keV for 24 μm thick shells compares favorably with the value of 6±1 keV obtained by a fit to the shock line, assuming only thermal broadening, reported by Petrasso *et al* [62].

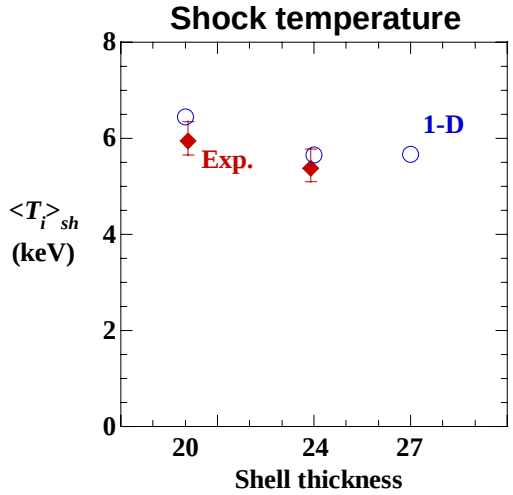

Figure 5-13: Experimental measurements (solid diamonds) and 1-D simulations (open circles) of the shock-burn averaged ion temperature for capsules with 18 atm D^3He. Temperatures were inferred using the ratio method (see Figure 2-21). Simulations predict slightly higher temperatures at shock time.

5.3.3 Shell compression at shock-bang time

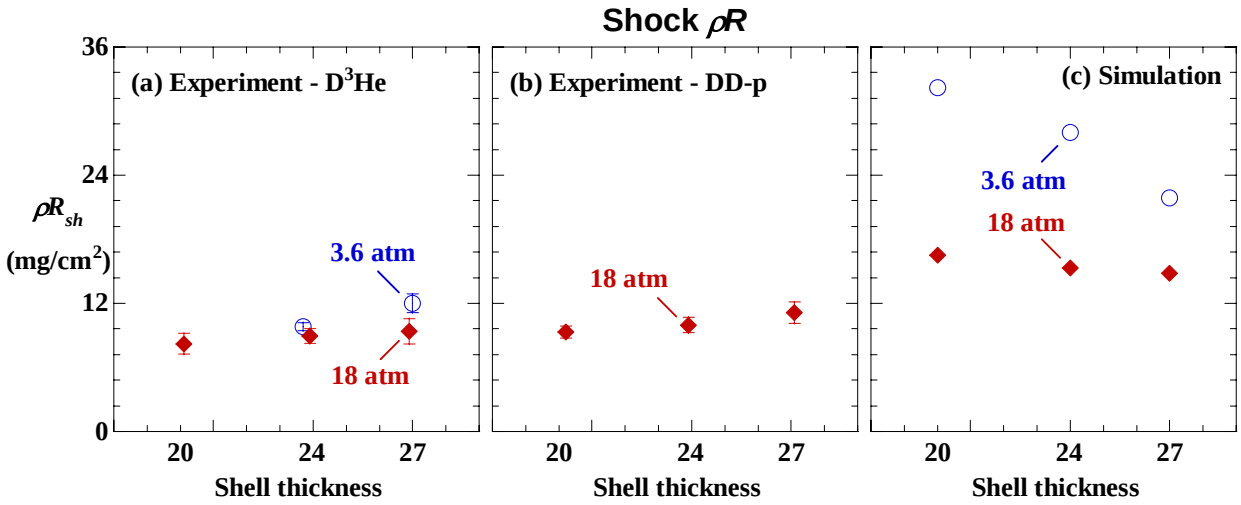

Figure 5-14: Shock ρR's for 18 atm (solid diamond) and 3.6 atm (open circle) D^3He fills of capsules with various shell thickness. The experimental ρR_{sh} is inferred from the downshift of (a) 14.7 MeV D^3He protons and (b) 3 MeV DD-protons from their birth energy. Markers show mean and standard error. (c) The simulated ρR_{sh} is the ρR of the implosion weighted by the D^3He reaction rate over the shock burn.

The compression of the shell at shock-bang time can be quantified by the shock-burn averaged areal density, ρR_{sh}, and is shown in Figure 5-14. Experimentally, ρR_{sh} is inferred from the measured downshift of the mean energy of D^3He protons in the shock line or DD protons measured by CPS from their birth energy. The simulated ρR_{sh} is the ρR weighted by the D^3He reaction rate over the shock burn.

1-D simulations anticipate higher ρR_{sh}'s than were observed experimentally. Experimental ρR_{sh}'s are about 10 mg/cm^2, whereas the simulated ρR_{sh}'s are about 15 mg/cm^2 for 18 atm capsules, and between 22-32 mg/cm^2 for 3.6 atm capsules. The measured downshift of DD-protons confirms the ρR results obtained using D^3He protons.

Experiments and simulations see opposing trends of ρR_{sh} as a function of shell thickness. The shock ρR inferred using the downshift of D^3He and DD protons increases with increasing shell thickness, whereas the simulated ρR_{sh} decreases with increasing shell thickness. Simulations predict much higher ρR_{sh}'s for low pressure fills, whereas only a modestly higher ρR_{sh} was observed experimentally.

There are several competing shell-thickness-dependent effects that could alter ρR at shock time. For the same laser drive, the same amount of shell mass gets ablated, so thicker shells will have a more mass remaining, which should increase ρR. However, the larger payload of the thicker shells will experience less acceleration, and will have a lower implosion velocity during the coasting phase, which will tend to reduce ρR, as the shell will be farther out. Finally, the delay in shock-bang time in targets with thicker shells gives the shell more time to compress before nuclear production begins.

Shock ρR should be the same for high and low pressure fills of targets with the same shell thickness, since the trajectory of the shell should be independent of gas fill pressure until the

deceleration phase. Since shock-bang time occurs before the onset of the deceleration phase, it is puzzling that higher ρR_{sh}'s were observed for low pressure fills.

5.4 Asymmetrically driven convergent shocks

Experimental measurements have demonstrated that shock-bang time and shock yield are both very robust against drive asymmetries. Convergent shocks were driven with two types of asymmetric drives, corresponding to predominantly low ℓ-mode and predominantly high ℓ-mode asymmetries[26]. The D^3He shock bang time and shock yield were measured with the PTD and with WRF spectrometers, respectively.

To investigate the effects of low-mode drive non-uniformities on shock timing and convergence, four campaigns of targets with shell thicknesses of 20, 24, 26, and 27 μm were conducted where capsules were offset from the target chamber center (TCC) by 0, 50, 100, and 150 μm, while the laser beams remained pointed at the nominal, no-offset position. The resulting intensity non-uniformity is dominated by low ℓ modes (ℓ = 1-3), with surface-averaged root-mean-square (rms) variation of 11%, 21%, and 32% for offsets of 50, 100, and 150 μm, respectively. The nominal intensity nonuniformity over all modes for a centered target is less than 2% rms. A schematic of the target offset, and an example of the illumination intensity profile is shown in Figure 5-15.

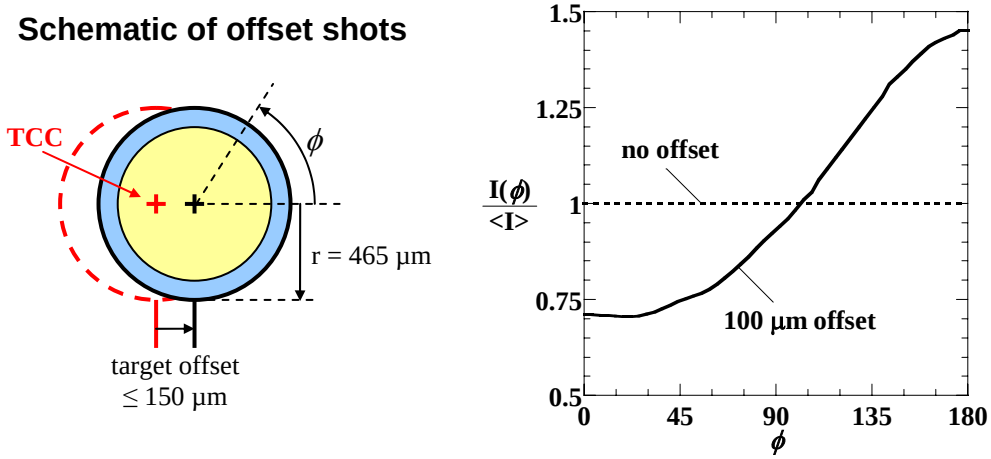

Figure 5-15: Schematic of a target offset from the target chamber center (TCC). TCC is the focal point of the laser pointing. The angle ϕ is measured with respect to the direction of offset. The graph on the right shows the intensity profile (normalized to the surface average) on the surface of a 465 μm radius capsule which was offset from TCC by 100 μm (solid line), as well as the nominal flat intensity profile for a target placed at TCC (dotted line).

The D^3He-shock yield is not significantly affected by increased radiation nonuniformity induced by offset of the target from TCC. The yield from each implosion in an offset campaign was normalized to the yield from the reference shot with no offset from the same campaign. The mean and standard error of shots with the same offset from each campaign is shown in Figure

[26] The ℓ^{th} asymmetry mode number corresponds to the set of spherical harmonics $Y_{\ell m}$, with $-\ell \le m \le \ell$, and is characterized by having a maximum of ℓ oscillations around a great circle.

5-16. The yield is not significantly degraded for offsets up to 100 μm (21% rms nonuniformity), and a nonuniformity of 32% reduced the shock yield by only 40%.

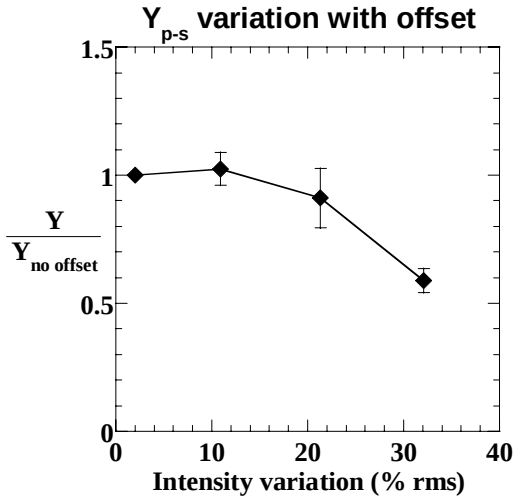

Figure 5-16: Normalized D^3He shock yield ($Y_{p\text{-}s}$) from implosions of targets which were offset from TCC, as a function of the rms intensity variation over the surface. The yields are normalized to the yields measured from centered implosions. The error bars show the standard error over four campaigns of offset shots with different shell thicknesses. No significant reduction in the yield is seen until the target is offset by 150 μm (32% rms). The rms intensity variation is predominantly in low modes (ℓ = 1-3).

Shock-bang time was also minimally affected by illumination nonuniformities induced by the target offset from TCC, as seen in Figure 5-17. The average difference in the shock-bang time of offset shots compared to shock-bang time of their corresponding centered shot is less than the shot to shot scatter in the shock-bang time.

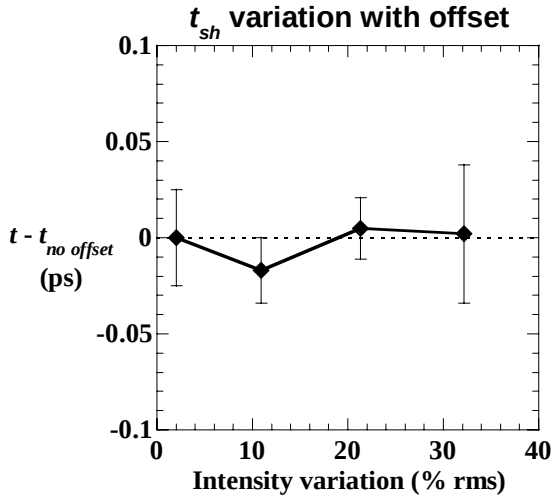

Figure 5-17: Shock-bang time of offset shots compared to shock-bang time for centered shots as a function of rms intensity variation. Points are averages and standard deviations, among shots with the same offset, of the difference of shock-bang time with the shock-bang time of the corresponding centered shot. The absolute timing variation is 25 ps, and is shown as the error bar on the centered (2% rms) data point.

To investigate the effects of high-mode drive non-uniformities on shock timing and convergence, capsules with 20 μm thick shells were shot with and without SSD laser beam

smoothing. Laser smoothing using 2-D SSD with a 1 THz bandwidth reduces the rms illumination nonuniformity in high ℓ modes (ℓ = 31-500) by a factor of 20 [37]. The resulting overall laser intensity nonuniformity is reduced from 14% without laser smoothing ("SSD off") to less than 2% rms with full beam smoothing ("SSD on").

Measurements with SSD on and off show that shock yield and timing have minimal sensitivity to high-mode irradiation non-uniformities. Turning off SSD reduced the shock yield by 8±26%, and delayed shock-bang time by 10±18 ps.

The robustness of the D^3He shock yield and shock-bang time to asymmetrically driven shocks is revealed in Figure 5-18. The shock yield ratio is plotted as a function of the shock-bang time delay as compared to the corresponding symmetric shot. Shocks driven with low-mode (ℓ = 1-3) asymmetries less than 22% rms produce the same yield and timing, whereas a 32% rms degrades the yield by a factor of two, without affecting timing. Shocks driven with high-mode (ℓ = 31-500) asymmetries of 14% rms behave the same as the corresponding symmetrically driven shot, within the error of the observations.

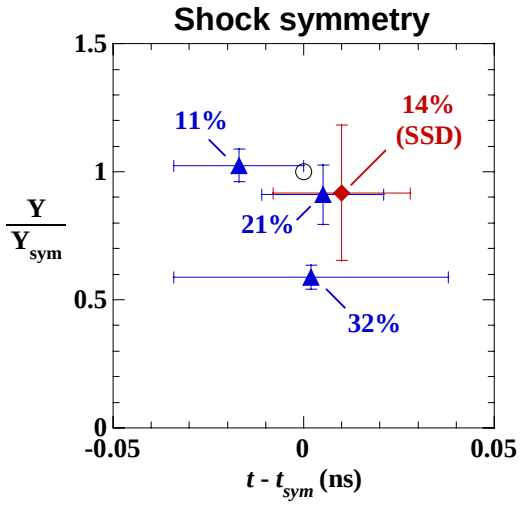

Figure 5-18: Asymmetrically driven shocks have the same yield and shock-bang time performance as symmetric shocks driven through equivalent capsules. The shock yield ratio is plotted as a function of the shock-bang time delay as compared to the corresponding symmetric shot (open circle at (0,1)). Shocks driven with low-mode (ℓ = 1-3, blue triangles) asymmetries less than 22% rms produce the same yield and timing, whereas a 32% rms degrades the yield by a factor of two, without affecting timing. Shocks driven with high-mode (ℓ = 31-500, red diamonds) asymmetries of 14% rms behave the same as the corresponding symmetrically driven shot.

5.5 Shock Summary

Measurements of shock-bang time, D^3He and DD-p shock yields, and ρR at shock time have been performed on a variety of types of capsule implosions with different CH shell thicknesses and D^3He fill pressures, and the experimental results were compared to results from 1-D hydrodynamic simulations. The experimental D^3He shock results are summarized in Table 5-1 and the experimental DD-p shock results are summarized in Table 5-2.

Table 5-1: Mean and error of measured values of shock-bang time, shock-burn duration, D^3He shock yield, and ρR at shock time, for implosions with different shell thicknesses and fill pressures. The D^3He shock yield is shown both as an absolute yield, and as a percentage of the total D^3He yield.

Pres (atm)	ΔR (μm)	Num shots	shock bang (ps)	err	shock burn (ps)	err	$Y_{p\text{-}s}$ ($\times 10^7$)	err (%)	$Y_{p\text{-}s}$ (% Y_p)	err	ρR_{sh} (mg/cm^2)	err
3.6	15	3	1233	29	108	26	-		-		-	
"	20	8	1470	16	118	16	-		-		-	
"	24	6	1585	27	129	10	0.48	8.8	10.6	0.9	9.8	0.4
"	27	4	1731	39	122	30	0.25	20.0	12.2	1.7	12.0	0.9
18	15	3	1264	29	137	26	-		-		-	
"	20	8	1506	16	146	12	3.09	7.4	6.2	0.5	8.2	1.0
"	24	9	1591	12	137	9	1.45	9.3	9.3	0.6	8.9	0.7
"	27	6	1690	11	146	8	1.44	17.8	19.8	2.5	9.4	1.2

Table 5-2: Mean and standard error of measured values of DD-p shock yield, and ρR at shock time inferred from the downshift of DD-p, for implosions with different shell thicknesses and 18 atm fill pressure. The DD-p shock yield is shown both as an absolute yield, and as a percentage of the total DD-n yield.

Pres (atm)	ΔR (μm)	Num shots	$Y_{DD\text{-}s}$ ($\times 10^7$)	err (%)	$Y_{DD\text{-}s}$ (% Y_n)	err	ρR_{sh} (mg/cm^2)	err	T_{rat} (keV)	err
18	20	3	14.1	13.1	1.2	0.2	9.3	0.6	5.9	0.4
"	24	3	9.2	19.6	1.9	0.3	10.0	0.7	5.4	0.4
"	27	2	-	-	-	-	11.1	1.0	-	

Shock-bang time was observed to occur 200 to 350 ps earlier than predicted by simulations. Experiments and simulations both saw that increasing shell thickness linearly delayed shock-bang time, but simulations predicted that lowering the fill pressure from 18 to 3.6 atm would delay shock-bang time by 100 to 150 ps, whereas experiments demonstrated that shock-bang time is independent of fill pressure. The duration of shock burn was observed to be independent of shell thickness, but to be about 20 ps seconds shorter for 3.6 atm fills compared to 18 atm fills.

LILAC simulations overestimate the D^3He and DD-p shock yields that were observed experimentally. The largest discrepancy occurs for the D^3He shock yields from implosions with 3.6 atm fills, where the simulations predict yields nearly 30 times higher than the experimental results, or a YOC of 3.5%. The YOC for implosions with 18 atm fill pressure was 5-12% for D^3He shock yield, and 7-14% for the DD-p shock yield.

The simulated shock timing and yields can be adjusted by changing the flux limiter; however, no value of the flux limiter can match both the shock timing and yield simultaneously. Simulations using the new input deck substantially improve shock results. A simulation of shot 38525 using the new input deck improves the D^3He shock YOC from 12% to 50%, and reduces the simulated shock-bang time delay from 270 ps to 230 ps.

The simultaneous measurement of yields from two different nuclear reactions at shock time allows an estimate of the ion temperature to be made. A shock temperature near 6 keV was inferred from experimental data, consistent with previously published results using a different method, and slightly lower than the shock temperature inferred using simulated shock yields.

Areal density at shock time was inferred using the downshift of two nuclear products from their birth energy: 14.7 MeV D^3He protons and 3.0 MeV DD protons. Both methods of inferring shock ρR give results near 10 mg/cm^2, with larger values of ρR for thicker shells and lower fill pressures. Simulations predict much higher ρR's at shock time: about 15 mg/cm^2 for 18 atm fills and up to 32 mg/cm^2 for 3.6 atm fills. In addition, the simulations predict that ρR will decrease with increasing shell thickness; the opposite trend was observed experimentally.

The convergence of the shock, and the nuclear production induced by the resulting expanding shock have been demonstrated to be essentially one dimensional in nature. In Chapter 4 it was shown that shock collapse and shock burn occur well before there is a substantial amount of hydrodynamic instability growth leading to turbulence and mix. And in Section 5.4, it was shown that even rather large low-mode and high-mode drive nonuniformities do not significantly perturb the shock timing or yield. This is encouraging for the potential of 1-D hydrodynamic codes to simulate converging shocks, since the more computationally intensive 2-D and 3-D models are not necessary to reproduce the essential features of nuclear production resulting from collapsed shocks.

The poor performance of the current 1-D simulations indicates that the currently included physics is not sufficient to predict shock propagation and heating. Due to the importance of shock timing and heating to the success of ignition in ICF, it is likely worthwhile to reexamine the treatment of shocks in current hydrodynamic codes.

6 Modeling Shock Burn

Reliable prediction of shock dynamics is of critical importance for the design of ignition capsules in inertial confinement fusion (ICF). The significant discrepancy between experiments and 1-D simulations of the shock yield and timing results reported in Chapter 5 is of great concern for the accuracy of numerical code predictions of shock timing and heating. The demonstration of the inherent 1-D nature of the shock convergence in ICF implosions establishes that expensive 2-D or 3-D models are not necessary to predict its behavior. This chapter uses a quasi-analytic 1-D model of shock convergence to help elucidate the origination of the differences between experiments and simulations.

The dynamics of a strong imploding spherical shock front was first investigated by Guderley [77] using a self-similar form of the fluid equations. This analysis was extended in numerous works, including those of Lazarus [78] and Hafner [79], and has been reviewed in a number of books, including Zel'dovich and Raizer [21] and Atzeni and Meyer-ter-Vehn [19].

In direct-drive ICF implosions, the rise of the laser pulse launches a strong imploding spherical shock, which can induce nuclear burn after it collapses at the center. Goldman [80] previously compared neutron yields from a Guderley analysis to numerical simulations. Brueckner and Jorna [16] and Haubold and John [81] calculated analytic approximations to the yields. In this chapter, we will compute the time-dependent DD-n and D^3He nuclear production histories using the Guderley analysis, and compare these results to measured and simulated nuclear production histories.

Section 6.1 reviews the Guderley model of a collapsing shock, and Section 6.2 describes a method to estimate the absolute timing of shock collapse using a simple extension to Guderley's model. Section 6.3 gives the nuclear yield and burn history results obtained by calculating nuclear burn using Guderley profiles with scales relevant to ICF. Section 6.4 compares the burn histories obtained with the Guderley model to burn histories measured experimentally and calculated numerically. Section 6.5 discusses the results of the comparison, and suggests possible improvements to the model. A summary is included in Section 6.6.

6.1 The Guderley model of a collapsing shock

In 1942, Guderley [77] considered the behavior of strong spherical and cylindrical shocks near the center or axis of collapse by treating the dynamics of the shock-perturbed fluid as a self-similar system. As the converging shock approaches the center of collapse, it decouples from its generating boundary, and thus loses "memory" of the details of its formation. The legacy of the shock's creation is only a single number corresponding to its strength. The loss of the reference length and time scale which produced the shock compels the resulting flow to assume a self-similar form.

A self-similar (or "scale-invariant") system has the property that its "shape" is identical at any time or length scale, provided the other dimension is scaled appropriately. For example, by changing the time scale by a factor of c, so that $t' = c\,t$, the system will retain its shape if the length is scaled as $r' = c^{\alpha}\,r$, where α is the self-similarity index.

An important property of scale-invariant flows is that flow variables can be represented as functions with just a single self-similar coordinate, instead of complex multi-argument functions of both space and time. For example, the velocity u, mass density ρ, and pressure P – normally expressed as functions of space and time (r and t) – can be expressed as functions of just the single self-similar coordinate x:

$$\begin{aligned} u(r,t) &= u_0 \; f_u(x), \\ \rho(r,t) &= \rho_0 \; f_\rho(x), \\ P(r,t) &= \rho_0 \, u_0^2 \; f_P(x), \end{aligned} \tag{6-1}$$

where u_0 and ρ_0 are the reference speed and density, and f_u, f_ρ, and f_P are the self-similar functions for velocity, density, and pressure. For the collapsing shock problem, it is convenient to express the coordinate x as a function of radius and time like:

$$x(r,t) = \frac{1}{\xi_0} \frac{r}{\left| t - t_c \right|^\alpha}, \tag{6-2}$$

where t_c is the instant of collapse, and ξ_0 is the shock strength parameter, which is a constant whose value is reduced from the strength of the shock that formed.

The inherent advantage of the self-similar treatment is that the fluid system of partial differential equations can be reduced to a set of self-similar ordinary differential equations. The ordinary differential equation system is less computationally intensive to solve, and produces a simpler solution, which depends on only a single coordinate.

Let's consider the case of a strong spherical shock converging into a cold, uniform, ideal gas at rest. When the shock approaches the center of collapse, it will have decoupled from its generating boundary, and will follow a self-similar trajectory given by:

$$r_s(t) = \xi_0 \left| t - t_c \right|^\alpha, \tag{6-3}$$

where r_s is the radial position of the shock front at time t; notice that the scale has been chosen such that the initial ingoing shock has the self similar coordinate position $x = 1$. The shock front represents the boundary condition, and the self-similar fluid equations are integrated starting from the following strong shock jump condition:

$$\begin{aligned} u_1 &= \frac{2}{\gamma - 1} u_s, \\ \rho_1 &= \rho_0 \frac{\gamma + 1}{\gamma - 1}, \\ P_1 &= \frac{2}{\gamma - 1} \rho_0 \, u_s^2, \end{aligned} \tag{6-4}$$

where subscripts 0 and 1 denote the flow parameters just upstream and just downstream of the shock front, respectively. Here, γ is the adiabatic index, and u_s is the shock speed at time t:

$$u_s = \frac{dr_s}{dt} = \xi_0 \alpha \left| t - t_c \right|^{\alpha - 1}. \tag{6-5}$$

Integration of the reduced, self-similar fluid equations from the boundary condition given by Equations (6-4) to the shock collapse at the center is only possible for a single value of α. This unique value is determined by the adiabatic index γ, and in general must be calculated numerically. For spherical collapse in an ideal monatomic gas ($\gamma = 5/3$), characteristic of the fill gas after the shock, $\alpha \approx 0.68838$.

At the moment of collapse, the shock reflects from the center to create a new, outgoing shock. This outgoing shock will have the same self-similarity index, but a lower shock strength parameter, since it is now traveling through an inward-moving fluid. For a gas with $\gamma = 5/3$, the outgoing shock strength parameter ξ_2 takes the value $0.740\xi_0$. Figure 6-1 shows the shock trajectory and particle streamlines in the Guderley solution.

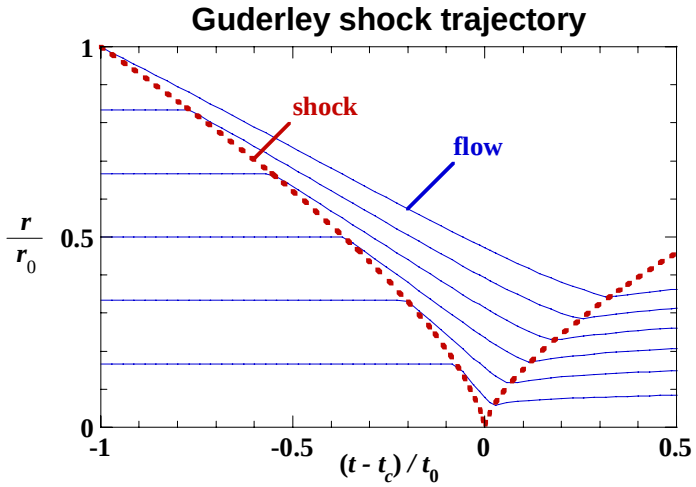

Figure 6-1: Shock trajectory and particle streamlines in the Guderley solution. This plot is analogous to the region near $r = 0$ and $t = 1.7$ ns in Figure 5-3.

A full description of the setup and solution of the Guderley model can be found in, for example, Atzeni and Meyer-ter-Vehn [19]. The result of the analysis is a tabular solution of the self-similar flow variable functions f_u, f_ρ, and f_P. The temperature T is calculated from the density and pressure using the ideal gas law, $T = mP/\rho$, where m is the average particle mass.

The resulting solution curves for the mass density (ρ/ρ_0) and temperature ($T / m\, u_0^2$) are plotted in Figure 6-2 as a function of the radial position (r/r_0) at times before and after shock collapse. The times were chosen to be the same time t_0 before and after the instant of collapse t_c. The radial position has been normalized to the radius r_0 corresponding to the position of the shock at time $t_c - t_0$, the density has been normalized to the initial density ρ_0, and the temperature has been normalized using the average particle mass m, and the shock speed u_0 at time $t_c - t_0$.

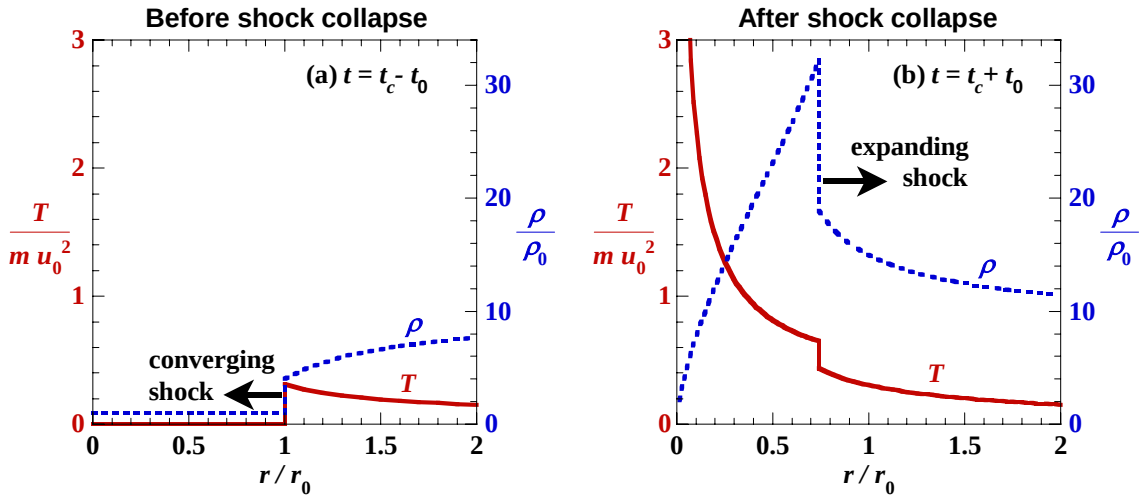

Figure 6-2: Normalized temperature (solid red) and density (dotted blue) profiles in the Guderley solution with $\gamma = 5/3$, (a) before shock collapse, where the shock is moving inwards and (b) after shock collapse, where the shock is moving outwards.

Some interesting characteristics of the Guderley flow with $\gamma = 5/3$ are that before the instant of collapse, the density jumps from ρ_0 to $4.0\rho_0$ at the shock front, and increases toward $9.5\rho_0$ at large radii. At the instant of shock collapse, the flow has a uniform density of $9.5\rho_0$, and the temperature and pressure diverge near the center. The reflected shock increases the density to a maximum of $32.3\rho_0$, and the temperature diverges and the density vanishes near the center in such a way that the pressure is nearly isobaric.

6.2 Shock collapse time

In ICF, the shock must propagate through at least two distinct regions, corresponding to the solid shell and the gaseous fuel. The large density difference between these regions has a significant impact on the propagation of the shock. Since Guderley considered a problem with no interfaces, we must add to this model a treatment of the shock propagation through the shell, and understand how the shock is transmitted into the fuel.

Working backwards from the time of shock collapse, and using r_0 as the initial inner boundary of the shell, the time it takes for the shock to propagate from r_0 to the center of collapse is:

$$t_c - t_b = (r_0 / \xi_0)^{1/\alpha}, \tag{6-6}$$

where t_b is the moment of shock breakout, when the shock first emerges from the shell into the fuel, and is at position r_0. At this time, the shock speed can be calculated from Equations (6-5) and (6-6):

$$u_0 = \alpha\, r_0 (r_0 / \xi_0)^{-1/\alpha}. \tag{6-7}$$

A shock of speed u_0 in the fuel is transmitted through the fuel-shell interface by a shock of speed u_1 in the shell. The ratio of the shock speed in the fuel to the shock speed in the shell is $R_{us} = u_0/u_1$, which can be easily calculated assuming the density ratio and γ in each material are

known [22]. For the situations under consideration here, R_{us} takes on values of 2.41 and 2.67 for high and low fill pressures, respectively[27]. This initial shock is assumed to propagate at constant speed through the entire shell, of thickness Δr, where $\Delta r/r_0$ is of order 1/20. The transit time of the shock through the shell is expressed as:

$$t_b - t_{rise} = \Delta r / u_1, \tag{6-8}$$

where t_{rise} is the time that the laser rises to full power. For 1-ns pulses on OMEGA, t_{rise} is about 100 ps. Defining $t = 0$ at the "laser on" event, the time of shock collapse is:

$$\begin{aligned} t_c &= t_{rise} + \Delta r / u_1 + (r_0 / \xi_0)^{1/\alpha} \\ &= t_{rise} + \left[1 + \frac{R_{us}}{\alpha}\frac{\Delta r}{r_0}\right]\left(\frac{r_0}{\xi_0}\right)^{1/\alpha}. \end{aligned} \tag{6-9}$$

This calculation of the time of shock collapse ignores a number of physical processes that affect the speed, strength, and timing of the shock, the most important of which is the formation and coalescence of the second shock. However, Equation (6-9) gives a reasonable approximation, and has the advantage of much greater simplicity.

6.3 Burn history results of the Guderley model

In order to calculate nuclear burn histories from Guderley's model, a choice of scale must first be made, since the model is scale-invariant. A choice of three values is sufficient to set real physical scales, for example: of distance, time, and density. Here, we choose the density scale ρ_0 to be the initial density of the cold gas in the target (before implosion), which is 3.6 or 18 atm of D^3He gas at 293 K, giving $\rho_0 = 0.0005$ or 0.0025 g/cm^3, respectively. The distance is chosen as the typical initial inner radius of the target, r_0 = 410 μm. The shock strength parameter ξ_0 is chosen as the final value to set the scale of the problem, from which the time scale $t_0 = (r_0 / \xi_0)^{1/\alpha}$ can be determined. ξ_0 is chosen to best fit the experimental shock-bang time.

With the choice of scale ρ_0, r_0, and ξ_0, and the temperature and density profiles from Section 6.1, the DD-p, DD-n, and D^3He nuclear production rates can be determined using the fusion reactivities from Bosch and Hale [23] and integrating over radius:

$$\begin{aligned} \frac{dN_{DD}}{dt} &= \int_0^{r_0} \frac{\pi}{2A^2 m_p^{\,2}} \rho^2 \, \langle \sigma v \rangle_{DD} \, r^2 dr, \\ \frac{dN_{D3He}}{dt} &= \int_0^{r_0} \frac{\pi}{A^2 m_p^{\,2}} \rho^2 \, \langle \sigma v \rangle_{D3He} \, r^2 dr, \end{aligned} \tag{6-10}$$

where m_p is the proton mass, A is the average ion atomic mass number, equal to 2.5 for an equimolar mixture of D and ^{3}He, and $\langle \sigma v \rangle$ is the local thermal reactivity averaged over a Maxwellian ion velocity distribution with temperature T. The DD-p or DD-n branches can be calculated by appropriate choice of $\langle \sigma v \rangle_{DD}$. The additional factor of 1/2 in the DD reaction rate accounts for the double-counting of identical reactants.

[27] Assuming $\gamma = 5/3$ in the gas, and $\gamma = 1.5$ in the shell. If $\gamma = 5/3$ in the shell is assumed, R_{us} decreases by about 5%.

The Guderley model is a one-fluid model, but of course ions and electrons will be heated differently by the shock (see Section 5.1 and Reference [21]). The e-i thermal equilibration time scale in the fuel during shock burn is comparable to the duration of shock, so it will be important to consider e-i coupling in order to calculate the proper yields. Once the ion and electron temperatures equilibrate, the final temperature is determined using the ideal gas law for a fully ionized plasma:

$$T = \frac{Am_p}{1+Z}\frac{P}{\rho} \tag{6-11}$$

where Z is the average atomic number. This temperature represents a lower bound on the ion temperature used to calculate the nuclear production rate. An upper bound can be calculated by setting $Z = 0$ in Equation (6-11), which represents the temperature reached by the ions if there was no coupling to the electrons. These full-coupling (low T) and no-coupling (high T) limits will be used to illustrate the full range of yields that are allowed by the Guderley model.

To take into account the fact that no nuclear production occurs outside the imploding shell, the radial integration is actually performed out to the position of the fuel-shell interface, which is approximated as the position of the fluid element that encountered the shock front located at position r_0 (see the outermost particle streamline in Figure 6-1). This modified boundary condition has a very small effect on the nuclear reaction rate, since the nuclear production is dominated by the hot central regions.

Figure 6-3 shows the D^3He and DD-n nuclear reaction histories computed using the Guderley model with $\rho_0 = 0.0025$ g/cm^3, $r_0 = 410$ μm, $\xi_0 = 350$ μm/ns$^\alpha$, and no e-i thermal coupling. The majority of nuclear production occurs in the region just inside of the outgoing reshock, where both the temperature and density are very high. Very little nuclear production occurs before the instant of shock collapse, since it is before the creation of the second shock, which drives much of the nuclear yield. As the outgoing shock expands, the gas behind it cools, and the reaction rate drops. Since the D^3He thermal reactivity has stronger temperature dependence, the D^3He reaction rate drops much more rapidly that of DD-n.

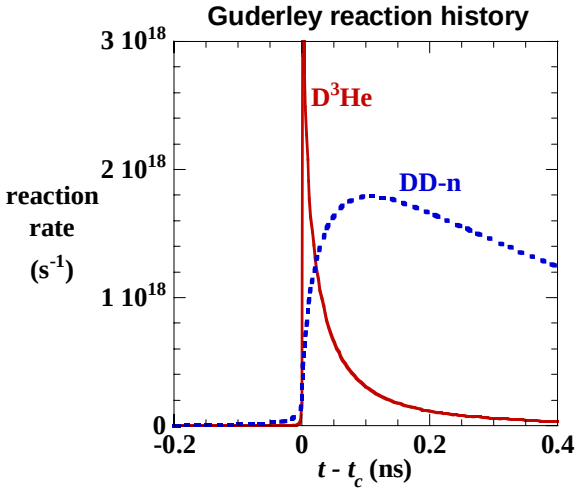

Figure 6-3: D^3He and DD-n production histories in a D^3He gas, using the Guderley model with $\rho_0 = 0.0025$ g/cm^3, $r_0 = 410$ μm, $\xi_0 = 350$ μm/ns$^\alpha$, and no e-i thermal coupling. The majority of D^3He nuclear production occurs shortly after the time of shock collapse.

Figure 6-4 shows the D^3He and DD-n yield in an 18 atm D^3He gas in the Guderley model as a function of ξ_0 for both the no-coupling and full-coupling limits. The yield limits for 3.6 atm D^3He fuel are exactly 25 times lower than the results for 18 atm, for all values of ξ_0. The yield is calculated by integrating the reaction rate out to the time that the fluid element that was first shocked at r_0 encounters the outgoing shock. This element flows inward at nearly a free-fall velocity, and is used as a substitute for the fuel-shell interface. Deceleration phase onset, and thus the beginning of the compression burn, will begin at approximately the time this element encounters the outgoing shock. Because laser ablation accelerates the shell to implosion velocities higher than reached by the initial shock impulse, the actual fuel-shell interface will most likely encounter the shock at an earlier time.

The shock collapse time as calculated by Equation (6-9) is plotted as a function of ξ_0 in an 18 atm D^3He gas in Figure 6-5. This calculation assumes a shell thickness of 24 μm, a 100 ps rise time, and a shock speed transmission ratio $R_{us} = 2.41$.

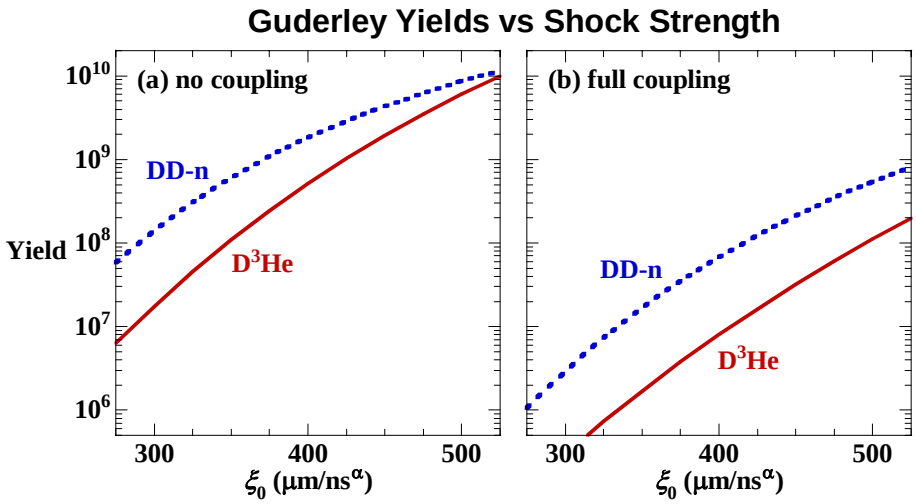

Figure 6-4: DD-n and D^3He yield dependence on the shock strength parameter ξ_0 in the Guderley model, with (a) no e-i thermal coupling, and with (b) full e-i thermal coupling.

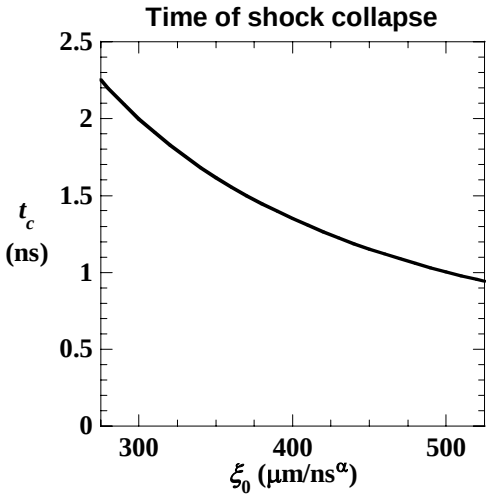

Figure 6-5: The time of shock collapse as a function of the shock strength parameter ξ_0 in capsules with a 24 μm thick capsule filled with 18 atm of D^3He.

6.4 Comparison of the model to simulation and experiment

Direct-drive implosions were conducted at OMEGA [30], with 60 beams of frequency-tripled (351 nm) UV light in a 1-ns square pulse and a total energy of 23 kJ. SG4 phase plates [36], and 1 THz bandwidth smoothing by spectral dispersion of the laser beam were used [37]. The beam-to-beam energy imbalance was typically between 2 and 4% rms. The spherical capsules had diameters between 860 and 880 μm, plastic shell thicknesses of 20, 24, or 27 μm, and a flash coating of about 0.1 μm of Aluminum. The capsules were filled with an equimolar (by atom) mixture of D_2 and ^3He with a total fill pressure of 3.6 or 18 atm. This set of experiments is the same as that examined in Chapter 5.

Diagnostics for this study were the proton and neutron temporal diagnostics (PTD and NTD) [54][52], to measure the D^3He and DD-n reaction histories; multiple wedge-range-filter (WRF) spectrometers [42], to measure the D^3He proton yield and spectrum; and the magnet-based charged-particle spectrometer (CPS-2) [42], to measure the DD protons emitted at shock-bang time (see Section 2.6).

Simulations were performed with the one dimensional radiation-hydrodynamic code LILAC [31], with a flux limiter $f = 0.06$. A selection of shots for each type of experimental setup described above was simulated using the "old" input deck. Shot 38525 was also simulated using a "new" input deck, with improved treatment of laser absorption, which has important consequences for these shock convergence studies. This new input deck was developed after the experiments were performed, and after this Guderley comparison was first presented.

The D^3He burn history calculated using the Guderley model is very peaked at the instant of shock collapse. In order to compare this history to the experimental D^3He reaction history, the Guderley burn history is broadened by convolving it with a Gaussian point-response-function with $\sigma = 25$ ps, the instrumental response of the proton temporal diagnostic (PTD). In addition, the DD-n burn history is similarly broadened, but with $\sigma = 40$ ps. Figure 6-6 shows the results of these convolutions.

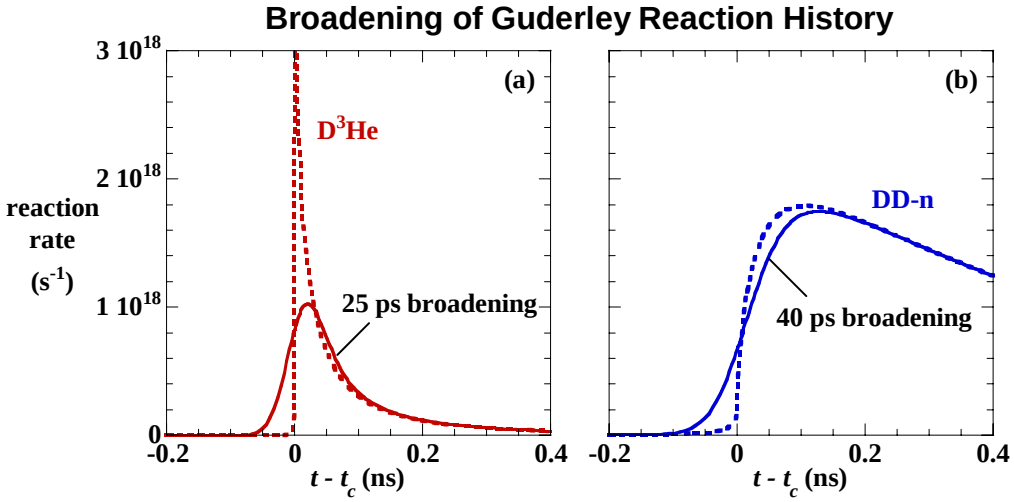

Figure 6-6: (a) D^3He and (b) DD-n production histories in the Guderley model. The dotted curves are the Guderley histories shown in Figure 6-3, and the solid curves represent the Guderley histories "broadened" with a Gaussian point-response-function to mimic the instrumental broadening of the PTD (25 ps) and the NTD (40 ps). The DD-n and DD-p reaction histories are nearly identical.

The shock strength parameter ξ_0 that best matches experiment is chosen so that the broadened Guderley shock burn history has a shock-bang time which best matches the experimental shock-bang time. The experimental shock yield should fall in between the high and low temperature limits of the Guderley model with the best-matched choice of ξ_0. Figure 6-7 compares the experimental D^3He production history of shot 38525 with the best-matched Guderley model with no thermal coupling. Also shown is the trajectory of the shock. The Guderley history with no coupling results in a shock yield about 6 times higher than experiment, and with full coupling, is about 7 times lower. In this example, the experimental shock-burn duration is about 60 ps longer than the Guderley shock burn duration (with no coupling).

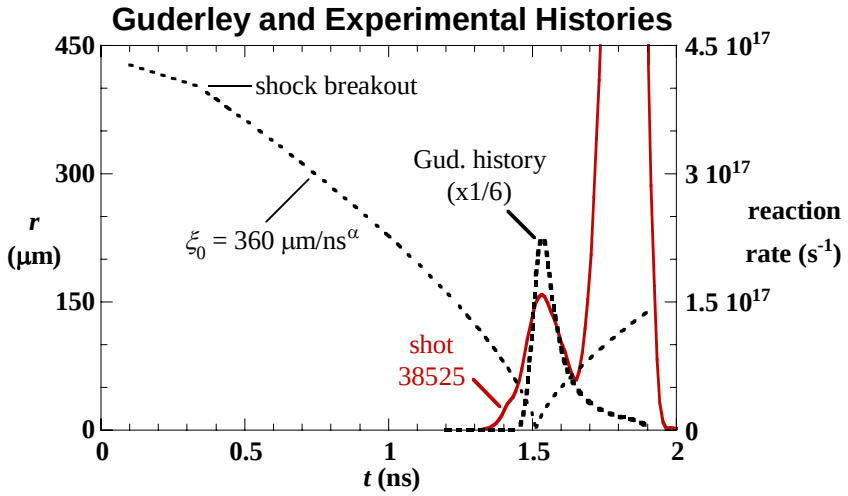

Figure 6-7: Comparison of the Guderley model with $\xi_0 = 360$ μm/ns$^\alpha$ and the experimental D^3He burn history of shot 38525, which had a 24 μm thick CH capsule with 18 atm D^3He fill. The time of collapse for the Guderley model (with no coupling) was chosen to best match the experimental D^3He shock bang time. The rise in the experimental burn history at 1.7 ns is the start of the compression burn.

The value of ξ_0 that best matches a simulation is chosen in a different fashion than the experimental best fit. The shock trajectory can be extracted directly from the simulation, and so a Guderley shock is chosen with a ξ_0 and t_c that best match the final converging trajectory of the simulated shock. Because the simulated shock trajectory includes shock dynamics which are neglected in the simple extended Guderley model, such as the rarefaction, 2nd shock formation and shock coalescence, the earliest time of the fit is taken to be shock coalescence time. Since the simulation can't track the shock inside the outer boundary of the innermost zone, the fit extends up to the time the shock encounters this boundary.

Figure 6-8 compares the simulated D^3He production history and shock trajectory of shot 38525 with the best-matched Guderley model using no thermal coupling. Immediately evident is the fact that the final simulated shock trajectory is well-fit by a Guderley shock trajectory. However, the best fit ξ_0 to the simulation is much higher than the experimental best fit (445 vs. 360 μm/ns$^\alpha$), even though shock-bang time occurs later than in the experiment. A best fit to the simulation using the fitting method used for the experimental results gives $\xi_0 = 319$ μm/ns$^\alpha$. The coalescence of two shocks seen in the simulations allows for very strong final shock strengths, while still allowing shock collapse time to occur later.

As with the experimental shock yield, the simulated shock yield should fall in between the high and low temperature limits of the Guderley model with the best-matched choice of ξ_0. The

Guderley history with no coupling results in a D^3He shock yield about 13 times higher than simulation, and with full coupling, is about 4 times lower. A best fit to the simulation using the experimental fitting method would place the simulated D^3He shock yield above the upper *T* limit.

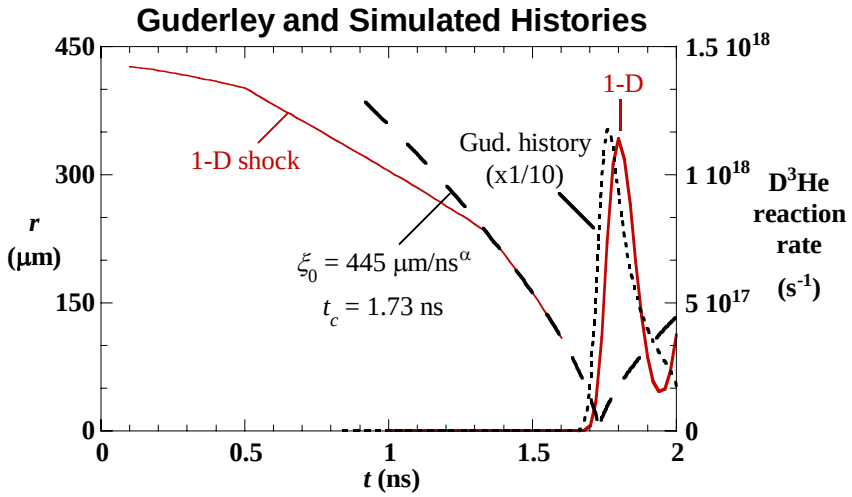

Figure 6-8: Comparison of the Guderley model and a 1-D simulation of shot 38525, which had a 24 μm thick CH capsule with 18 atm D^3He fill. The best fit of a Guderley self-similar shock to the 1-D shock trajectory after shock coalescence gives ξ_0 = 445 μm/ns$^\alpha$ and t_c = 1.73 ns.

Figure 6-9 shows the D^3He and DD-p shock yields as a function of ξ_0 for experiments, simulations, and the Guderley model. ξ_0 for experiments and simulations was determined as described above, and the points shown are the results of the average of many shots with 20, 24, and 27 μm thick shells filled with 18 atm D^3He.

The experimental and simulated shock yields always fall within the upper and lower *T* limit curves of the Guderley model. The decreasing experimental best-fit ξ_0 and yields for thicker shells results in experimental points distributed along a curve with about the same thermal coupling ratio between the full and no coupling curves. Simulations predict very little change in the shock strength with shell thickness, but the decreasing yields indicate that thermal coupling is stronger for thicker shells.

Simulations predict much higher shock strengths than the best fit ξ_0 to the experiments. In fact, the shock strength is so high that the lower *T* limit yield is above the experimental yields for all shell thicknesses, and for both D^3He and DD-p yields. Looked at another way, the highest value of ξ_0 consistent with the experimental yields (according to the model) is lower than the value of ξ_0 predicted by the simulations.

Figure 6-10 shows a similar plot as Figure 6-9, but for a fuel density corresponding to a fill pressure of 3.6 atm of D^3He. The experimental values are much closer to the no-coupling upper *T* limit of the Guderley yield curve, because the thermal equilibration time is much longer for these low pressure fills. The 1-D simulations also fall close to the upper *T* limit curve, and for the case of the 20 μm thick target, even falls above it. The high yields in the simulations compared to the Guderley yields are partly due to additional heating of the fuel from a reverberation shock that reflects off the imploding shell (see Subsection 5.3.1).

Unlike the case of high fill pressures, the shock strength predicted by simulations falls within the range of ξ_0's that are consistent with the experimental yields. Curiously, though, the best fit of ξ_0 to simulations has a strong dependence on shell thickness for targets with low pressure, in contrast to the weak dependence on shell thickness for targets with high fill pressure.

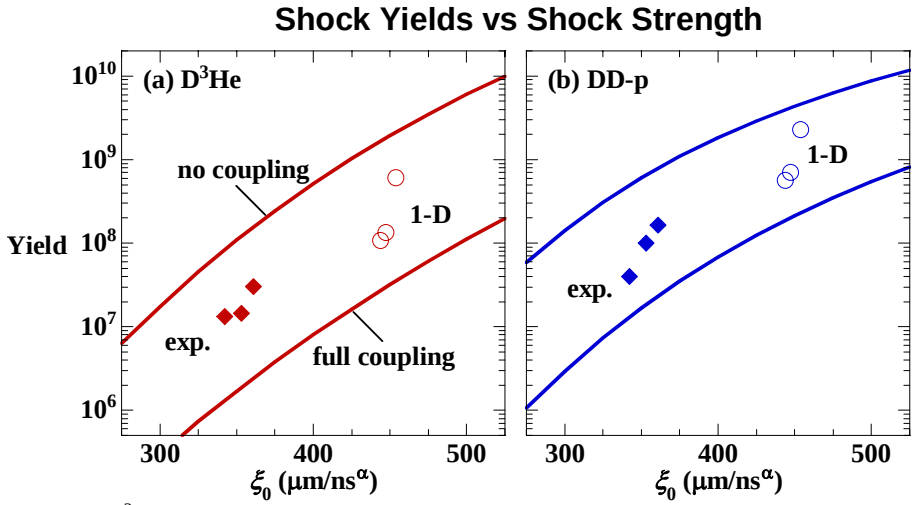

Figure 6-9: (a) D^3He and (b) DD-p shock yields derived using the Guderley model with full and no e-i thermal coupling (lower and upper solid lines). Also shown are the experimental (solid diamonds) and 1-D simulated (open circles) values for high pressure fills of 20, 24, and 27 μm thick targets (thicker shells have lower ξ_0). The standard error on both yield and ξ_0 for experimental points is about the marker size.

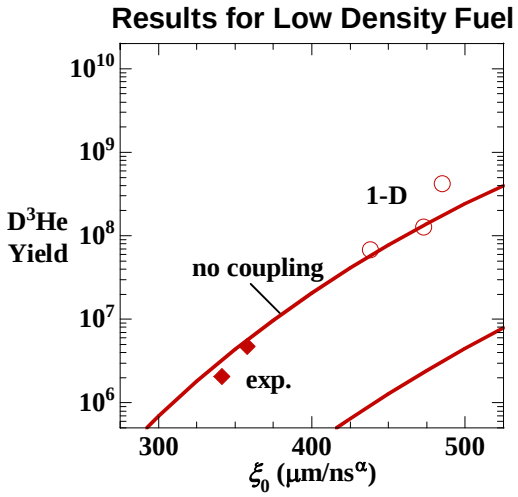

Figure 6-10: D^3He shock yields derived using the Guderley model with low fuel density and with full and no e-i thermal coupling (lower and upper solid lines). Also shown are the experimental (solid diamonds) and 1-D simulated (open circles) values for low pressure fills of 20 (1-D only), 24, and 27 μm thick targets, where thicker shells correspond to lower yields and ξ_0. The experimental values are much closer to the no-coupling Guderley yield curve than for high fuel density, because the thermal equilibration time is much longer for these low pressure fills.

6.5 Discussion

Experimental data fit well within the limits imposed by the no-coupling and full-coupling extremes of the Guderley model, but as currently formulated, the estimation of the Guderley time of collapse is fit to the experiments by choice of the free parameter ξ_0. A similar model could be turned into a predictive model if a suitable treatment of the shock generation, rarefaction, and coalescence could be formulated such that ξ_0 could be calculated from experimental shot parameters. The result of this treatment would tend to increase the estimate of the best guess for the shock strength parameter of the final collapsing shock.

Tighter constraints than the high-T and low-T limits could be achieved using a simple treatment of the e-i thermal equilibration within the Guderley model. This could be accomplished without perturbing the dynamics of the Guderley model, since the exchange of energy between electrons and ions will not otherwise affect the implosion dynamics, as the total pressure will be the same no matter what temperature ratio is used.

A simple thermal coupling relation can be found in numerous references, such as in Zel'dovich and Raizer [21], which typically assumes the rate of thermal equilibration is linearly related to the temperature difference, over the electron-ion equilibration time constant:

$$\frac{dT_i}{dt} = \frac{T_i - T_e}{\tau_{eq}}. \tag{6-12}$$

The temperature relation is closed by constraining the sum of the temperatures:

$$T_i + ZT_e = const = T_0, \tag{6-13}$$

where $T_0 = Am_pP/\rho$ is the initial ion temperature (just after the shock front). The electron-ion thermal coupling time constant τ_{eq} is given by:

$$\frac{\tau_{eq}}{\tau_0} = \left(\frac{T_e}{m_i u_0^2}\right)^{3/2} \left(\frac{\rho}{\rho_0}\right)^{-1}, \tag{6-14}$$

$$\tau_0 = \frac{3}{8\sqrt{2\pi}} \left(\frac{4\pi\varepsilon_0}{e^2}\right)^2 \frac{m_i^2}{Z^3 m_e^{1/2} \ln\Lambda} \frac{(m_i u_0^2)^{3/2}}{\rho_0}. \tag{6-15}$$

where τ_0 is a normalization constant, and u_0 is the local speed of the shock front as it passed.

Examination of the assumptions of the Guderley model turns up more features that could be improved. Assumptions that are very good are that the shock collapse is 1-D in nature; the EOS of the fuel is an ideal gas with $\gamma = 5/3$; the gas is initially cold, uniform, and stationary; the nuclear production does not affect the hydrodynamics; and that the problem is self-similar near the center of collapse. Two essential assumptions of the Guderley model that are most likely violated in the collapse of shocks in these situations are that there is no thermal conduction, and that the fluid is highly collisional.

Thermal conduction is an important effect to consider during the shock burn, due to the relatively high temperatures and steep temperature gradients that occur in the fuel at that time.

Reinicke and Meyer-ter-Vehn [82] considered a self-similar hydrodynamic problem that included heat conduction that could likely be adapted to the Guderley converging shock analysis. The most important effect of thermal conduction would be to smooth out the temperature singularity at the center of collapse after the time of collapse, which would reduce the yield for a given shock strength.

The fluid approximation holds best when the collisional mean-free-path of constituent particles is much smaller than the scale size of the system, and when the collision time is much shorter than the time scales of interest. The high temperatures and low densities characteristic of the fuel during shock burn (~6 keV, ~0.1 g/cc) lead to mean-free-paths that are about the same size as the plasma (~100 μm). The breakdown of the fluid assumption for plasmas that are not highly collisional has a number of important consequences.

The most fundamental consequence of a breakdown in the fluid approximation is, of course, that the dynamics of the system may deviate from that expected based on the fluid equations. The distribution of particle velocities will most likely not have the Maxwellian form that is assumed for a fluid, due to the non-locality of the constituent particles, as well as the convergence of the fuel at speeds comparable to the typical ion thermal speed. The non-Maxwellian velocity distribution necessitates a kinetic treatment, which complicates the calculation of flow variables such as pressure and temperature. In particular, the thermal reactivities used to calculate the nuclear production rate assumes a Maxwellian velocity distribution, and any deviation will tend to change the predicted yields.

The strength of the shock reflected from the center may differ from that of an ideal fluid if the fuel is not highly collisional. When the shock gets very close to the center of collapse, very few particles will be left that make up the “shock front”, so the shock may pass through the center without a hard reflection. The resulting outgoing shock may therefore be weaker than would occur in the ideal fluid picture.

It may be surprising that a shock could be sustained at all in a plasma with such low collisionality, but collisionless shocks have been observed in many astrophysical and laboratory systems, and are mediated by collective electromagnetic interactions. In the absence of an ambient magnetic field, streaming plasma instabilities lead to the formation of an electric potential at the boundary of the flow regions, and the resulting collisionless shock front is known as an electrostatic shock [83]. The essential behavior of an electrostatic shock is the same as a shock mediated through collisions, but the details of its propagation can not be fully treated with a fluid system.

It should be emphasized that these limitations of the fluid approximation also apply to LILAC simulations, since LILAC is also based on the fluid equations. Although LILAC includes thermal conduction terms, it may not calculate its effects correctly during the shock burn, since the temperature gradients are shorter than the mean-free-path at that time.

In light of these limitations of the fluid approximation in the fuel during shock burn, it is remarkable how well the Guderley analysis and the LILAC simulations can model the observed shock burn. Although the suggestions outlined above would improve the constraints imposed by the Guderley analysis, and the fluid simulations could also benefit from modifications to take into account limitations of the fluid assumption, a kinetic treatment may be necessary to more fully reproduce the shock-induced nuclear production observed experimentally.

6.6 Shock Model Summary

A 1-D model of shock convergence was constructed based on the Guderley self-similar converging shock problem. Density and temperature profiles from Guderley's solution were used to calculate D^3He and DD nuclear production histories. A simple extension to the Guderley analysis was added in order to obtain absolute timing of the modeled nuclear production histories.

A one-parameter fit of this model to experimental data from a given shot gives a shock-bang time and shock-burn duration in reasonable agreement with experiment, and bounds the experimental D^3He and DD-p yields. The model was used to determine that stronger shocks are formed in implosions of capsules with thicker shells, and to demonstrate that the e-i thermal coupling at shock-bang time is weaker in implosions of capsules with lower fill pressure.

A two-parameter fit of this model to simulated data from a given shot also produces a reasonable shock-bang time and shock-burn duration, and can bound most of the simulated D^3He and DD-p yields. The model was used to determine that simulations calculate final shock strengths that are nearly independent of shell thickness for high pressure fills, and depend strongly on shell thickness for low pressure fills. The simulated shock strengths were much higher than the best fit to the experiment, and in fact for high-pressure capsules, the simulated shock strength is above the upper limit on shock strength consistent with the experimental yields.

An exception to the limits placed on yields by the model was found in simulations of 20 and 27 μm thick capsules filled with 3.6 atm D^3He, where the simulated yield was over twice as large as the upper limit imposed by the model. These simulated yields exceed the limits of the model due in part to additional heating of the fuel from a reverberation of the shock in the fuel caused by a reflection from the imploding shell, however, no experimental evidence for this shock reflection was observed (see Section 5.3).

This model shows promise in reproducing the essential characteristics of shock collapse and the resulting nuclear production, and several possibilities to improve its effectiveness, tighten its limits, and enable predictive capabilities have been suggested. However, limitations of the model due to the fluid approximation may ultimately lead to the need for a kinetic representation of shock collapse.

7 Summary

Spectral and temporal nuclear diagnostics were used to measure yields, areal densities, ion temperatures, and bang times for a variety of directly-driven implosions of plastic capsules filled with D_2 and ^{3}He gas at the OMEGA laser facility. These experiments were performed to investigate the hydrodynamic equivalence of D_2 and ^{3}He mixtures, the time-dependent dynamics of turbulent mix between the fuel and the shell, and the timing of and yields produced by the collapse of converging spherical shocks. In addition, a self-similar quasi-analytic model was developed to gain insight into the behavior of collapsing shocks, and to evaluate the ability of 1-D fluid codes to model their behavior.

Hydrodynamically-equivalent fuels with different ratios of D_2 and ^{3}He can be chosen to have the same mass density, total particle density and equation of state. The implosion of capsules filled with these fuels resulted in DD-n and D^{3}He bang times that were independent of the fuel composition, confirming the hydro-equivalence. However, implosions with a 50-50 mixture of D:^{3}He by atom consistently resulted in measured nuclear yields half of that anticipated by scaling from measured yields of implosions with pure D_2 and nearly pure ^{3}He. This observation is seen over a wide range of experimental configurations, including targets with a variety of shell thicknesses and fill pressures, simultaneously for two different nuclear yields (DD and D^{3}He), as well as for shock and compression yields. A number of possible mechanisms to cause this unexpected experimental scaling have been considered, but no dominant mechanism has been identified.

The extent and evolution of turbulent fuel-shell mix was investigated using special targets with a 1 μm layer of CD at the inner surface, or offset by 1 μm from the inner surface of a 20 μm thick shell and filled with a gas of pure ^{3}He. Production of D^{3}He protons requires atomic mixing between the fuel and shell, and measurements of these protons were used to determine the timing and extent of mix. Important features of the mix experiments were immediately evident: first, that the fuel and shell become atomically mixed, even to the extent that the fuel mixes with shell material from the second micron of the original configuration. Second, that susceptibility to instability growth and mix is reduced by increasing the initial fill pressure. Third, the D^{3}He shock burn – always present for gas fills of D^{3}He – was absent, enabling a strong limit to be set on the extent of D penetration into the ^{3}He. And fourth, the time necessary for RT instabilities to induce mix resulted in a 90 ps delay in the D^{3}He bang time as compared to bang time for implosions with D^{3}He fills.

The onset of the laser pulse launches a convergent shock into the capsule, collapsing at the center and inducing nuclear production several hundred ps before deceleration and stagnation of the imploding shell. The time and duration, as well as the D^{3}He and DD-p yields, the mean ion temperature, and the capsule ρR for this shock burn were measured and compared to 1-D simulations. 1-D simulations overestimate the shock yields by a factor of about ten, and predict shock-bang time several hundred ps later and ρR's two to three times higher than was observed experimentally. The convergence of the shock, and the nuclear production induced by the resulting expanding reshock have been demonstrated to be essentially one dimensional in nature, as even large low-mode and high-mode drive nonuniformities do not significantly perturb the shock timing or yield. This is encouraging for the potential of 1-D hydrodynamic codes to simulate converging shocks, but the poor performance of the current 1-D simulations indicates that the currently included physics is not sufficient to predict shock propagation and heating.

A 1-D model of shock convergence was constructed based on the Guderley self-similar converging shock problem. Simple extensions to the Guderley analysis were added in order to model shock timing and yields. This model was used to estimate the shock strength parameter and the thermal coupling between ions and electrons based on experimental data. It was found that stronger convergent shocks were launched in capsules with thinner shells, and that thermal coupling was weaker in capsules with low fill pressure. Comparison of this model to 1-D simulations demonstrated that the high shock strengths anticipated by the simulations are above the upper limit imposed by the model that is consistent with experimental yields. Further extensions to this model, including thermal conduction and a better treatment of the formation of the second shock, can be used to convert it to a predictive model. However, the fluid approximation used in both this model and the simulations may impose limitations to the calculation of shock convergence that can only be overcome using a kinetic treatment

Thorough understanding of the behavior of different materials in extreme conditions, the turbulent mixing of the fuel and shell due to RT instability growth, and the propagation and heating caused by shocks are essential to the success of inertial confinement fusion. The experimental observations reported herein provide robust and diverse constraints that can be used to improve the analytical and numerical tools which are used to predict ICF implosion performance.

Appendix A: Selected Acronyms

Acronym	Description
CD	a plastic used for target shells, having a ratio D:C of 1.53
CH	a plastic used for target shells, having a ratio H:C of 1.36
CPS	Charged-particle spectrometer
CR-39	Columbia Resin #39 (a plastic used for detection of ~MeV nuclear particles)
EOS	Equation of state (how pressure and energy depend on density and temperature)
FWHM	Full width at half maximum
ICF	Inertial confinement fusion
KH	Kelvin-Helmoltz (a hydrodynamic instability)
KO	Knock-on (a type of particle interaction, and a diagnostic port on OMEGA)
LILAC	not an acronym! (a 1-D rad-hydro code developed at LLE)
LLE	Laboratory for Laser Energetics (in Rochester, NY)
LLNL	Lawrence Livermore National Laboratory (in Livermore, CA)
MCF	Magnetic confinement fusion
NIF	National Ignition Facility (a laser facility under construction at LLNL)
NTD	Neutron temporal diagnostic
nTOF	Neutron time of flight (a neutron yield and ion temperature diagnostic)
OMEGA	not an acronym! (a laser facility located at LLE in Rochester, NY)
PTD	Proton temporal diagnostic
rms	root-mean-square
RM	Richtmyer-Meshkov (a hydrodynamic instability)
RT	Rayleigh-Taylor (a hydrodynamic instability)
SSD	Smoothing by spectral dispersion (a laser beam smoothing technique)
TCC	Target chamber center (where the OMEGA lasers are focused)
TIM	Ten-inch manipulator (a diagnostic instrument manipulator – 6 are on OMEGA)
UV	Ultraviolet
WRF	Wedge-range filter (a compact proton spectrometer)
YOC	The ratio of the experimental yield over the calculated yield

Appendix B: Notes on Error Analysis

This appendix gives a brief description of how the means and errors were calculated in this thesis. Many resources are available that explain error analysis in greater depth; see, for example, Bevington and Robinson [84].

On a given shot, the quantity A is measured to have a value A_i with an error σ_i. If A is measured in an ensemble of N nearly-identical shots, an estimate of the mean, $\bar{A}$, is given by:

$$\overline{A} = \left(\sum_i^N \frac{A_i}{\sigma_i^{\,2}} \right) \Bigg/ \left(\sum_i^N \frac{1}{\sigma_i^{\,2}} \right). \tag{B-1}$$

When all the errors σ_i are equal, this reduces to:

$$\overline{A} = \frac{1}{N} \sum_i^N A_i \ , \tag{B-2}$$

which is simply the arithmetic mean.

The standard error σ_A reflects the confidence in the estimate of the mean A in a shot ensemble by our observed value $\bar{A}$. When the σ_i's are equal, σ_A is equal to the standard deviation of the A_i's divided by the square root of N, which can be calculated as:

$$\sigma_A = \sqrt{\frac{\sum_i^N A_i^{\,2} - N\,\overline{A}^{\,2}}{N(N-1)}} \ . \tag{B-3}$$

When N is large, σ_A corresponds to the usual confidence intervals of a Gaussian or normal distribution (68% confidence that the actual value A falls in the interval $\bar{A} \pm \sigma_A$, 95% confidence it falls in the interval $\bar{A} \pm 2\sigma_A$, etc.). For small N, larger multiples of σ_A need to be used to attain an interval with the same confidence level.

Many shot ensembles in this work have a low value of N due to the high expense of shots on OMEGA. Although measurements of individual shots will generally be well distributed among the shot-to-shot variation of measurements for a particular type of shot, occasionally the measurements will cluster near each other when N is small, giving an estimate σ_A that does not reflect the real uncertainty. To compensate somewhat for this clustering effect, σ_A is calculated as the maximum of the value computed in Equation (B-3) and the value:

$$\sigma_A = \left(\sum_i^N \frac{1}{\sigma_i^{\,2}} \right)^{-1/2} \ . \tag{B-4}$$

which reduces to $\sigma_A = \sigma_0/\sqrt{N}$ when the σ_i are all equal to σ_0, the single-shot measurement error. This modification limits the reported error from becoming too small if the estimate of shot-to-shot variation is artificially low due to clustering. This modification will still underestimate the error, however, in the situation where the shot-to-shot variation is larger than both σ_0 and the estimated shot-to-shot variation.

When several measurements of the same quantity were made on the same shot, an additional step must be made to estimate the values of the A_i and σ_i for that shot. The same method was used as was described above. For example, if M measurements of A are made on a shot, each with a value A_{ij}, and error σ_0, the value of A_i is calculated as $A_i = (\Sigma_j A_{ij})/M$, which is analogous to Equation (B-2). The quantities $Y_{p\text{-}c}$, $Y_{p\text{-}s}$, ρR, and ρR_{sh} are all measured by several WRF spectrometers on a single shot, and values of σ_0 that were used in Appendix C are 10% for $Y_{p\text{-}c}$ and $Y_{p\text{-}s}$, 5 mg/cm^2 for ρR, and 1 mg/cm^2 for ρR_{sh}.

The values of some reported quantities are not directly observed, but are composite quantities that are calculated based on observations of other quantities (such as the normalized yield ratios $|\tilde{Y}_n|$, and $|\tilde{Y}_{p\text{-}c}|$). If the quantity $C = A + B$, the error in C is the quadrature sum of the errors on A and B:

$$\sigma_C = \sqrt{{\sigma_A}^2 + {\sigma_B}^2}\ . \tag{B-5}$$

For products and quotients, such as C = A×B, Equation (B-5) can still be used as long as the fractional error is used in place of the error for each quantity, $\sigma_A \rightarrow \sigma_A/A$, etc. If a quantity B is a function of quantity A, $B = f(A)$, (T_i inferred using the ratio method is such a quantity) the error in B is calculated as:

$$\sigma_B = \frac{f(A+\sigma_A) - f(A-\sigma_A)}{2}. \tag{B-6}$$

Whenever possible, composite and functional quantities are calculated individually for each shot, and the mean of that quantity for an ensemble is calculated as described above.

Appendix C: Selected Experimental Data

A selection of experimental data is presented in this appendix in tabular form. Descriptions of the columns are included below, as well as explanations for certain notation used in the tables.

The values in the $Y_{p\text{-}c}$ column for shots with pure D_2 fuel are actually the secondary D^3He yields, rather than the primary D^3He compression yields. In addition, only values of $Y_{p\text{-}s}$ measured by the WRF spectrometers are listed ($Y_{p\text{-}s}$ can also be measured by PTD).

Errors are put in the column immediately to the right of measured quantities, and when the error in the measurement of a quantity is the same for all shots in a group, a single value is put at the top of the that group. Errors are reported as a fractional (or percentage) error for yields, and as a value with the same units as the relevant quantity for all other quantities.

The double apostrophe (") indicates the value in that cell is the same as above, the dash (-) indicates that no value was obtained for that quantity on that shot, and the carrot (^) indicates that the value above was obtained by summation over more than one shot.

Column	**Description**
Shot	The OMEGA shot number
f_D	Atomic deuterium fraction in the fuel
Type	Target configuration, see Figure 4-1 (Type I unless stated otherwise)
Fuel	Pure D_2, pure ^3He, or a mixture of D^3He ($f_D = 0.5$ unless stated otherwise)
Pres.	Fill pressure of the fuel in the target
ΔR	Thickness of target shell
Diam.	Outer diameter of the target
E	Total laser energy delivered to the target
Y_n	DD-n yield
$Y_{p\text{-}c}$	D^3He compression yield (or secondary D^3He yield for D_2 fuels)
$Y_{p\text{-}s}$	D^3He shock yield
$Y_{DD\text{-}sh}$	DD-p shock yield
$\lvert\tilde{Y}_n\rvert$	Y_n scaled according to Equation (3-6) and normalized to value at $f_D = 0.5$
$\lvert\tilde{Y}_{p\text{-}c}\rvert$	$Y_{p\text{-}c}$ scaled according to Equation (3-6) and normalized to value at $f_D = 0.5$
T_{ntof}	Burn-averaged ion temperature as measured by the nTOF diagnostic
T_{rat}	Temperature calculated using the ratio method
ρR	Compression-burn-averaged areal density
ρR_{sh}	Shock-burn-averaged areal density
DD bang	Time of peak DD-n production
D^3He bang	Time of peak D^3He production (compression burn)
shock bang	Time of peak D^3He production (shock burn)
DD burn	FWHM duration of DD-n history
D^3He burn	FWHM duration of D^3He history (compression burn)
shock burn	FWHM duration of D^3He history (shock burn)
err	The estimated error of values to the left

Table C-1: Experimental data for 20 μm thick CH shells with different mixtures of D_2 and ^3He. Although only 9 shots of pure D_2 are shown here, data from 22 shots were analyzed.

Shot	f_D	Fuel	Pres. (atm)	ΔR (μm)	Diam. (μm)	E (kJ)	DD bang (ps)	err	DD burn (ps)	err	D^3He bang (ps)	err	D^3He burn (ps)	err
32130	1.00	D_2	15	19.1	878	24.2	1749	30	145	25	-	-	-	-
32184	"	"	"	19.0	880	23.8	1746		183					
32276	"	"	"	19.3	877	23.1	1737		164					
32851	"	"	"	19.4	878	22.8	1762		168					
34688	"	"	"	19.1	949	20.6	1923		173					
34689	"	"	"	20.2	941	22.1	1887		170					
35255	"	"	"	19.7	873	21.1	1770		144					
35256	"	"	"	20.1	864	22.7	1695		149					
37572	"	"	"	19.2	861	22.8	1712		160					
36583	0.778	D^3He	16.5	19.3	860	22.6	1668	30	151	25	-	30	-	30
36584	"	"	"	19.4	858	22.7	1667		166		1705		186	
36585	"	"	"	19.2	858	22.6	1703		162		1702		178	
36586	"	"	"	19.2	860	22.4	1692		161		1704		168	
36587	"	"	"	19.2	852	22.5	1675		149		1698		200	
35004	0.5	D^3He	18	19.6	877	22.7	1739	30	160	25	1717	30	173	30
35176	"	"	"	19.7	871	21.0	1830		152		1772		139	
37642	"	"	"	20.3	878	22.9	1787		162		1779		168	
37987	"	"	"	20.1	854	23.0	1766		169		1769		169	
37995	"	"	"	20.3	856	22.8	1816		155		1710		149	
38035	"	"	"	20.0	853	22.7	1725		168		1748		167	
38036	"	"	"	20.4	858	23.0	1729		138		1657		133	
38274	"	"	"	20.4	860	23.6	1635		151		-		144	
37988	0.273	D^3He	19	19.7	867	22.6	-	30	-	25	1758	30	167	30
37989	"	"	"	19.8	871	22.7	1741		122		1758		155	
37990	"	"	"	19.9	870	22.3	1817		116		1785		168	
37991	"	"	"	19.7	867	22.6	1704		177		1756		152	
37992	0.073	D^3He	19.75	19.7	872	22.5	-	-	-	-	1764	30	171	30
37993	"	"	"	19.5	871	22.6	-		-		1743		160	
37994	"	"	"	19.8	872	23.0	-		-		1723		164	
Num:	**f_D**			**AVERAGE:**										
22	1.000	D_2	15	19.5	879	22.9	1758	15	172	6	-		-	
5	0.778	D^3He	16.5	19.3	858	22.6	1681	13	158	11	1702	15	183	15
8	0.500	D^3He	18	20.1	863	22.7	1753	22	157	9	1736	17	155	11
4	0.273	D^3He	19	19.8	869	22.6	1754	33	138	19	1764	15	160	15
3	0.073	D^3He	19.75	19.7	872	22.7	-		-		1743	17	165	17

Table C-1 (cont.): Experimental data for 20 μm thick CH shells with different mixtures of D_2 and ^{3}He. Although only 9 shots of pure D_2 are shown here, data from 22 shots were analyzed.

Shot	f_D	Y_n ($\times 10^9$)	err (%)	$\lvert\tilde{Y}_n\rvert$	T_{ntof} (keV)	err	T_{rat} (keV)	err	Num WRF	$Y_{p\text{-}c}$ ($\times 10^8$)	err (%)	$\lvert\tilde{Y}_{p\text{-}c}\rvert$	ρR (mg/cm^2)	err
32130	1.00	236	10.0	2.92	4.1	0.5	-	-	4	5.47	3.0		60.0	2.4
32184	"	234		2.89	4.6				3	4.10	2.3		58.5	6.5
32276	"	156		1.93	4.4				3	2.47	1.8		65.0	7.0
32851	"	182		2.25	4.3				3	2.93	4.6		55.0	6.1
34688	"	198		2.45	4.0				3	3.62	8.7		58.2	8.4
34689	"	162		2.00	3.9				3	2.66	8.4		59.8	6.2
35255	"	178		2.20	-				2	2.65	12.7		52.4	7.1
35256	"	161		1.99	-				2	2.27	9.7		56.4	11.7
37572	"	147		1.82	3.8				-	-	-		-	-
36583	0.778	86.8	10.0	2.19	4.0	0.5	3.2	0.1	5	10.0	1.3	1.87	44.3	0.8
36584	"	83.0		2.09	4.0		3.2	0.1	5	9.6	7.4	1.80	46.9	1.8
36585	"	87.6		2.21	4.2		3.6	0.1	5	13.8	4.2	2.58	40.5	3.0
36586	"	78.3		1.98	3.7		3.7	0.2	5	13.4	9.4	2.51	47.2	2.0
36587	"	81.0		2.04	4.1		3.4	0.1	5	10.9	4.1	2.04	47.8	2.0
35004	0.5	15.5	10.0	1.20	4.3	0.5	3.7	0.2	2	9.73	5.2	1.59	49.4	1.4
35176	"	10.5		0.81	5.1		3.5	0.1	2	5.38	6.3	0.88	55.5	6.9
37642	"	10.5		0.81	4.9		3.2	0.1	4	4.40	4.6	0.72	48.3	2.7
37987	"	12.3		0.95	3.7		3.3	0.2	4	5.34	10.5	0.88	49.9	1.7
37995	"	13.0		1.00	4.9		3.2	0.1	2	5.25	1.1	0.86	50.3	0.2
38035	"	16.6		1.28	3.8		3.2	0.1	4	7.03	4.5	1.15	50.3	0.2
38036	"	13.5		1.04	3.9		3.6	0.2	4	7.70	12.8	1.26	44.8	5.9
38274	"	11.6		0.90	4.6		3.3	0.2	3	5.07	9.1	0.83	43.7	5.1
37988	0.273	4.46	10.0	1.38	4.9	0.5	2.8	0.1	5	3.19	2.0	0.78	53.5	1.9
37989	"	5.87		1.81	4.6		2.5	0.1	5	3.17	10.0	0.78	45.8	1.8
37990	"	5.94		1.84	4.6		2.6	0.1	6	3.38	4.1	0.83	49.2	2.0
37991	"	5.46		1.69	4.7		2.9	0.1	6	4.51	3.7	1.11	46.5	4.7
37992	0.073	0.42	10.0	2.08	4.8	0.5	2.6	0.1	6	1.11	3.6	0.92	52.7	1.3
37993	"	0.42		2.06	4.2		2.5	0.1	6	1.07	3.6	0.88	49.3	0.9
37994	"	0.36		1.78	4.7		2.9	0.1	6	1.37	3.2	1.14	55.1	3.3
Num:	f_D	**AVERAGE:**												
22	1.000	192	3.6	2.38	4.1	0.1	-		3	3.6	7.9	-	57.1	1.3
5	0.778	83.3	4.5	2.10	4.0	0.2	3.35	0.09	5	11.5	7.6	2.15	45.8	1.4
8	0.500	12.9	6.1	1.00	4.4	0.2	3.33	0.07	3	6.10	10.3	1.00	49.3	1.3
4	0.273	5.43	6.3	1.68	4.7	0.3	2.71	0.09	6	3.70	8.7	0.91	49.3	1.7
3	0.073	0.40	5.8	1.97	4.6	0.3	2.65	0.11	6	1.18	8.0	0.98	51.6	1.7

Table C-2: Experimental data for 24 μm thick CH shells with different mixtures of D_2 and ^3He.

Shot	f_D	Fuel	Pres. (atm)	ΔR (μm)	Diam. (μm)	E (kJ)	DD bang (ps)	err	DD burn (ps)	err	D^3He bang (ps)	err	D^3He burn (ps)	err
32182	1.00	D_2	15	24.1	873	24.2	1942	30	207	25	-	-	-	-
32185	"	"	"	24.0	866	24.0	1963		222					
32231	"	"	"	23.9	866	24.4	-		-					
32852	"	"	"	23.8	859	22.8	1991		196					
34690	"	"	"	24.5	873	22.4	1942		169					
34691	"	"	"	24.8	863	22.4	1895		179					
35262	"	"	"	23.4	883	23.0	1882		160					
35264	"	"	"	23.0	899	22.9	1924		167					
36357	"	"	"	23.4	887	22.9	1957		211					
36358	"	"	"	23.3	882	23.3	1929		188					
38527	0.778	D^3He	16.5	24.3	870	22.5	1858	30	152	25	1861	30	152	30
38528	"	"	"	24.3	869	22.6	1864		181		1858		161	
32821	0.5	D^3He	18	23.7	859	22.0	-	60	-	50	-	30	-	30
37643	"	"	"	23.9	861	23.0	1870		191		1875		179	
37645	"	"	"	23.8	881	22.6	1940		122		1941		182	
38032	"	"	"	24.1	857	23.0	1876		132		1896		159	
38033	"	"	"	23.7	880	22.6	1926		175		1940		158	
38034	"	"	"	23.6	870	22.7	1929		197		1935		187	
38278	"	"	"	24.0	860	23.1	1781		135		1817		146	
38279	"	"	"	24.2	864	22.8	1858		166		1858		177	
38525	"	"	"	24.0	855	22.1	1841		156		1832		144	
38529	0.073	D^3He	19.75	23.9	870	22.5	-	-	-	-	1808	30	126	30
38530	"	"	"	24.0	865	22.1	-		-		1823		138	
38531	"	"	"	23.7	871	22.2	-		-		1860		169	
Num:	f_D			**AVERAGE:**										
10	1.000	D_2	15	23.8	875	23.2	1936	11	189	8	-		-	
2	0.778	D^3He	16.5	24.3	870	22.6	1861	21	167	18	1860	21	156	21
9	0.500	D^3He	18	23.9	865	22.7	1878	21	159	18	1887	17	167	11
3	0.073	D^3He	19.75	23.9	869	22.3	-		-		1830	17	144	17

Table C-2 (cont.): Experimental data for 24 μm thick CH shells with different mixtures of D_2 and ^3He.

Shot	f_D	Y_n ($\times 10^9$)	err (%)	$\lvert\tilde{Y}_n\rvert$	T_{ntof} (keV)	err	T_{rat} (keV)	err	Num WRF	$Y_{p\text{-}c}$ ($\times 10^8$)	err (%)	$\lvert\tilde{Y}_{p\text{-}c}\rvert$	ρR (mg/cm^2)	err
32182	1.00	98	10.0	2.71	3.7	0.5			3	1.40	3.0		61.9	2.4
32185	"	92		2.54	3.9				3	1.62	2.3		66.5	6.5
32231	"	76		2.10	3.4				3	1.12	4.6		65.5	3.2
32852	"	68		1.87	3.5				3	0.89	1.8		60.5	7.0
34690	"	74		2.04	3.3				3	0.94	4.6		67.8	6.1
34691	"	60		1.66	3.9				2	0.66	0.7		52.9	7.8
35262	"	115		3.17	3.5				2	1.43	1.4		64.6	4.0
35264	"	123		3.40	3.9				2	1.64	1.6		63.2	2.2
36357	"	99		2.72	3.3				2	1.61	1.6		67.4	4.4
36358	"	95		2.61	3.4				2	1.39	1.4		75.8	1.6
38527	0.778	30	10.0	1.69	3.6	0.5	2.8	0.1	6	2.40	7.6	1.80	60.0	3.4
38528	"	31		1.76	3.1		3.1	0.1	6	3.26	9.5	2.44	54.2	3.4
32821	0.5	5.84	10.0	1.01	3.8	0.5	2.8	0.1	6	1.68	4.7	1.10	60.9	1.9
37643	"	4.55		0.79	4.5		3.1	0.1	4	1.74	4.6	1.14	49.2	1.7
37645	"	4.11		0.71	3.9		2.6	0.1	3	0.87	3.3	0.57	51.0	3.4
38032	"	6.05		1.04	4.3		2.7	0.1	3	1.40	12.7	0.91	54.5	1.5
38033	"	6.14		1.06	3.1		2.5	0.1	2	1.22	11.3	0.80	59.9	3.3
38034	"	7.59		1.31	3.1		2.7	0.1	5	1.82	3.6	1.19	55.3	4.0
38278	"	5.51		0.95	4.4		2.6	0.1	3	1.12	6.5	0.74	44.0	6.7
38279	"	6.19		1.07	4.2		2.7	0.1	2	1.53	6.5	1.00	44.0	-
38525	"	6.18		1.07	3.7		2.8	0.1	6	1.72	9.7	1.13	55.7	3.6
38529	0.073	0.21	10.0	2.26	-	0.5	2.5	0.1	3	0.51	9.2	1.69	65.6	3.3
38530	"	0.23		2.50	3.3		2.5	0.1	6	0.53	12.8	1.75	56.2	5.3
38531	"	0.22		2.37	-		2.3	0.1	6	0.39	12.2	1.28	61.3	3.1
Num:	f_D													
10	1.000	89.9	7.2	2.48	3.6	0.2	-		3	1.25	8.7	-	65.5	1.9
2	0.778	30.7	7.1	1.73	3.3	0.4	2.93	0.13	6	2.74	15.6	2.05	57.1	2.9
9	0.500	5.80	5.8	1.00	3.9	0.2	2.71	0.06	4	1.53	7.1	1.00	54.4	2.1
3	0.073	0.22	5.8	2.38	3.3	0.5	2.42	0.07	5	0.48	9.2	1.60	62.2	2.7

Table C-3: Experimental data for 20 and 24 μm thick CH shells with low pressure fills of pure D_2 and the standard D^3He mixture.

Shot	f_D	Fuel	Pres. (atm)	ΔR (μm)	Diam. (μm)	E (kJ)	DD bang (ps)	err	DD burn (ps)	err	D^3He bang (ps)	err	D^3He burn (ps)	err
32187	1.0	D_2	3	19.0	876.0	24.1	1704	30	-	25	-	-	-	-
32190	"	"	"	19.1	873.0	23.8	1724		132					
32426	"	"	"	19.0	875.0	22.5	1800		196					
35259	"	"	"	19.7	872.0	22.7	1705		133					
35260	"	"	"	19.7	871.0	23.4	1689		123					
35261	"	"	"	19.5	872.0	23.0	1727		141					
37581	"	"	"	19.4	861.0	22.6	1719		158					
35002	0.5	D^3He	3.6	20.0	880.0	23.3	1613	30	160	25	1650	30	133	30
35170	"	"	"	19.8	873.8	21.2	1785		172		1753		130	
36875	"	"	"	20.0	854.0	22.6	1695		121		-		-	
36876	"	"	"	20.0	856.0	22.8	1669		-		-		-	
37635	"	"	"	20.1	857.0	22.9	1661		-		1699		120	
38029	"	"	"	20.0	860.0	22.5	-		-		1709		113	
38030	"	"	"	20.1	857.0	22.7	1716		151		1692		121	
38031	"	"	"	19.4	860.0	22.3	1717		136		1695		123	
32188	1.0	D_2	3	24.1	860.0	24.0	-	30	-	25	-	-	-	-
32191	"	"	"	23.9	851.0	23.5	1915		161					
32427	"	"	"	24.1	855.0	22.5	1960		196					
35265	"	"	"	23.0	876.0	22.9	1810		146					
35266	"	"	"	22.9	885.0	23.2	1829		163					
35267	"	"	"	22.8	888.0	23.1	1845		138					
37664	0.5	D^3He	3.6	23.7	872.0	22.4	1732	60	-	-	1920	30	158	30
37665	"	"	"	23.6	874.0	22.3	1718		-		1889		88	
38553	"	"	"	23.6	873.0	22.1	-		-		1790		135	
38554	"	"	"	23.6	878.0	22.4	-		-		1806		156	
38555	"	"	"	23.7	877.0	22.7	-		-		1791		142	
38558	"	"	"	23.9	861.0	22.9	-		-		1739		134	
Num:	f_D			**AVERAGE:**										
7	1.0	D_2	3	19.3	871	23.2	1724	14	147	11				
8	0.5	D^3He	3.6	19.9	862	22.5	1694	20	148	11	1700	14	123	12
6	1.0	D_2	3	23.5	869	23.2	1872	28	161	11				
6	0.5	D^3He	3.6	23.7	873	22.5	1725	42	-		1822	28	135	12

Table C-3 (cont.): Experimental data for 20 and 24 μm thick CH shells with low pressure fills of pure D_2 and the standard D^3He mixture.

Shot	f_D	Y_n ($\times 10^9$)	err (%)	$\lvert\tilde{Y}_n\rvert$	T_{ntof} (keV)	err	T_{rat} (keV)	err	Num WRF	$Y_{p\text{-}c}$ ($\times 10^7$)	err (%)	ρR (mg/cm^2)	err
32187	1.0	40.1	10.0	2.19	-	0.5			3	7.71	9.0	77.7	6.5
32190	"	45.3		2.48	4.8				3	4.47	5.9	70.3	7.4
32426	"	47.4		2.59	4.6				3	6.56	7.8	71.3	4.9
35259	"	46.6		2.55	4.4				2	4.15	7.2		
35260	"	35.6		1.95	4.5				0				
35261	"	48.4		2.65	4.5				2	4.10	1.7		
37581	"	37.8		2.07	4.5				0				
35002	0.5	3.42	10.0	1.17	4.2	0.5	5.5	0.3	4	58.9	6.4	56.0	6.0
35170	"	2.95		1.01	4.8		4.3	0.3	2	27.2	12.3	62.9	2.0
36875	"	2.59		0.88	5.2		4.5	0.2	4	27.1	2.7	58.7	0.9
36876	"	2.22		0.76	5.7		4.9	0.2	5	29.5	3.2	54.3	3.5
37635	"	1.77		0.60	4.0		3.9	0.2	5	12.7	12.2	53.1	1.5
38029	"	3.08		1.05	3.5		3.7	0.2	5	18.8	6.6	54.5	1.8
38030	"	3.32		1.13	3.5		3.9	0.2	5	24.2	9.7	50.3	6.6
38031	"	4.07		1.39	3.6		3.4	0.2	5	20.6	13.5	56.5	1.6
32188	1.0	18	10.0	2.78	3.7	0.5			3	2.7	0.8	76.2	0.6
32191	"	15		2.33	-				3	1.4	7.1	61.1	1.9
32427	"	14		2.13	4.4				3	1.7	14.2	70.0	4.4
35265	"	26		3.97	4.0				2	2.2	21.6		
35266	"	23		3.60	3.8				2	1.6	21.4		
35267	"	27		4.14	3.9				2	2.0	11.9		
37664	0.5	1.01	10.0	0.98	4.0	0.5	3.2	0.1	6	4.0	4.5	56.7	1.9
37665	"	0.86		0.84	3.8		3.3	0.1	6	4.0	4.9	65.1	-
38553	"	1.22		1.18	3.9		3.3	0.2	6	5.4	11.3	56.1	4.1
38554	"	0.97		0.94	5.1		3.1	0.1	6	3.6	5.6	51.7	2.8
38555	"	0.85		0.83	3.9		3.3	0.1	5	3.7	7.9	45.2	3.5
38558	"	1.27		1.23	4.9		3.0	0.1	6	4.1	6.1	53.8	1.2
Num:	f_D	**AVERAGE:**											
7	1.0	43.0	4.5	2.35	4.6	0.2	-		1.9	5.10	14.4	72.9	3.5
8	0.5	2.93	8.8	1.00	4.3	0.3	4.17	0.24	4.4	30.4	16.1	55.9	1.3
6	1.0	20.4	11.2	3.16	4.0	0.2	-		2.5	2.13	9.1	68.9	4.4
6	0.5	1.03	7.0	1.00	4.3	0.5	3.17	0.06	5.8	3.97	6.6	56.4	2.7

Table C-4: Experimental data for 27 μm thick CH shells with high and low pressure fills of pure D_2 and the standard D^3He mixture.

Shot	f_D	Fuel	Pres. (atm)	ΔR (μm)	Diam. (μm)	E (kJ)	DD bang (ps)	err	DD burn (ps)	err	D^3He bang (ps)	err	D^3He burn (ps)	err
32189	1.0	D_2	3	26.8	856	23.7	-	30	-	25	-	-	-	-
32192	"	"	"	27.2	861	23.5	2011		157					
35285	"	"	"	27.9	851	23.0	1971		129					
35286	"	"	"	26.9	877	23.3	1968		164					
35287	"	"	"	27.0	856	23.3	1886		149					
37660	0.5	D^3He	3.6	27.0	874	21.5	1794	90	-	75	2020	30	158	30
37661	"	"	"	26.9	881	22.4	1879		-		2020		147	
38556	"	"	"	26.8	865	23.1	-		-		1842		158	
38557	"	"	"	27.4	870	23.0	-		-		1863		149	
32183	1.0	D_2	15	27.0	860	23.9	2091	30	233	25	-	-	-	-
32186	"	"	"	26.9	874	23.7	2092		208					
32232	"	"	"	27.1	862	24.6	-		-					
32424	"	"	"	27.0	863	23.3	-		-					
32853	"	"	"	27.0	871	22.8	2100		219					
35281	"	"	"	26.7	866	22.5	2026		175					
35282	"	"	"	26.9	859	23.3	1989		179					
35284	"	"	"	26.7	871	23.3	2013		194					
36359	"	"	"	27.3	867	23.4	2043		189					
36360	"	"	"	27.4	874	23.6	2089		208					
36361	"	"	"	26.3	858	22.8	2054		196					
38275	"	"	"	26.9	870	23.5	1974		179					
32833	0.5	D^3He	18	26.9	873	22.6	-	90	-	75	-	30	-	30
37646	"	"	"	26.6	875	22.9	2043		-		2061		204	
37648	"	"	"	27.6	861	22.9	2227		-		1990		163	
37750	"	"	"	27.1	878	23.7	-		-		1991		208	
37827	"	"	"	26.4	879	22.0	2078		167		2026		174	
38280	"	"	"	26.7	869	22.8	2020		-		1969		183	
Num:	f_D			**AVERAGE:**										
5	1.0	D_2	3	27.2	860	23.4	1959	26	150	13				
4	0.5	D^3He	3.6	27.0	873	22.5	1837	64	-		1936	48	153	15
12	1.0	D_2	15	26.9	866	23.4	2047	14	198	8				
6	0.5	D^3He	18	26.9	873	22.8	2092	47	167	75	2007	16	187	13

Table C-4 (cont.): Experimental data for 27 μm thick CH shells with high and low pressure fills of pure D_2 and the standard D^3He mixture.

Shot	f_D	Y_n ($\times 10^9$)	err (%)	$\lvert\tilde{Y}_n\rvert$	T_{ntof} (keV)	err	T_{rat} (keV)	err	Num WRF	$Y_{p\text{-}c}$ ($\times 10^7$)	err (%)	ρR (mg/cm^2)	err
32189	1.0	10.8	10.0	2.50	3.9	0.5	-	-	3	1.54	6.9	70.5	5.1
32192	"	9.5		2.20	3.6				3	0.77	3.9	63.7	6.4
35285	"	9.3		2.15	3.3				2	0.50	10.0		
35286	"	13.4		3.11	3.4				2	0.85	8.2		
35287	"	10.1		2.34	4.3				0				
37660	0.5	0.49	10.0	0.71	2.5	0.5	2.5	0.1	6	0.96	14.1	53.5	3.0
37661	"	0.61		0.89	2.2		2.6	0.2	6	1.29	16.4	54.3	2.9
38556	"	0.79		1.15	5.3		2.9	0.1	6	2.50	7.7	-	-
38557	"	0.86		1.25	3.9		3.2	0.2	6	3.56	14.3	47.5	2.0
32183	1.0	58	10.0	3.02	3.5	0.5	-	-	3	8.8	9.6	66.5	2.7
32186	"	57		2.97	3.5				3	8.1	1.4	65.3	6.5
32232	"	46		2.42	3.4				3	7.7	17.4	67.5	0.7
32424	"	41		2.16	2.9				3	6.4	2.2	73.3	1.8
32853	"	40		2.11	2.9				3	5.6	10.9		
35281	"	32		1.69	3.0				2	2.4	11.4		
35282	"	47		2.44	3.2				2	3.5	7.0		
35284	"	59		3.11	3.4				2	4.7	12.2		
36359	"	49		2.54	3.2				2	8.7	1.4		
36360	"	41		2.16	3.0				2	6.4	7.0		
36361	"	42		2.18	3.0				2	5.7	4.4		
38275	"	52		2.71	3.2				2	2.9	1.0	50.4	7.0
32833	0.5	2.9	10.0	0.93	3.3	0.5	2.6	0.1	6	6.2	7.6	61.7	4.2
37646	"	2.4		0.77	2.6		2.3	0.1	4	3.2	4.8	52.9	4.5
37648	"	2.2		0.73	3.2		2.5	0.1	4	4.4	2.7	44.4	4.9
37750	"	2.9		0.95	3.3		2.7	0.1	5	6.9	2.3	49.0	2.3
37827	"	4.1		1.33	3.4		2.7	0.1	5	10.4	7.3	59.3	5.1
38280	"	3.9		1.29	3.7		1.9	0.1	3	2.9	4.4	52.6	5.1
Num:	f_D	**AVERAGE:**											
5	1.0	10.6	7.0	2.46	3.7	0.2	-		2.0	0.96	22.9	67.9	4.0
4	0.5	0.69	12.2	1.00	3.5	0.7	2.78	0.16	6.0	2.27	26.3	50.6	2.1
12	1.0	46.9	5.1	2.46	3.2	0.1	-		2.4	6.09	10.5	68.0	3.8
6	0.5	3.05	10.4	1.00	3.3	0.5	2.32	0.13	4.5	5.30	21.7	52.0	2.6

Table C-5: Experimental data for Type I, II, and III capsules with 20 μm thick shells and with high and low fill pressures.

Shot	Type	Fuel	Pres. (atm)	ΔR (μm)	Diam. (μm)	E (kJ)	DD bang (ps)	err	DD burn (ps)	err	D^3He bang (ps)	err	D^3He burn (ps)	err
35004	I	D^3He	18	19.6	877	22.7	1739	30	160	25	1717	30	173	30
35176	"	"	"	19.7	871	21.0	1830		152		1772		139	
37642	"	"	"	20.3	878	22.9	1787		162		1779		168	
37987	"	"	"	20.1	854	23.0	1766		169		1769		169	
37995	"	"	"	20.3	856	22.8	1816		155		1710		149	
38035	"	"	"	20.0	853	22.7	1725		168		1748		167	
38036	"	"	"	20.4	858	23.0	1729		138		1657		133	
38274	"	"	"	20.4	860	23.6	1635		151		-		144	
35002	I	D^3He	3.6	20.0	880	23.3	1613	30	160	25	1650	30	133	30
35170	"	"	"	19.8	874	21.2	1785		172		1753		130	
36875	"	"	"	20.0	854	22.6	1695		121		-		-	
36876	"	"	"	20.0	856	22.8	1669		-		-		-	
37635	"	"	"	20.1	857	22.9	1661		-		1699		120	
38029	"	"	"	20.0	860	22.5	-		-		1709		113	
38030	"	"	"	20.1	857	22.7	1716		151		1692		121	
38031	"	"	"	19.4	860	22.3	1717		136		1695		123	
32828	II	^3He	20	20.5	877	22.4	-	-	-	-	1880	30	169	30
32832	"	"	"	20.2	864	22.7	-		-		1890		144	
35003	"	"	"	20.5	881	23.2	-		-		1786		164	
35288	"	"	"	20.4	873	23.2	-		-		-		-	
35289	"	"	"	20.5	877	23.1	-		-		-		-	
35290	"	"	"	20.5	877	23.2	-		-		-		-	
37639	"	"	"	20.1	859	22.8	-		-		1764		138	
32826	II	^3He	4	20.5	873	22.4	-	-	-	-	1817	30	160	30
32827	"	"	"	20.8	876	22.5	-		-		1842		143	
35000	"	"	"	20.4	876	20.5	-		-		1792		127	
37636	"	"	"	19.9	866	22.9	-		-		1733		162	
37637	"	"	"	20.0	854	22.8	-		-		1740		175	
37641	III	^3He	4	20.9	855	22.9	-		-		-		-	
Num:	**Type:**			**AVERAGE:**										
8	I	D^3He	18	20.1	863	22.7	1753	22	157	9	1736	17	155	11
8	I	D^3He	3.6	19.9	862	22.5	1694	20	148	11	1700	14	123	12
7	II	^3He	20	20.4	873	22.9					1830	32	154	15
5	II	^3He	4	20.3	869	22.2					1785	21	153	13

Table C-5 (cont.): Experimental data for Type I, II, and III capsules with 20 μm thick shells and with high and low fill pressures.

Shot	Type	Fuel	Pres. (atm)	Y_n ($\times 10^8$)	err (%)	T_{ntof} (keV)	err	Num WRFs	$Y_{p\text{-}c}$ ($\times 10^7$)	err (%)	ρR (mg/cm^2)	err
35004	I	D^3He	18	155	10.0	4.3	0.5	2	97.3	5.2	49.4	1.4
35176	"	"	"	105		5.1		2	53.8	6.3	55.5	6.9
37642	"	"	"	105		4.9		4	44.0	4.6	48.3	2.7
37987	"	"	"	123		3.7		4	53.4	10.5	49.9	1.7
37995	"	"	"	130		4.9		2	52.5	1.1	50.3	0.2
38035	"	"	"	166		3.8		4	70.3	4.5	50.3	0.2
38036	"	"	"	135		3.9		4	77.0	12.8	44.8	5.9
38274	"	"	"	116		4.6		3	50.7	9.1	43.7	5.1
35002	I	D^3He	4	34.2	10.0	4.2	0.5	4	58.9	6.4	56.0	6.0
35170	"	"	"	29.5		4.8		2	27.2	12.3	62.9	2.0
36875	"	"	"	25.9		5.2		4	27.1	2.7	58.7	0.9
36876	"	"	"	22.2		5.7		5	29.5	3.2	54.3	3.5
37635	"	"	"	17.7		4.0		5	12.7	12.2	53.1	1.5
38029	"	"	"	30.8		3.5		5	18.8	6.6	54.5	1.8
38030	"	"	"	33.2		3.5		5	24.2	9.7	50.3	6.6
38031	"	"	"	40.7		3.6		5	20.6	13.5	56.5	1.6
32828	II	^3He	20	4.5	10.0	2.2	0.5	6	1.81	5.2	58.1	4.3
32832	"	"	"	5.6		2.6		6	2.05	4.7	69.4	2.3
35003	"	"	"	5.6		2.0		3	1.80	12.1	59.0	4.7
35288	"	"	"	4.2		1.8		2	0.75	12.6	49.9	6.3
35289	"	"	"	6.4		2.3		2	1.07	16.4	55.7	6.2
35290	"	"	"	6.5		2.5		2	1.07	2.5	51.0	5.2
37639	"	"	"	3.1		1.7		4	1.43	10.7	43.3	3.1
32826	II	^3He	4	9.0	10.0	2.1	0.5	6	2.96	3.8	63.9	3.8
32827	"	"	"	10.5		2.0		6	3.49	4.0	68.5	2.7
35000	"	"	"	7.2		2.7		5	1.26	8.1	56.6	2.0
37636	"	"	"	9.4		2.6		5	2.35	15.0	51.8	6.2
37637	"	"	"	10.8		3.2		5	2.16	15.2	53.2	4.6
37641	III	^3He	4	1.3	10.0	-		5	0.28	10.1	52.9	5.8
Num:	**Type:**			**AVERAGE:**								
8	I	D^3He	18	129.4	6.1	4.4	0.2	3.1	61.0	10.3	49.3	1.3
8	I	D^3He	3.6	29.3	8.8	4.3	0.3	4.4	30.4	16.1	55.9	1.3
7	II	^3He	20	5.1	9.2	2.2	0.2	3.6	1.68	10.8	58.3	3.1
5	II	^3He	4	9.4	6.9	2.5	0.2	5.4	2.96	12.8	60.5	3.2

Table C-6: Experimental shock burn data for capsules of various thickness filled with 3.6 atm of D^3He.

Shot	Fuel	Pres. (atm)	ΔR (μm)	Diam. (μm)	E (kJ)	shock bang (ps)	err	shock burn (ps)	err	Num WRFs	Y_{p-s} ($\times 10^7$)	err (%)	ρR_{sh} (mg/cm^2)	err
39519	D^3He	3.6	14.5	879	23.2	1251	50	109	45	-	-	-	-	-
39520	"	"	14.5	874	23.5	1223		92						
39521	"	"	14.7	872	23.3	1224		123						
35002	D^3He	3.6	20.0	880	23.3	1428	40	122	35	-	-	-	-	-
35170	"	"	19.8	874	21.2	1506		116						
36875	"	"	20.0	854	22.6	-		-						
36876	"	"	20.0	856	22.8	-		-						
37635	"	"	20.1	857	22.9	1461		143						
38029	"	"	20.0	860	22.5	1513		136						
38030	"	"	20.1	857	22.7	1459		75						
38031	"	"	19.4	860	22.3	1451		-						
37664	D^3He	3.6	23.7	872	22.4	1690	30	167	25	4	0.40	6.4	11.5	0.7
37665	"	"	23.6	874	22.3	1635		139		1	0.30	-	9.5	-
38553	"	"	23.6	873	22.1	1563		99		6	0.57	10.0	10.3	0.8
38554	"	"	23.6	878	22.4	1562		138		6	0.49	6.3	8.9	0.5
38555	"	"	23.7	877	22.7	1555		120		5	0.51	10.7	9.5	0.7
38558	"	"	23.9	861	22.9	1503		111		6	0.57	6.6	9.6	1.3
37660	D^3He	3.6	27.0	874	21.5	1775	25	103	15	4	0.14	19.1	10.2	0.8
37661	"	"	26.9	881	22.4	1764		181		5	0.18	19.5	11.1	1.1
38556	"	"	26.8	865	23.1	-		-		0	-	-	-	-
38557	"	"	27.4	870	23.0	1653		83		3	0.30	9.9	13.2	0.5
Num:			**AVERAGE:**											
3	D^3He	3.6	14.6	875	23.3	1233	29	108	26					
8	D^3He	3.6	19.9	862	22.5	1470	16	118	16					
6	D^3He	3.6	23.7	873	22.5	1585	27	129	10	4.7	0.48	8.8	9.8	0.4
4	D^3He	3.6	27.0	873	22.5	1731	39	122	30	3.0	0.25	20.0	12.0	0.9

Table C-7: Experimental shock burn data for capsules of various thickness filled with 18 atm of D^3He.

Shot	Fuel	Pres. (atm)	ΔR (μm)	Diam. (μm)	E (kJ)	shock bang (ps)	err	shock burn (ps)	err	Num WRFs	Y_{p-s} ($\times 10^7$)	err (%)	ρR_{sh} (mg/cm^2)	err
39522	D^3He	18	14.5	872	23.3	1244	50	137	45	-	-	-	-	-
39523	"	"	14.6	875	22.9	1266		132						
39524	"	"	14.7	878	23.1	1281		141						
35004	D^3He	18	19.6	877	22.7	1506	40	146	35	0	-	-	-	-
35176	"	"	19.7	871	21.0	1522		144		0				
37642	"	"	20.3	878	22.9	1497		118		3	3.38	15.0	9.1	0.6
37987	"	"	20.1	854	23.0	1509		161		2	3.17	9.5	7.2	2.4
37995	"	"	20.3	856	22.8	1482		169		3	2.61	14.9	5.8	1.1
38035	"	"	20.0	853	22.7	1497		133		0				
38036	"	"	20.4	858	23.0	1440		141		0				
38274	"	"	20.4	860	23.6	1598		159		0				
32821	D^3He	18	23.7	859	22.0	-	30	-	25	6	1.61	5.4	10.9	0.7
37643	"	"	23.9	861	23.0	1623		159		4	1.48	5.6	9.0	0.3
37645	"	"	23.8	881	22.6	1617		114		3	1.12	6.1	9.2	0.2
38032	"	"	24.1	857	23.0	1586		113		2	1.43	7.0	8.3	1.0
38033	"	"	23.7	880	22.6	1632		152		2	1.39	6.5	9.0	0.2
38034	"	"	23.6	870	22.7	1608		136		5	1.95	7.7	8.4	0.8
38278	"	"	24.0	860	23.1	1557		139		3	0.95	10.1	4.1	1.9
38279	"	"	24.2	864	22.8	1572		121		1	0.96	-	6.2	-
38525	"	"	24.0	855	22.1	1534		158		6	2.10	11.1	10.0	1.2
32833	D^3He	18	26.9	873	22.6	-	25	-	15	6	1.59	8.5	13.9	1.2
37646	"	"	26.6	875	22.9	1711		172		4	1.03	3.8	9.4	0.7
37648	"	"	27.6	861	22.9	1697		131		4	1.28	2.2	10.2	1.0
37750	"	"	27.1	878	23.7	1680		125		5	2.37	3.8	10.6	1.7
37827	"	"	26.4	879	22.0	1708		153		4	1.14	7.0	11.6	0.6
38280	"	"	26.7	869	22.8	1655		151		3	0.50	7.0	5.0	0.7
Num:			**AVERAGE:**											
3	D^3He	18	14.6	875	23.1	1264	29	137	26					
8	D^3He	18	20.1	863	22.7	1506	16	146	12	1.0	3.09	7.4	8.2	1.0
9	D^3He	18	23.9	865	22.7	1591	12	137	9	3.6	1.45	9.3	8.9	0.7
6	D^3He	18	26.9	873	22.8	1690	11	146	8	4.3	1.44	17.8	9.4	1.2

Table C-8: Experimental DD-p shock burn data for capsules of various thickness filled with 18 atm of D^3He. The carrot (^) indicates that data is the results of a sum over two shots (the DD-p shock yield is the per-shot average over the summation).

Shot	Fuel	Pres. (atm)	ΔR (μm)	Diam. (μm)	E (kJ)	Num Shots	$Y_{DD\text{-}sh}$ ($\times 10^7$)	err (%)	ρR_{sh} (mg/cm^2)	err	T_{rat} (keV)	err (+)	err (-)
37642	D^3He	18	20.3	878	22.9	1	16.6	20.0	9.7	1.0	5.8	0.7	0.5
37987	"	"	20.1	854	23.0	1	15.2	20.0	8.9	1.0	5.8	0.6	0.4
37995	"	"	20.3	856	22.8	1	10.5	20.0	9.2	1.0	6.3	0.8	0.5
37643	D^3He	18	23.9	861	23.0	2	7.8	14.1	10.1	1.0	5.3	0.5	0.4
37645	"	"	23.8	881	22.6	^	^		^		^	^	^
38525	"	"	24.0	855	22.1	1	12.2	20.0	9.8	1.0	5.4	0.6	0.4
37646	D^3He	18	26.6	875	22.9	2	4.0	14.1	11.1	1.0	6.7	0.3	1.0
37648	"	"	27.6	861	22.9	^	^		^		^	^	^
Num:			**AVERAGE:**			**AVERAGE:**							
3	D^3He	18	20.2	863	22.9		14.1	13.1	9.3	0.6	5.9	0.4	0.3
3	D^3He	18	23.9	866	22.6		9.2	19.6	10.0	0.7	5.4	0.4	0.3
2	D^3He	18	27.1	868	22.9		4.0	14.1	11.1	1.0	6.7	0.3	1.0

References

[1] A. Einstein, Ann. Phys. 18, 639 (1905).
[2] Energy Information Administration, *International Energy Outlook 2005*, DOE/EIA-0484(2005) (Washington, DC, 2005).
[3] Intergovernmental Panel on Climate Change, *Climate Change 2001: Synthesis Report* (Cambridge, UK, 2002).
[4] F. W. Aston, Nature 105, 617 (1920).
[5] A. S. Eddington, Nature 106, 14 (1920).
[6] R. Atkinson and F. Houtermans, Z. fur Physik 54, 656 (1929).
[7] J. D. Cockroft and E. T. S. Walton, Proc. Roy. Soc. A137, 229 (1932).
[8] H. A. Bethe, Phys. Rev. 55, 434 (1939).
[9] R. Rhodes, *The Making of the Atomic Bomb*, (Simon & Schuster, 1986).
[10] ITER EDA Doc. Series No. 22, International Atomic Energy Agency (Vienna, 2001).
[11] A. L. Schawlow and C. H. Townes, Phys. Rev. 112, No 6, 1940 (1958).
[12] T. H. Maiman, Nature 187, 493 (1960).
[13] R. E. Kidder, in *High-Power Laser Ablation*, SPIE Proceedings Vol. 3343, p. 10 (1998).
[14] G. H. Miller, E. I. Moses, and C. R. Wuest, Nucl. Fusion 44, S228 (2004).
[15] J. Nuckolls, L. Wood, A. Thiessen *et al*, Nature (London) 239, 139 (1972).
[16] K. A. Brueckner and S. Jorna, Rev. Mod. Phys. 46, No 2, 325 (1974).
[17] J. D. Lindl, Phys. Plasmas 2, 3933 (1995).
[18] J. D. Lindl, *Inertial Confinement Fusion*, Springer, (1998).
[19] S. Atzeni and J. Meyer-Ter-Vehn, *The Physics of Inertial Fusion*, Oxford University Press, (2004).
[20] W. Kruer, *The Physics of Laser Plasma Interactions*, Westview Press, (1988).
[21] Ya. B. Zel'dovich and Yu. P. Raizer, *Physics of Shock Waves and High-Temperature Hydrodynamic Phenomena*, edited by W. D. Hayes and R. F. Probstein, Dover Publications, (2002).
[22] R. P. Drake, *High-Energy-Density Physics*, Springer (2006).
[23] H.-S. Bosch and G. M. Hale, Nucl. Fusion 32, No 5, 611 (1992).
[24] J. D. Lawson, Proc. Phys. Soc. B70, 6 (1957).
[25] M. D. Rosen, Phys. Plasmas 6, 1690 (1999).
[26] M. Tabak, J. Hammer, M. E. Glinsky *et al*, Phys. Plasmas 1, 1626 (1994).
[27] S. E. Bodner, D. G. Colombant, J. H. Gardner *et al*, Phys. Plasmas 5, 1901 (1998).
[28] R. L. McCrory, R. E. Bahr, R. Betti *et al*, Nucl. Fusion 41, 1413 (2001).
[29] J. M. Soures, R. L. McCrory, C. P. Verdon *et al*, Phys. Plasmas 3, 2108 (1996).
[30] T. R. Boehly, D. L. Brown, R. S. Craxton *et al*, Opt. Commun. 133, 495 (1997).
[31] J. Delettrez, R. Epstein, M. C. Richardson *et al*, Phys. Rev. A 36, 3926 (1987).
[32] Lord Rayleigh, Proc. London Math. Soc. 14, 170 (1883).
[33] G. Taylor, Proc. Roy. Soc. London A 201, 192 (1950).
[34] R. Betti, V. N. Goncharov, R. L. McCrory *et al*, Phys. Plasmas 5, 1446 (1998).
[35] G. Dimonte, Phys. Plasmas 6, 2009 (1999).
[36] F. J. Marshall, J. A. Delettrez, R. Epstein *et al*, Phys. Plasmas 11, 251 (2004).
[37] S. Skupsky and S. Craxton, Phys. Plasmas 6, 2157 (1999).
[38] S. Kurebayashi, J. A. Frenje, F. H. Séguin *et al*, Phys. Plasmas 12, 032703 (2005).
[39] H. Brysk, Plasma Phys. 15, 611 (1973).

[40] L. Ballabio, J. Källne, and G. Gorini, Nucl. Fusion 38, No 11, 1723 (1998).
[41] C. K. Li and R. D. Petrasso, Phys. Rev. Lett. 70, 3059 (1993).
[42] F. H. Séguin, J. A. Frenje, C. K. Li *et al*, Rev. Sci. Instrum. 74, 975 (2003).
[43] J. A. Frenje, K. M. Green, D. G. Hicks *et al*, Rev. Sci. Instrum. 72, 854 (2001).
[44] D. G. Hicks, C. K. Li, F. H. Séguin *et al*, Phys. Plasmas 7, 5106 (2000).
[45] T. J. Murphy, C. W. Barnes, R. R. Berggren *et al*, Rev. Sci. Instrum. 72, 773 (2001).
[46] R. A. Lerche and T. J. Murphy, Rev. Sci. Instrum. 63, 4880 (1992).
[47] M. J. Moran, V. Yu Glebov, C. Stoeckl *et al*, Rev. Sci. Instrum. 76, 023506 (2005).
[48] J. A. Frenje, C. K. Li, F. H. Séguin *et al*, Rev. Sci. Instrum. 73, 2597 (2002).
[49] C. K. Li, F. H. Séguin, J. A. Frenje *et al*, Rev. Sci. Instrum., to be published (2006).
[50] D. G. Hicks, Ph.D. thesis, MIT (1999).
[51] D. G. Hicks, C. K. Li, F. H. Séguin *et al*, Phys. Plasmas 8, 626 (2001).
[52] R. A. Lerche, D. W. Phillion, and G. L. Tietbohl, Rev. Sci. Instrum. 66, 933 (1995).
[53] C. Stoeckl, V. Yu. Glebov, S. Roberts *et al*, Rev. Sci. Instrum. 74, 1713 (2003).
[54] J. A. Frenje, C. K. Li, F. H. Séguin *et al*, Phys. Plasmas 11, 2798 (2004).
[55] J. L. DeCiantis, F. H. Séguin, J. A. Frenje *et al*, Rev. Sci. Instrum. 76, 043503 (2006).
[56] F. H. Séguin, J. L. DeCiantis, J. A. Frenje *et al*, Rev. Sci. Instrum. 75, 3520 (2004).
[57] F. H. Séguin, J. L. DeCiantis, J. A. Frenje *et al*, Phys. Plasmas, to be published (2006).
[58] S. P. Regan, J. A. Delettrez, V. Yu. Glebov *et al*, Bull. Am. Phys. Soc. 47, 113 (2005).
[59] J. R. Rygg, J. A. Frenje, C. K. Li *et al*, Phys. Plasmas 13, 052702 (2006).
[60] M. Bonino, private communication, Lab for Laser Energetics, Rochester, NY (2006).
[61] C. K. Li, D. G. Hicks, F. H. Séguin *et al*, Phys. Plasmas 7, 2578 (2000).
[62] R. D. Petrasso, J. A. Frenje, C. K. Li *et al*, Phys. Rev. Lett. 90, 095002 (2003).
[63] S. P. Regan, J. A. Delettrez, V. N. Goncharov *et al*, Phys. Rev. Lett. 92, 185002 (2004).
[64] L. Spitzer and R. Harm, Phys. Rev. 89, 977 (1953).
[65] S. I. Braginskii, Rev. of Plasma Phys. 1, 205 (1965).
[66] D. Henderson, Phys. Rev. Lett. 33, No 19, 1142 (1974).
[67] P. E. Dimotakis, Annu. Rev. Fluid Mech. 37, 329 (2005).
[68] A. J. Scannapieco and B. Cheng, Phys. Lett. A 299, 49 (2002).
[69] C. K. Li, F. H. Séguin, J. A. Frenje *et al*, Phys. Rev. Lett. 89, 16502 (2002).
[70] P. B. Radha, J. Delettrez, R. Epstein *et al*, Phys. Plasmas 9, 2208 (2002).
[71] S. P. Regan, J. A. Delettrez, F. J. Marshall *et al*, Phys. Rev. Lett. 89, 085003 (2002).
[72] D. C. Wilson, C. W. Cranfill, C. Christensen *et al*, Phys. Plasmas 11, 2723 (2004).
[73] D. C. Wilson, T. C. Sangster, P. S. Ebey *et al*, Bull. Am. Phys. Soc. 47, 312 (2005).
[74] T. R. Boehly, E. Vianello, J. E. Miller *et al*, Phys. Plasmas 13, 056303 (2006).
[75] V. N. Goncharov, O. V. Gotchev, E. Vianello *et al*, Phys. Plasmas 13, 012702 (2006).
[76] T. R. Dittrich, S. W. Hann, M. M. Marinak *et al*, Phys. Plasmas 5, 3708 (1998).
[77] V. G. Guderley, Luftfahrtforsch. 19, 302 (1942).
[78] R. B. Lazarus, SIAM J. Numer. Anal. 18, 316 (1981).
[79] P. Hafner, SIAM J. Appl. Math. 48, 1244 (1988).
[80] E. B. Goldman, Plasma Phys. 15, 289 (1973).
[81] H. J. Haubold and W. John, Plasma Phys. 23, 399 (1981).
[82] P. Reinicke and J. Meyer-ter-Vehn, Phys. Fluids A 3, 1807 (1991).
[83] G. Sorasio, M. Marti, R. Fonseca, and L. O. Silva, Phys. Rev. Lett. 96, 045005 (2006).
[84] P. Bevington and D. K. Robinson, *Data Reduction and Error Analysis for the Physical Sciences*, McGraw-Hill (2002).